Design of a small Aqueous Homogeneous Reactor for production of ^{99}Mo

Improving the reliability of the supply chain

S. Rijnsdorp

Master Thesis

TU Delft Delft University of Technology

Challenge the future

DESIGN OF A SMALL AQUEOUS HOMOGENEOUS REACTOR FOR PRODUCTION OF ^{99}MO

IMPROVING THE RELIABILITY OF THE SUPPLY CHAIN

by

S. Rijnsdorp BSc

in partial fulfillment of the requirements for the degree of

Master of Science
in Applied Physics

at Delft University of Technology,
to be defended on Tuesday September 2, 2014 at 09:30.

faculty	Applied Sciences	
department	Radiation Science and Technology	
section	Nuclear Energy and Radiation Applications	
supervisors	Dr.ir. J.L. Kloosterman	
	Dr.ir. M. Rohde	
thesis committee	Dr.ir. J.L. Kloosterman	TU Delft, Applied Sciences, RST, NERA
	Dr.ir. M. Rohde	TU Delft, Applied Sciences, RST, NERA
	Dr. Eng. L.M. Portela	TU Delft, Applied Sciences, ChemE, TP

TU Delft Delft University of Technology

ABSTRACT

Medical isotopes are used worldwide for medical imaging and treatment of patients with different kinds of diseases, for example thyroid diseases and blood disorders. The most widely used radioisotope for medical imaging is ^{99m}Tc, a daughter nuclide of ^{99}Mo. Annually, around 400,000 diagnostical treatments using ^{99m}Tc are carried out in the Netherlands.

The characteristic aspect that makes ^{99m}Tc so useful for medical imaging is also the challenge: ^{99m}Tc has a half-life of approximately 6 hours. Because also the parent nuclide ^{99}Mo has a relatively short half-life (66 hours), a continuous production and supply is needed. Recently, a number of events occurred, disrupting the supply, which led to the wish for a more reliable production method of radioisotopes. Currently, the entire world demand is produced in 5 reactors, meaning that an unplanned outage of one or more reactors will immediately decrease the supply of ^{99}Mo. If more reactors are used for production of ^{99}Mo on a smaller scale, the effect of such an event is decreased.

An aqueous homogeneous reactor (AHR) is considered a suitable candidate to produce medical isotopes on a small scale. Various aspects contribute to the suitability, such as the relatively easy extraction of ^{99}Mo, the possibility to use low enriched uranium (LEU) fuel and the large negative void and temperature feedback.

In this thesis, an AHR design is optimized to meet the Dutch demand for ^{99}Mo for the coming years. In the process, an existing computational model is used and improved to better describe physical phenomena that come into play when operating the reactor, such as temperature-induced fuel expansion and creation of void bubbles. An earlier proposed geometry is used and slightly altered.

The designed reactor is fueled by a uranyl sulfate solution containing 225 gL^{-1} uranium with an inflow rate of 0.4 kg s^{-1} and operates at a power of 13.2 kW in steady state. At this power level, the maximum fuel temperature in the core is 316.1 K, which is well below the boiling point. When operating continuously, the reactor is capable of producing an amount of ^{99}Mo that is sufficient to meet the estimated Dutch demand, assuming daily transport from the reactor facility.

An important result of the investigation of transient behavior in case of an unanticipated event, is that safe operation is ensured for all scenarios considered. The largest problems could occur if for some reason the fuel level in the reactor rises significantly, but this can be easily prevented by adding supplementary outflow pipes just above the desired fuel level. In all other scenarios, the power excursions induced by an increase in reactivity are limited by the negative feedback effects. The maximum fuel temperature stays well below the boiling point in all cases considered.

CONTENTS

1

INTRODUCTION

1.1. NUCLEAR FISSION

The fission of nuclides is in itself a natural process and occurs usually in an unstable nucleus of an atom with a high mass number. In fission reactors the process of fission is induced by the absorbtion of neutrons by the fissile nuclides which split into new nuclides while releasing neutrons which can be used for another fission event. A typical decay diagram of a neutron induced fission of fissile uranium, ^{235}U, is shown in figure 1.1.

Two different types of product can be distinguished: fission products and neutrons. Both of these carry kinetic energy, which can be converted into electric energy.

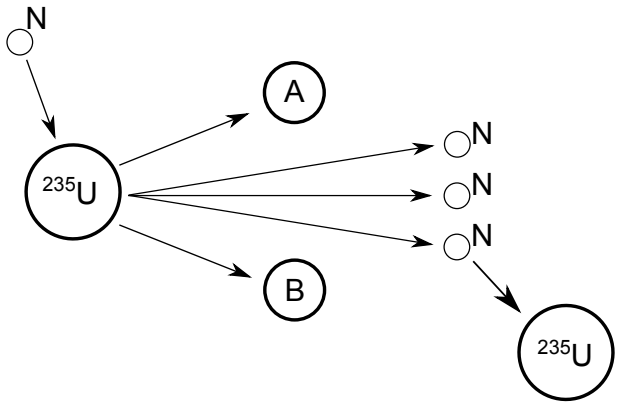

Figure 1.1: The fission process schematically visualised. After the neutron interacts with ^{235}U, the formed U_{235} atom splits into two smaller isotopes *A* and *B*. Meanwhile some neutrons (*N*, on average approximately 2.45 per fission [1]) are released. These neutrons can be used for various purposes, for example for another fission. If the number of neutrons emerging from a fission that initiate a new fission is equal to or larger than 1, a chain reaction can be sustained.

Neutrons

The released neutrons are of importance for any reactor, as at least one released neutron should initiate a new fission to sustain the process. However, approximately 2.45 neutrons are released per fission of ^{235}U, leaving a possibility to extract the surplus of neutrons and use them for the study of structures by neutron scattering (as is done with neutrons produced in the Hoger Onderwijs Reactor in Delft), the bombardment of isotopes, and other purposes. An application of irradiating isotopes

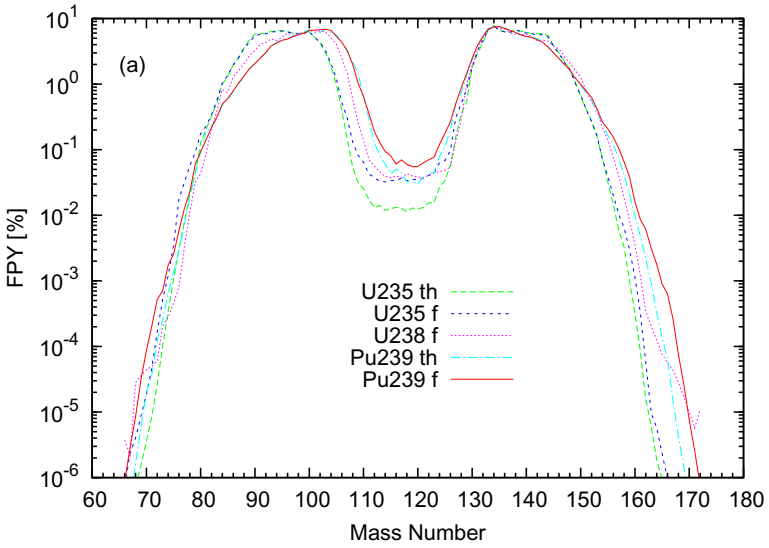

Figure 1.2: The distribution of fission products of uranium and plutonium. The green dashed line is relevant for the reactor considered in this research, as the most occuring fission is that of ^{235}U by thermal neutrons. ^{99}Mo is found in the left peak, and is one of the products with the highest yields. [2]

is the creation of ^{99}Mo from ^{98}Mo. This process (1.1) is referred to as neutron capture.

$$^{98}_{42}\text{Mo} + ^{1}_{0}\text{n} \rightarrow ^{99}_{42}\text{Mo} \tag{1.1}$$

Fission products

The fission products, usually 2 per event, have a specific probability of being produced in the process, as depicted in figure 1.2. ^{99}Mo can be found in the left peak, corresponding to a 6.1% yield. Obviously, after irradiation a range of fission products is available, so a selection step is needed to obtain the wanted products. The rest of the fuel can be treated as radioactive waste or be reprocessed. This waste (either the spent fuel or waste from the reprocessing process) is usually stored in special facilities.

Energy

The most well-known purpose of a nuclear reactor is probably the production of electrical energy. In every fission event, about 200 MeV [3] becomes available. This energy comes from the difference in binding energy between the uranium, and the fission products. In figure 1.3, the binding energy, the energy needed to divide the nucleus into individual protons and neutrons, per nucleon, is shown. The difference between the initial and final binding energy is approximately 200 MeV, in the form of kinetic energy of the fission products and neutrons, and radiation. By collisions, kinetic energy is converted to heat, which is converted into electrical energy in nuclear power plants. One of the benefits of using nuclear energy instead of conventional energy from coal, is the amount of fuel needed to produce the same amount of energy. A single gram of fully fissioned uranium corresponds to the burning of roughly 3000 kg of coal in terms of the production of energy.

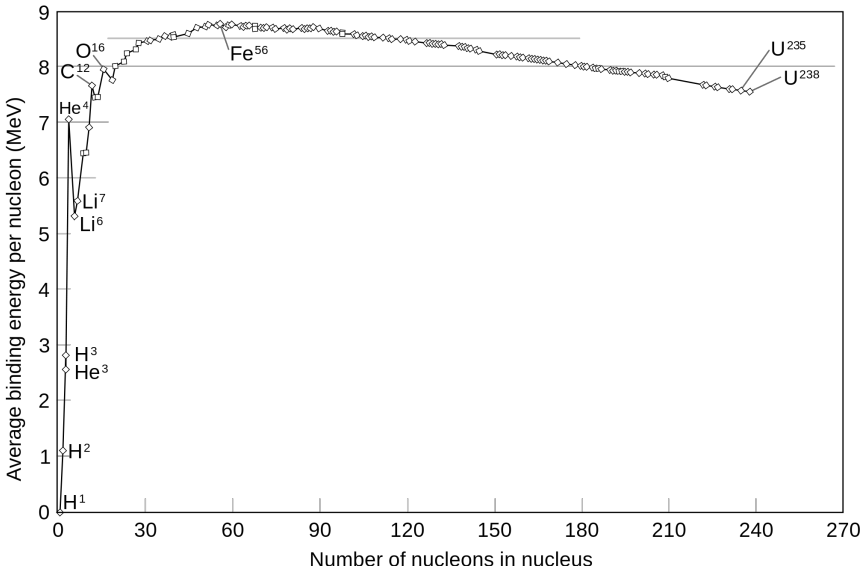

Figure 1.3: The binding energy per nucleon for common isotopes, ^{235}U is found at the right side of the graph. The products created by fission have a higher average binding energy per nucleon; the difference between the total binding energy before and after fission is the amount of energy that is released in fission.

1.2. MEDICAL ISOTOPES

The term *medical isotope* refers to an atom that can be used for diagnostics or medical treatments. A range of radioisotopes with different characteristics and half-life times is utilized for different purposes, but the most common isotope (used for medical diagnostics 30 million times a year worldwide) [4, 5] is ^{99m}Tc, in words Technetium-99 metastable. A metastable nucleus contains one or more nucleons in excited state. This particular radioisotope has a half-life of approximately 6 hours [3]. This relatively short lifetime implies that production of a large stock is useless, as after every day only 6.25% of the stock is left. As a consequence, continuous production and distribution of ^{99m}Tc is a prerequisite to be able to treat patients when necessary.

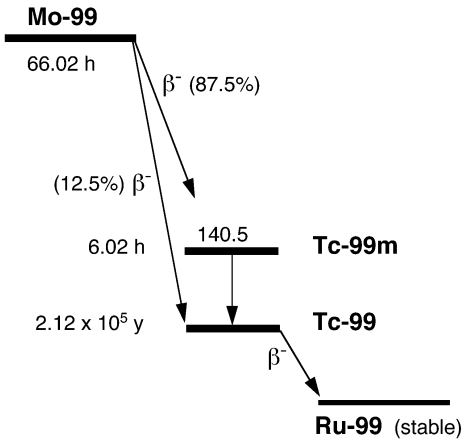

Figure 1.4: A schematic diagram of the process of the decay of the unstable isotope ^{99}Mo. All ^{99}Mo decays to ^{99}Tc, but the majority decays to the metastable isotope, ^{99m}Tc. The metastable product decays in its turn to ^{99}Tc, with a half-life of approximately 6 hours. ^{99}Tc itself is also not a stable isotope, but the half-life is several thousands of years [6].

^{99m}Tc is produced in the decay process of another isotope, ^{99}Mo, which has a half-life of 66 hours [3], see figure 1.4. The majority of this ^{99}Mo is produced in research reactors, where highly enriched uranium (HEU) targets are irradiated. After irradiation, the targets are transported to processing plants where ^{99}Mo is separated from the targets. Subsequently, the ^{99}Mo bulk is transported to a next facility where ^{99}Mo-^{99m}Tc generators are produced, which are finally transported to the customers [4].

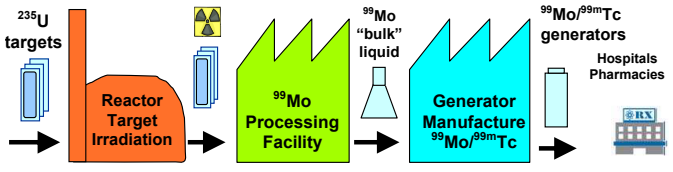

(a)

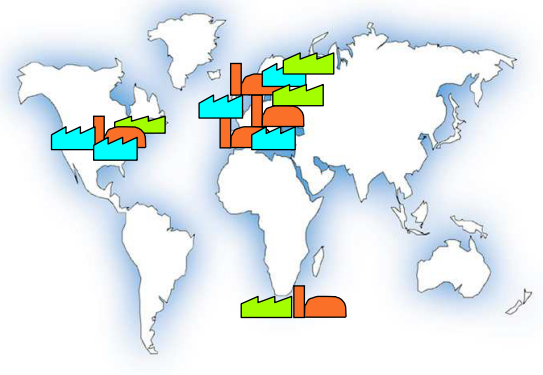

(b)

Figure 1.5: In the upper picture, the current process of molybdenum production is explained: the prefabricated targets are irradiated in a reactor and then transferred to a processing facility. There, the ^{99}Mo is extracted, so that it can be brought to a generator manufacturer. These generators are brought to the hospitals and farmacies, where the generator can be 'milked' to extract the ^{99m}Tc. The lower image shows the locations where the previously mentioned facilities can be found. Remarkably, some areas with a large number of inhabitants, such as southeast Asia and South America, are dependent on facilities far away. This causes logistical challenges and makes the supply line more vulnerable. (Images: [7])

The biggest producers of ^{99}Mo, NRU (Canada), HFR (the Netherlands), BR-2 (Belgium), SAFARI-1 (South Africa) and Osiris (France), together typically produce around 90-95% of the world demand [4]. Although the existing production sites of ^{99}Mo are currently capable of producing more than the world demand [8], there is no guarantee that all reactors can be operated when needed. Recent events underline that a drawback of having only a few production sites supplying almost the entire world is a vulnerability. Also, the number of processing plants makes the production line vulnerable. A recent example of the possible problems is the ^{99}Mo supply crisis at the end of the last decade, induced by outages of reactors (both planned and unplanned) and the shutdown of a processing facility [4]. Because no stock exists, events like these immediately affect patients through postponed or cancelled appointments.

Although the demand for ^{99m}Tc is rising [9], the existing production reactors are planned to be decomissioned in the near future [10] (the earliest in 2015 and 2016 (Osiris and NRU) [11]). To avoid new crises, an investigation of future production methods is conducted. Wolterbeek et al. [12] compare eight different production routes; among the possible alternatives to the current method are

photonuclear reaction of ^{100}Mo, direct production of ^{99m}Tc by irradiation of ^{100}Mo with protons, gel generator technology and aqueous homogeneous reactors [4, 13].

In the light of the Non-Proliferation Treaty [14], which embodies a goal of achieving nuclear disarmament, the aqueous homogeneous reactor is an ideal substituent for current reactors considering its possibility to use low enriched uranium as fuel. Also it is capable of producing ^{99}Mo using only 1% of the uranium currently needed for a similar production in nuclear reactors [15].

In the Organisation for Economic Co-operation and Development (OECD) report on the path to a reliable supply chain a list of criteria for production methods is posed [11]. Just looking at the non-legal and non-economical criteria an assessment of the suitability of the AHR can be made:

- **Technology maturity**
  AHRs have been built and operated for over 50 years in different forms, with different fuels.
- **Production capacity**
  One small AHR (core volume of 40 liters) is capable of producing a sufficient amount of ^{99}Mo to satisfy the Dutch demand.
- **Processing**
  Extraction of the ^{99}Mo is achieved by an absorption process, with high yield (90%).
- **Logistics**
  Filtering and extraction can be done at the production site, eliminating a transport step.
- **Waste**
  Compared to traditional methods, only 1% of the waste is produced for a similar amount of ^{99}Mo.
- **Proliferation resistance**
  The AHR can be fueled with LEU, conform the Non-Proliferation Treaty.
- **Other isotope production potential**
  During irradiation, a wide range of products is created, so with adequate filtering it should be possible to extract other isotopes.

From this assessment, the conclusion can be drawn that the AHR is an important alternative for the future production of medical isotopes.

1.3. AQUEOUS HOMOGENEOUS REACTORS - AN OVERVIEW

LOPO - 1944

The homogeneous reactor was one of the first reactors built after the first nuclear reactor, the Chicago Pile-1, went critical. The first reactor of this type was constructed at the end of 1943, running on a uranyl sulfate solution containing uranium enriched to 14%, being referred to as the "water-boiler" for security reasons. This name might be misleading because it suggests that the solution boils, however the bubbles observed in the reactor were hydrogen and oxygen bubbles which arose from the radiolysis of the solvent, water. In 1944, the LOPO (for Low Power) went critical using a uranyl sulfate solution of 565 gram ^{235}U dissolved in 13 liters of light water contained in a sphere of 30 cm diameter. The abscence of an adequate cooling system and a shield limited the power to 50 mW. [16, 17]

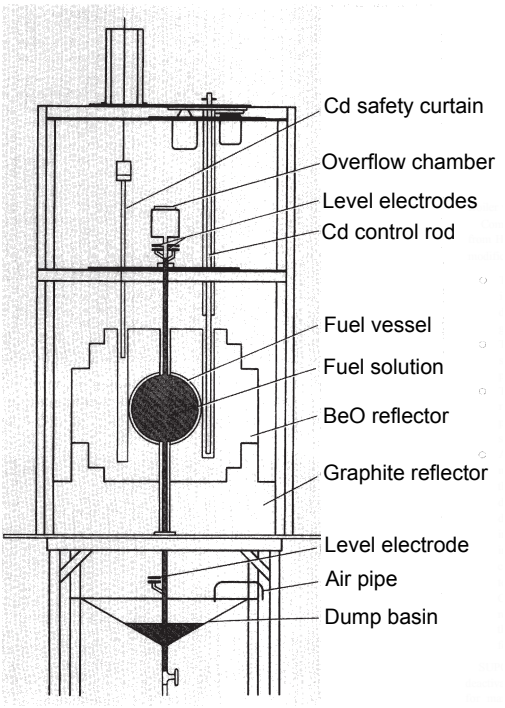

Figure 1.6: A schematic cross section of the Low Power AHR. The spherical reactor, filled with an uranyl sulfate solution, is surrounded by graphite and beryllium oxide reflectors. The fuel can be released from the core using the valve at the bottom of the dump bassin. A cadmium control rod is used to maintain criticality. [16]

HYPO - 1944

After dismantling the LOPO, a reactor called HYPO (for High Power) was constructed, which could be operated at a power level of several kW. With this reactor, cross section studies were performed, while the precursor was only used as a concept study and for determination of the critical mass. The fuel for the HYPO was contained in a similar stainless steel spherical shell with walls twice as thick as the LOPO, approximately 1.6 mm. The reflector was changed partly to a graphite thermal column, and cooling coils were added to be able to run the reactor at higher power. Moreover, the fuel was changed to an uranyl nitrate solution, containing 808 grams of ^{235}U in 13.65 L solution. Considering the intended experiments, a 'glory hole' was constructed, giving staff the possibility to place samples in the high flux areas of the reactor. [17] The total construction costs for this reactor are estimated at $500,000. [16, 18]

SUPO - 1951

As the neutron flux requirements for experiments rose, the HYPO was modified in 1950 to perform at a higher power level with a higher neutron flux (35 kW and 10^{12}cm^{-2}s^{-1} respectively). The modifications included an improved cooling installation enhancing the removal of heat, a higher enrichment (88.7%), a replacement of the beryllium oxide parts of the reflector by graphite and the incorporation of a system to recombine H_2 and O_2 gasses to reduce the risk at explosions. Eventually, SUPO (short for Super Power) was taken out of operation in 1974. Along with material experiments, also the transient behavior of the reactor was investigated. Reactivity increases led to an increase in gas production, resulting in a lower density in the fuel solution, reducing the moderating ability and therefore leading to a decrease in reactivity. This negative void reactivity coefficient is an important inherent safety aspect of the AHR. [16]

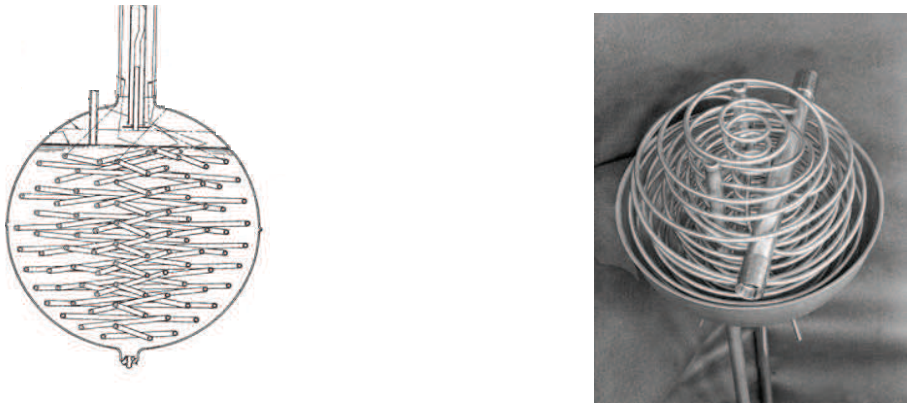

(a) (b)

Figure 1.7: In the schematic cross section the large amount of cooling water containing coils can be seen. The image on the right is an actual picture taken from the SUPO reactor. The tube that is placed in the middle of the reactor is the previously mentioned 'glory hole'. [19]

HRE - 1952

From 1952 to 1954, the Homogeneous Reactor Experiment - 1 (HRE-1) reactor was operated. In these 2 years, the nuclear stability of a fuel-circulating reactor was demonstrated, at power levels of several hundreds of kilowatts. The fuel, a 93% enriched uranyl sulfate solution, was circulated through the core at a rate of approximately 40 L min^{-1}. The core was a vessel of 45 cm diameter put in a pressure vessel, and the reactor used heavy water as a reflector. Steam produced in a heat exchanger powered a turbine, leading to an electrical power output of 140 kW. During experiments the discovery that a copper catalyst helps to recombine produced oxygen and hydrogen to water was made. The successor of the HRE-1, called HRE-2 or Homogeneous Reactor Test (HRT), had as main goal to prove the ability to run a homogeneous reactor continuously (an important characteristic for the reactor designs considered in this thesis), along with other goals such as testing methods for removal of fission and corrosion products. Uranyl sulfate was still used as fuel, but this time heavy water rather than light water was used as a solvent. During steady state operation, power excursions occurred, temporarily raising or lowering the reactor power. Investigation of these excursions showed that they were initiated by movement of uranium through the core. [17, 20]

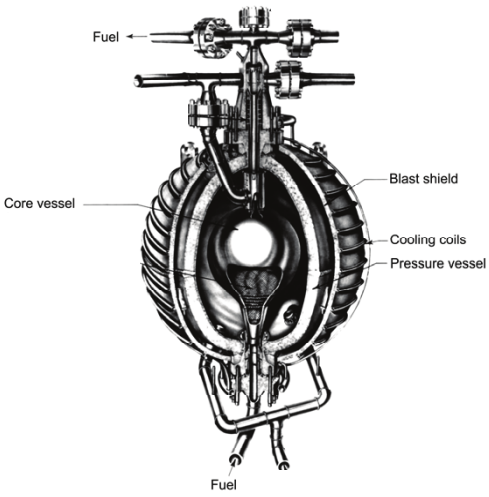

(a) The most important geometry features of the Homogeneous Reactor Test. The core vessel, 81 cm in diameter, is made of zircaloy 2 because of this material's small neutron absorption cross section. The pressure vessel and blast shield, which is surrounded by the cooling coils, have a diameter of 152 and 188 cm, respectively.

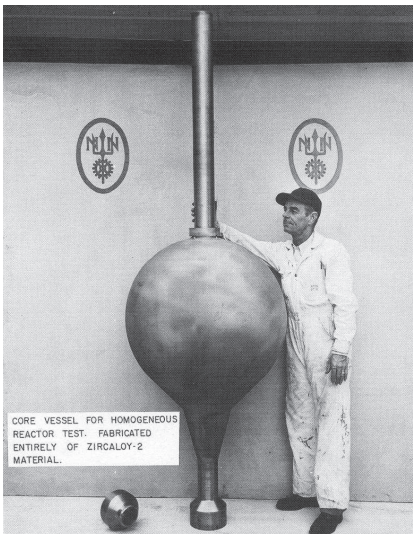

(b) The actual size and shape of the core vessel of the HRT. The vessel was constructed by a shipbuilding company in Virginia. The pressure vessel and blast shield are wrapped around this core.

Figure 1.8: The HRT, a schematic overview and an actual photograph [20].

ARGUS - 1981

ARGUS is a Russian research reactor located at the Kurchatov Institute, operated at a power of 20 kW. Its purposes are research and production of radionuclides such as ^{99}Mo and ^{89}Sr. The fuel, a uranyl sulfate solution, is contained in a cylindrical core placed within a graphite reflector. Originally, the fuel for ARGUS contained 93% enriched uranium, but a schedule for conversion to 19.8% enriched uranium has been drawn. A full conversion should be completed by June 2015, with a total cost of approximately $ 2,000,000. After this modification, the power will be decreased somewhat (10 - 20 %). [21]

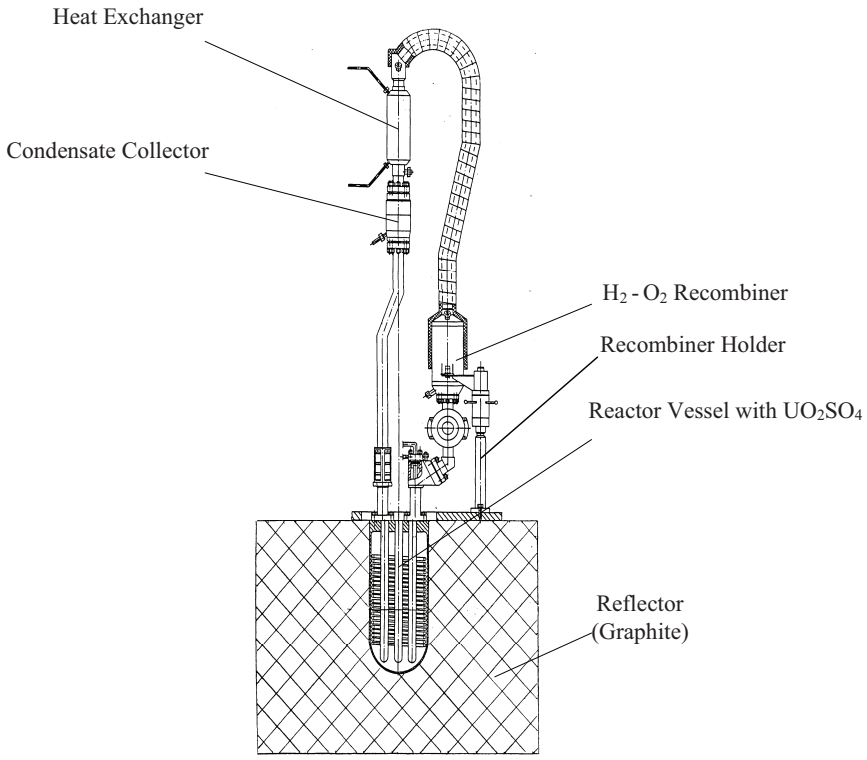

Figure 1.9: An overview of the ARGUS reactor, displaying the core and attached circuits. An eminent feature is the geometry of the core. Whereas previously mentioned reactors all had a spherical core, the ARGUS reactor has a cilindrical one with a hemisphere attached at the bottom. Radiolytic gas produced in the reactor flows through the H_2-O_2 recombiner, condensates and then returns to the fuel solution as water. [21]

SILENE - 1974

SILENE was originally designed to investigate accidents originating from situations in which suddenly a critical mass is reached. The core consists of a cyclindrical tank containing the fuel solution, with a small annular cylinder for the control rod in the center. The fuel solution is a 71 gram per liter uranyl nitrate solution, with an enrichment of 93%. Traditionally, the reactor was used to study criticality accidents, simulated by retracting the control rod. Three operation modes are the *pulse* mode, the *free evolution* mode and the *steady state* mode. In pulse mode, the control rod is retracted quickly, leading to a short power excursion to a very high level. In free evolution mode, the control rod is removed more carefully, while in steady state mode the reactor operates for a longer time at a certain power level. [22]

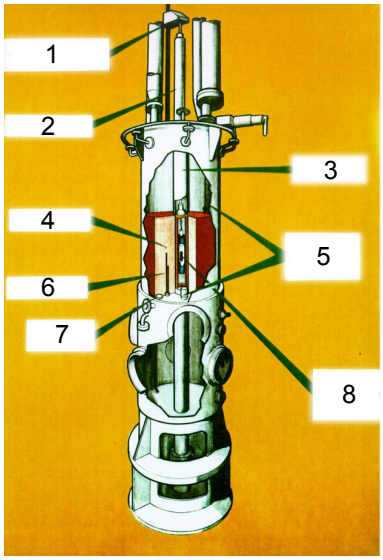

Figure 1.10: The layout of the reactor part of the SILENE facility. The rod drive mechanisms (1) at the top are used to move the control rod (2) up and down the central axial channel (3). The height and temperature of the fissile solution (4) are tracked by the level measurement devices (5) and thermocouples (6), to pass information on the state of the reactor. (7) is a pressure transducer, and (8) is a test capsule in which samples can be put in the center of the reactor to be irradiated. [23]

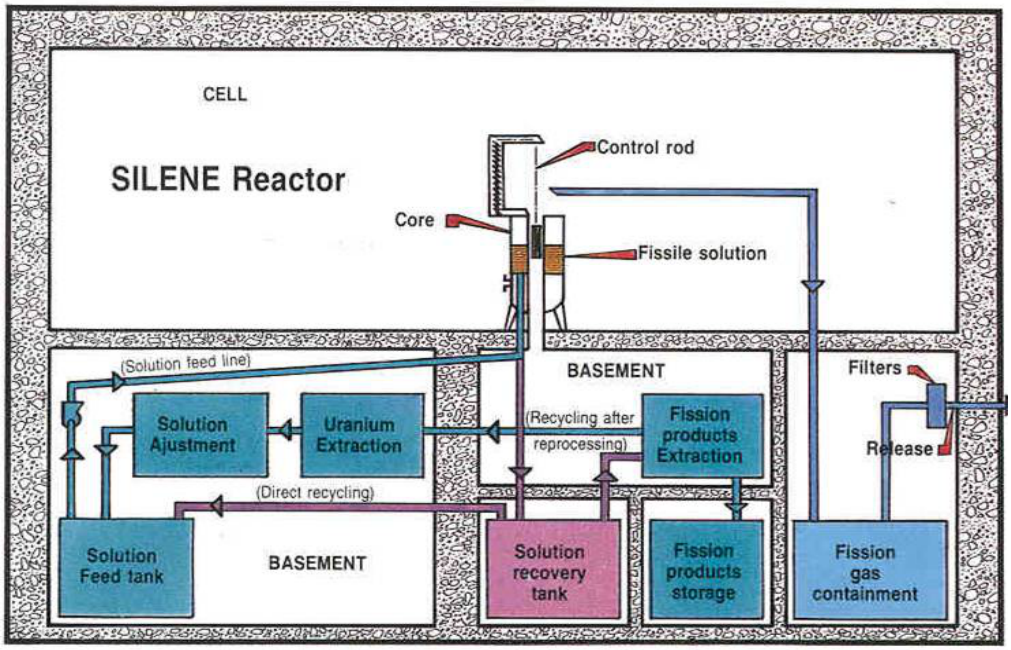

Figure 1.11: An overview of the SILENE reactor. The processing facilities are found one floor below the reactor itself. Fission products and fission gases are extracted, and the solution is reprocessed to be reinserted. The actual reactor, displayed on the upper floor in this figure, is shown in more detail in figure 1.10. [23]

MIPR BY NPIC

The Medical Isotopes Production Reactor concept as designed by the Nuclear Power Institute of China uses 100 L of a 90% enriched uranyl nitrate fuel solution in a cylindrical vessel (70 cm diameter and 73 cm height) and operates at 200 kW in steady state, while the power is controlled by a control rod. On average, the fuel temperature is around 343 K; well below the boiling point. Running for 100 cycles a year consisting of a 24 hour running period and a 48 hour shutdown, the annual production is 100,000 curies of ^{99}Mo, which corresponds to 220 6-day curie per cycle. The reactor fuel can be either a uranyl sulfate or uranyl nitrate solution, and both LEU and HEU can be used. In practice, a uranyl nitrate solution is chosen to ease the extraction process. [24, 25]

SAMOP

The Subcritical Assembly for Molybdenum Production, abbreviated SAMOP, consists of a 25.7 liter core tank surrounded by graphite reflectors, filled with 22.7 liters of uranyl nitrate solution. This entire system is placed in a tank filled with water for cooling purposes. The critical uranium concentration depends on factors as the thickness of the reflector and the placement of the reactor in the cooling tank, but has a minimum value of 300 gram 20% enriched uranium per liter. After irradiation, the fuel is first stored for some time in the delay tank, subsequently the molybdenum is extracted in the extraction column. In the reconditioning facility, the remainder of the solution is reconditioned and prepared to be reinserted in the reactor. [26]

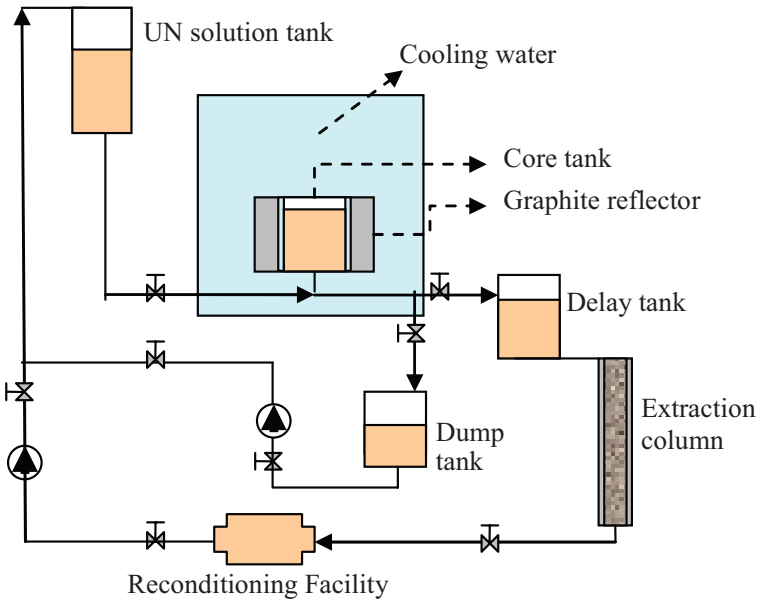

Figure 1.12: In the schematic above, the entire production process of ^{99}Mo is displayed. The uranyl nitrate solution flows from the storage tank to the reactor. After irradiation the fuel 'cools down' in the delay tank, before the ^{99}Mo is extracted [26].

SHEBA

SHEBA, Solution High-Energy Burst Assembly, is a homogeneous reactor located at Los Alamos National Laboratory, New Mexico. The core consists of a cylinder (diameter 49 cm, fuel height 43-45 cm) with a boron carbide control rod in the center, surrounded by the fuel, either a uranyl fluoride solution of 5% enrichment or a uranyl nitrate solution of 20% enrichment. A short list of goals of the SHEBA project is provided by Capiello, topped by 'study the behavior of nuclear excursions in a low-enrichment solution'. To achieve this goal, SHEBA is often operated in a free run to simu-

late accidents. Though the methods show similarities to the experiments at the SILENE reactor, the experiments vary at an important aspect: the level of enrichment. [27, 28]

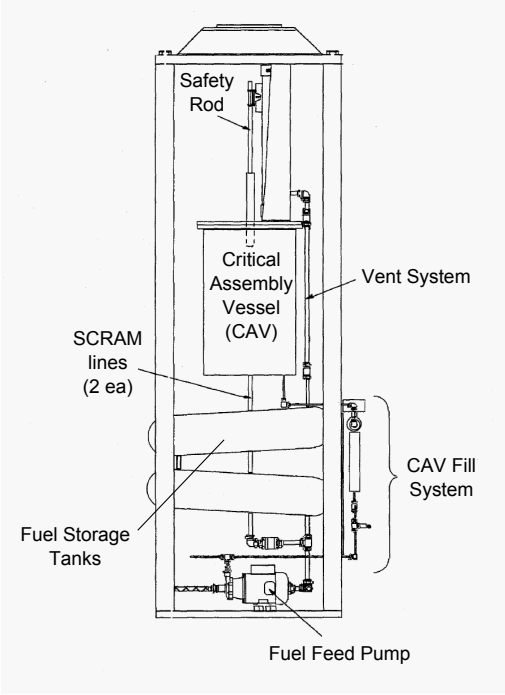

Figure 1.13: The shown design of the SHEBA reactor is quite simplistic. The most important features displayed are the cylindrical reactor vessel, the underlying fuel storage tanks and a safety rod that is dropped into the reactor in case of a criticality accident. [28]

1.4. DESIGN CONSIDERATIONS

The amount of ^{99}Mo produced is expressed in a somewhat odd-looking unit, the *6-day curie*. A curie corresponds to $3.7{\cdot}10^{10}$ decays per second while the prefix *6-day* indicates that it is the activity six days after the molybdenum has left the processing facility. Worldwide, the demand is estimated at 10,000 6-day curies per week, of which the majority is used in North America [9]. In the Netherlands, approximately 400,000 diagnostical treatments using ^{99m}Tc are carried out annually [10], which is roughly 1.5% of the total amount of treatments worldwide. Therefore, it is reasonable to assume that a production capacity of 2% of the world demand will suffice to satisfy the Dutch market. This capacity is higher than the currently needed capacity to anticipate increases in demand, which are estimated to be around 25% for a mature market [11]. Concluding, one of the requirements of the AHR design is a production of at least 200 6-day curies per week. Because the term 6-day curie refers to the activity at the time that the molybdenum leaves the facility, the total production rate needed is dependent on the interval between the cycles of processing campaigns.

$$Q = e^{\frac{\ln(2)}{t_h} t_s} \left(1 - e^{\frac{\ln(2)}{t_h} \Delta t}\right) \frac{p}{C} = 5.95 \cdot 10^{-12} \left(1 - e^{\frac{\ln(2)}{t_h} \Delta t}\right) p \tag{1.2}$$

Here, C is the conversion to the unit curie, $3.7{\cdot}10^{10}$, p the production rate in particles per second flowing out of the reactor and t_s, t_h and Δt denoting six days, the half-life time and the time between the harvests respectively. Comparing two situations, a daily and a weekly harvest, the production rates have to be $2.154{\cdot}10^{13}$ (daily) or $4.056{\cdot}10^{13}$ (weekly) atoms per second.

1.5. AIM OF THIS PROJECT

As discussed before, the vulnerability of the current supply chain of ^{99}Mo is the limited amount of production and processing facilities. If an AHR is used to produce ^{99}Mo at a smaller scale than in the current production facilities, the reliability of the supply chain will be improved because of two reasons. First, the number of production facilities is increased, which means that an outage of one reactor has a smaller effect on the total production. Second, the irradiated fuel can be processed at the production site, eliminating the need for separate processing facilities and simplifying the production process as a result. Therefore, an AHR which can produce approximately 2% of the global demand is designed. The design proposed by Huisman [29] is optimized, while additions to the computational model are made to approximate reality more closely. A leading goal is:

To design an aqueous homogeneous reactor which can produce approximately 2 percent of the global demand of ^{99}Mo.

2

THEORY

2.1. FUEL SOLUTION

The fuel of an aqueous homogeneous reactor is an uranyl salt dissolved in water. Looking at earlier reactors, the choice of salt is narrowed down to uranyl nitrate ($UO_2(NO_3)_2$), uranyl sulfate (UO_2SO_4) and uranyl fluoride (UO_2F_2), which have all proven to be appropriate candidates. A comparison between the characteristics of the salts has to be made to determine the most ideal fuel. In general, lowering the pH of the solution will increase the solubility of the uranyl salts. [17]

Uranyl nitrate

Uranyl nitrate was used as a fuel in the HYPO and SUPO reactors [16] and is the primary choice for the SAMOP reactor [30]. ^{99}Mo is more easily extracted from an uranyl nitrate solution than from uranyl sulfate because the distribution coefficient K_d, the ratio of ^{99}Mo absorbed to the concentration ^{99}Mo in the solvent, is higher for a uranyl nitrate solution. This is because competition for adsorption sites between molybdenum and sulfate is stronger than between molybdenum and nitrate [15, 31]. Regarding the production of radiolytic gas, a uranyl nitrate solution brings additional difficulties, since besides H_2 and O_2, nitrogen oxide (NO_x) gases are formed [32]. Furthermore, a large increase of the pH is observed after irradiation. A pH too high can lead to precipitation of solutes present because of the decreased solubility [31].

Uranyl sulfate

Uranyl sulfate was used as fuel in the first AHR that reached criticality, the LOPO [16], and also in the HRE-1 and HRE-2 reactors. Less neutron absorption and a higher solubility were used as arguments in favor of using uranyl sulfate [17]. Although uranyl sulfate has a lower distribution coefficient than uranyl nitrate, implicating a less efficient separation of the produced molybdenum from the irradiated fuel, it is possible to extract ^{99}Mo from a uranyl sulfate solution with a purity of over 90% [31, 33].

Uranyl fluoride

Traditionally, uranyl fluoride is not often used in AHRs, but SHEBA was designed to have the possibility to run on UO_2F_2 [27]. Taking only neutron capture into account, uranyl fluoride is an excellent option because the capture cross section of fluorine is low compared to that of sulfate and nitrate. However, during irradiation hydrogen fluoride (HF) is produced, present in both liquid and vapor

phase, which is highly corrosive towards zirconium and titanium and to a lesser extent towards stainless steel [17]. Research has indicated that the use of uranyl fluoride indeed leads to corrosion of the stainless steel cladding [28].

The absorbtion cross sections of sulfur, fluorine and nitrogen for thermal neutrons are listed in table 2.1 [34], while table 2.2 summarizes the advantages and drawbacks of the treated salts.

Table 2.1: Relevant microscopic absorbtion cross sections (for thermal neutrons) of the constituent atoms of the salts. For the atoms N, F, S and O, the cross section is given for a mixture of isotopes.

Isotope	**Cross section (barn)**
N	1.9
F	0.0096
S	0.53
O	0.00019
^{234}U	100.1
^{235}U	680.9
^{238}U	2.68

Table 2.2: The benefits and drawbacks of the different salts.

$UO_2(NO_3)_2$	+	Easier ^{99}Mo extraction compared to uranyl sulfate
	+	Extensive knowledge through use in earlier reactors
	–	Production of additional gaseous products (NO_x)
	–	pH fluctuations, possible precipitation
UO_2SO_4	+	Extensive knowledge through use in earlier reactors
	+	pH stable upon radiation
	–	Efficiency of ^{99}Mo extraction slightly lower compared to uranyl nitrate
UO_2F_2	+	Low neutron capture cross section
	–	Production of HF, which causes corrosion

THE INFINITE MULTIPLICATION FACTOR k_∞

To gain more insight into the neutronic properties of the aforementioned salts the multiplication value can be investigated. This is done for the three salts, treated as an infinite homogeneous material. The parameter that is changed during the comparison is the uranium concentration, which is set equal for all salts. This implies that, because of differences in molecular weight and density, the volumetric percentage occupied by water is different for each salt. In figure 2.1, the infinite multiplication factor is shown for different salts and different concentrations of uranium.

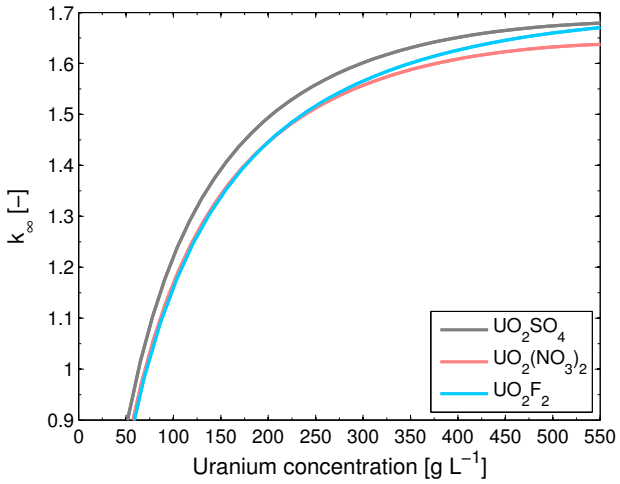

Figure 2.1: The value of k_∞ versus the concentration of the different salts, expressed in grams of uranium per liter, for an enrichment of 20%. The differences between the curves are caused by distinct cross sections, molecular weights and densities. These last two also affect the volume fraction of water.

EXTRACTION

Regarding the fact that the ^{99}Mo is dissolved in the fuel solution after irradiaton, a method is needed to extract the ^{99}Mo from that solution. Proposed techniques rely on chemical sorbtion processes in which two aspects are important: the capture yield (the fraction of the ^{99}Mo in the fuel solution that is captured by the sorbtion material) and the stripping yield (the fraction of the ^{99}Mo that can be recovered from the sorbtion material). Alumina was traditionally used as sorbent for molybdenum recovery, but currently some specifically designed sorbent materials are available for this purpose.

In 1999, Ponomarev-Stepnoy et al. claimed the invention of an AHR using a uranyl sulfate fuel [33], as shown in figure 2.2, and a solid polymer sorbent to absorb the produced ^{99}Mo [35]. Using this sorbent, 99% of the ^{99}Mo in the fuel solution (with a pH of 1) can be absorbed, without absorbing any ^{235}U. However, whether they use a HEU or LEU fuel is not mentioned in the patents.

Vandegrift et al. [36] investigated four sorbents (alumina, Radsorb, Isosorb and PZC) to determine their efficiency in absorbing ^{99}Mo from uranyl nitrate and uranyl sulfate solutions. Radsorb,

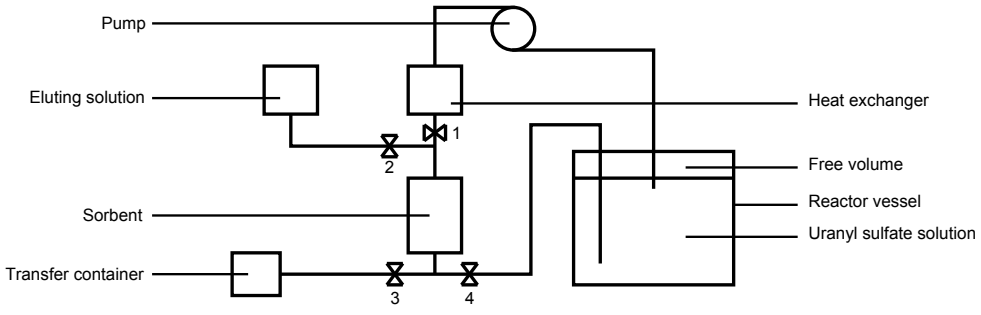

Figure 2.2: The most essential parts of the facility proposed by Ponomarev-Stepnoy et al. The fuel is pumped from the reactor vessel, through the heat exchanger to the column containing the sorbent. When the column is filled, valve 1 is closed. Subsequently, valve 4 is opened and the fuel (without the extracted ^{99}Mo) is returned to the reactor vessel. When no fuel is left in the sorbtion column, valve 4 is closed and valves 2 and 3 are opened. The molybdenum in the sorbtion column is solved in the eluting solution (a 10M nitric acid solution) and stored [33].

Isosorb [37] and PZC (polyzirconium compound) are solid sorbents, specifically designed for extraction of ^{99}Mo. The most important conclusions drawn from this experimental comparison are that a sorbent column can be used to efficiently extract ^{99}Mo from LEU uranyl sulfate and uranyl nitrate fuel solutions. Furthermore, it becomes clear that the specifically designed sorbents perform better than the alumina, and that separation of ^{99}Mo can be done more efficiently from uranyl nitrate solutions than from uranyl sulfate solutions.

A titanium based sorbent, TiO_2, has been introduced by Ling et al. [38] as an alternative for the traditional alumina sorbent used in the process of capture chromatography. It has a higher selectivity and capacity than alumina for ^{99}Mo in concentrated uranyl sulfate solutions. Both the capture and the stripping yield are approximately 95%.

Although the extraction of ^{99}Mo from an uranyl nitrate solution can be achieved more easily than from an uranyl sulfate solution, recent experiments have shown that ^{99}Mo can be extracted from uranyl sulfate fuel solutions with an efficiency larger than 90 % as discussed above. Therefore, from an extraction point of view, there is no preference for uranyl sulfate or uranyl nitrate as fuel.

Based on the aformentioned information, uranyl sulfate is chosen as fuel for the AHR. The uranyl fluoride solution is not considered as an appropriate option due to the possible corrosion, which can cause leaks. Also, there is less knowledge available on the subject of fission product separation. Uranyl sulfate is chosen because the disadvantages of using uranyl nitrate (possible precipitation and formation of NO_x gases) are considered larger than the disadvantage of uranyl sulfate (suboptimal extraction of ^{99}Mo).

pH ADJUSTMENT

As stated earlier, lowering the pH of the solution increases the solubility and therefore prevents precipitation. To lower the pH, an amount of acid is added, sufficient to reduce the acidity of the solution to a pH of 1. An ideal acid will split fully, so that a minimal amount of acid has to be added. The polyprotic sulfuric acid (H_2SO_4) seems a reasonable choice, as it fulfills this requirement while no difficulties as increased corrosion rates occur. Upon solving the acid one H^+ ion is split off:

$$H_2SO_4 \rightarrow H^+ + HSO_4^- \tag{2.1}$$

The HSO_4^- splits partly, i.e., it engages itself in an equilibrium with H^+ and SO_4^{2-}

$$HSO_4^- \leftrightarrow H^+ + SO_4^{2-} \tag{2.2}$$

with an equilibrium constant K_z of 0.01

$$K_z = \frac{[H^+]\,[SO_4^{2-}]}{[HSO_4{}^-]} \tag{2.3}$$

Solving equation (2.3) using the imposed constraint that the pH of the fuel solution should be equal to 1 $\left(\text{pH} = -\log[H^+]\right)$, approximately $9.7{\cdot}10^{-2}$ mole of sulfuric acid is needed in a liter of fuel solution.

2.2. RADIOLYTIC GAS PRODUCTION

A characteristic inherent to the AHR is the generation of gas in the fuel solution, due to the radiolysis of water. The slowing down of the fission fragments and neutrons in the liquid results in dissociation of water into H_2 and O_2, amongst others (such as hydrogen peroxide, H_2O_2) [39]. These products

can react with each other to form water again, however, for fission recoil particles this reaction is relatively slow [17]. In steady state operation, a stoichiometric composition of the gas bubbles can be assumed [40].

At a critical gas concentration in the solution, bubble production is induced in the tracks of the fission products. Previous studies conclude that gas bubbles are created with fixed radius, independent of parameters such as temperature, liquid pressure, surface tension, dissolved gas concentration and uranium concentration [41]. In aqueous solutions of uranyl salts, only a certain concentration of H_2 and O_2 can be dissolved. Even though the nucleation radius is independent of the dissolved gas concentration, the final dimension of the bubble is not. The radius of a radiolytic gas bubble grows or shrinks depending on the concentration of hydrogen and oxygen in the solution. In case of oversaturation, the bubble will grow, while an existing bubble will shrink when the solution is undersaturated [42]. If the gas concentration in the solution is lower than the critical gas concentration, the bubble will dissolve in 10^{-5} seconds. Values found in literature for the radius of a gas bubble differ: Souto et al. give a characteristic radius of $5 \cdot 10^{-7}$m [43], a nucleation radius of $5 \cdot 10^{-8}$m can be found [41], while Kimpland states that expansion within 10^{-5} seconds leads to a bubble size of $5 \cdot 10^{-13}$m^3, corresponding to a radius of approximately $5 \cdot 10^{-5}$m [39].

All radiolytic gas bubbles contribute to the total void volume in the reactor core. The amount of molecules of H_2 produced is dependent on the radiolytic yield. This value, $G(H_2)$, gives the number of hydrogen molecules produced per amount of fission energy and is a function of the uranium concentration [44]. Typical values are around 1 molecule per 100 eV of fission energy [42–44]. Assuming a stoichiometric composition of the bubbles, the amount of O_2 produced is half of the amount of H_2 produced. For a given total reactor power P, the amount of gas produced (in moles s^{-1}) can be written as

$$\left(1+\frac{1}{2}\right)\frac{G(H_2)}{qN_A}P \tag{2.4}$$

with N_A representing Avogadro's number and q the conversion factor between joule and electronvolt. Using the ideal gas law, the volume of the produced gas can be estimated. For the molar volume V_m, the equation

$$V_m = \frac{R_g T_g}{p_b} \tag{2.5}$$

can be written, where R_g is the gas constant, T_g the gas temperature and p_b the gas pressure inside the bubble, which is given by [45]

$$p_b = \frac{2\sigma}{r_b} + p_l \approx \frac{2\sigma}{r_b} \tag{2.6}$$

where σ is the surface tension and p_l the liquid pressure ($= \rho g h$). The approximation is justified, because p_l and $\frac{2\sigma}{r_b}$ are of the orders 10^3 Pa and 10^5 Pa, respectively. Combining (2.4), (2.5) and (2.6) gives the equation to calculate the total void volume production rate in the core:

$$V = \left(1+\frac{1}{2}\right)\frac{G(H_2)}{qN_A}\frac{R_g T_g r_b}{2\sigma}P \tag{2.7}$$

The created bubbles will not grow or shrink in a steady state case, as the dissolved gas concentration in the fuel solution stays at the saturation level. If the balance tips and there is an oversaturation, a gas bubble is formed, while a previously formed bubble shrinks in the case of undersaturation.

Souto et al. give a value of 500K for T_g [43]. However, Cooling et al. argue that this value represents the temperature of the gas just after nucleation of the bubble and that the bubbles cool down to the fuel temperature in a timescale of the order 10^{-8} seconds, which infers that the gas temperature is approximately equal to the local temperature of the fuel [46]. In table 2.3, (indicative) values

for the various parameters and constants are listed.

Table 2.3: An overview of parameters defining the production of a void volume

Quantity	Value	Unit	Reference
R_g	8.314413	$Jmol^{-1}K^{-1}$	[47]
T_g	500	K	[43]
N_A	$6.022045 \cdot 10^{23}$	mol^{-1}	[47]
q	$1.6 \cdot 10^{-19}$	$J\ eV^{-1}$	[48]
σ	$7 \cdot 10^{-2}$	Nm^{-1}	[49]
$G(H_2)$	$8 \cdot 10^{-3}$	molecules eV^{-1}	[44]
r_b	$5 \cdot 10^{-7}$	m	[43]

BUBBLE SPEED

The speed of the bubbles in the fluid is an important characteristic needed to estimate the time the bubbles stay in the fluid, which gives information about the total void volume in the fuel solution in the core. Three forces working on the bubbles are the buoyancy force F_b, gravitational force F_g and the drag force F_d, the latter calculated using the Rybczynski formula [50]. As soon as these forces cancel each other out, the bubble will have achieved its final speed.

$$F_b = \frac{4\pi}{3} r_b^3 (\Delta\rho) g = \frac{4\pi}{3} r_b^3 (\rho_f - \rho_g) g \tag{2.8}$$

$$F_d = 6\pi\mu_f \frac{2\mu_f + 3\mu_g}{3\mu_f + 3\mu_g} r_b v_b \tag{2.9}$$

where ρ is the density, μ the viscosity and subscripts f and g denote the fuel and gas, respectively. Because $\rho_f >> \rho_g$ and $\mu_f >> \mu_g$, F_b and F_d can be rewritten:

$$F_b \approx \frac{4\pi}{3} r_b^3 \rho_f g \tag{2.10}$$

$$F_d \approx 4\pi\mu_f r_b v_b \tag{2.11}$$

After equating (2.10) and (2.11) and rewriting, an expression for v_b is found:

$$v_b = \frac{g}{3} \frac{\rho_f}{\mu_f} r_b^2 \tag{2.12}$$

Inserting the values presented in table 2.3, the gravitational acceleration (9.80665 ms^{-2} [47]) and specific values for a uranyl sulfate fuel solution containing 251 g/L uranium ($\rho_f \approx 1.39$ g cm^{-3}, calculated using the protocol described in section 2.4, and $\mu_f \approx 1.4 \cdot 10^{-3}$ Pa·s [49]), a relative speed of approximately 10^{-6} m s^{-1} is obtained. Regarding the low speed of the bubbles relative to the fuel and the limited time a certain amount of fuel is in the reactor, the bubbles are assumed to be dragged along with the fuel flow, moving at the same speed.

2.3. BOUSSINESQ APPROXIMATION

Temperature differences can lead to a space-dependent density profile of a fuel. As a general rule, an increase in temperature leads to an expansion of the volume, which is equivalent to a decrease in density. These fluctuations in density can lead to a buoyancy-driven flow, often referred to as natural convection [45]. In the Boussinesq approximation, only the density change in the term where

density is multiplied by the gravitational constant is taken into account; effects on inertia resulting from density differences are neglected. In this approximation, the density at any temperature is evaluated by

$$\rho = \left(1 - \beta \Delta T\right) \rho_0 \tag{2.13}$$

$$\beta = -\frac{1}{\rho}\left(\frac{\partial \rho}{\partial T}\right) \tag{2.14}$$

where ΔT is the temperature difference between the local temperature T and the reference temperature T_{ref} at which ρ_0 is evaluated; β, as given in (2.14), is the coupling between the temperature difference and the corresponding density difference, called the *thermal expansion coefficient*.

This coefficient is not constant over the range of temperatures relevant for the fuel solution. Orban et al. [49] give an overview of densities of uranyl sulfate solutions for a variety of temperatures and concentrations. The experimental results show a relation between density and temperature, which can be approximated by a quadratic function. After this function has been determined it's little effort to produce the expansion coefficient over a range of temperatures, as shown in figure 2.3. The density of the fuel after a slight temperature difference δT, the transition from $\rho(T_0)$ to $\rho(T + \delta T)$, is given by $\rho(T_0)(1 - \beta(T_0)\delta T)$.

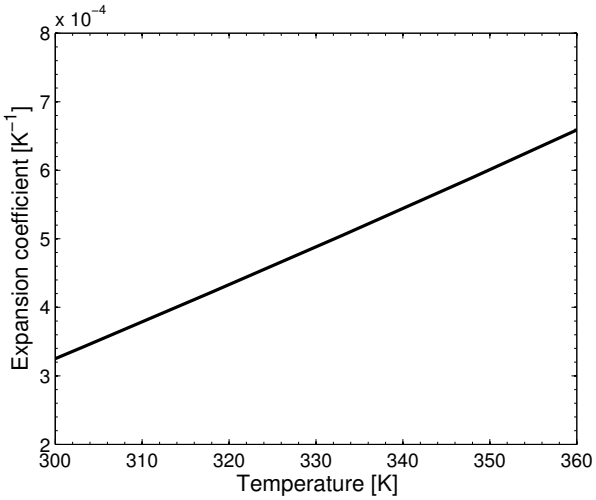

Figure 2.3: The expansion coefficient of the fuel, β, as a function of the temperature. Using experimental data on densities provided by Orban et al. [49], a quadratic fit of density as a function of temperature is made, from which this graph can be deducted using (2.14).

Considering only the first order effects (the higher order effects are negligible), the density at temperature T can be calculated using

$$\rho(T) = \rho(T_{\text{ref}})\left(1 - (T - T_{\text{ref}})\beta(T_{\text{ref}})\right) \tag{2.15}$$

In the aqueous homogeneous reactor, however, another mechanism leading to density fluctuations is present. Due to the production of bubbles filled with radiolytic gas, the density decreases. In an *unvoided* volume V_0, radiolytic gas production can be represented by the transition of a certain volume of solvent (water) to a volume of gas: the dissipated volume of water and the created void volume, both containing the same mass m_{trans}, are given by

$$V_{\text{diss}} = \frac{m_{\text{trans}}}{\rho_{\text{water}}} \tag{2.16}$$

$$V_{\text{void}} = \frac{m_{\text{trans}}}{\rho_{\text{void}}} \tag{2.17}$$

The void fraction α can be calculated by dividing the void volume by the total volume

$$\alpha = \frac{V_{\text{void}}}{V_0 - V_{\text{diss}} + V_{\text{void}}} \tag{2.18}$$

which can be rearranged to give

$$V_{\text{void}} = \frac{\alpha V_0}{(1-\alpha) + \alpha \frac{\rho_{\text{void}}}{\rho_{\text{water}}}} \tag{2.19}$$

$$V = \frac{V_0}{1 + \alpha\left(\frac{\rho_{\text{void}}}{\rho_{\text{water}}} - 1\right)} \tag{2.20}$$

Equation (2.20) gives the ratio between the *unvoided* volume and the *voided* volume. Because density is inversely proportional to volume, this expression can be used to write ρ as a function of ρ_0

$$\rho = \left(1 + \alpha\left(\frac{\rho_{\text{void}}}{\rho_{\text{water}}} - 1\right)\right)\rho_0 \tag{2.21}$$

Due to the fact that $\rho_{\text{void}} << \rho_{\text{water}}$ this boils down to

$$\rho = (1-\alpha)\,\rho_0 \tag{2.22}$$

The analogy with equation (2.13) can easily be seen. Combining the thermal and void effects, the density can be calculated using

$$\rho = \rho_0\left(1 - \beta_0 \Delta T\right)(1-\alpha) \approx \rho_0(1 - \beta_0 \Delta T - \alpha) \tag{2.23}$$

considering only first order effects.

For the traditional Boussinesq approximation, the correction factor $\beta\Delta T$ should be small ($\beta(T - T_{\text{ref}}) << 1$). With the temperature differences considered in this project, of the order of 20K and with a typical β of $5{\cdot}10^{-4}$, this condition is fulfilled. Assuming a similar condition applies to the void correction factor, the validity of (2.23) can be tested by looking at the void percentages. These are of the order 10^{-2} to 10^{-1}, comparable to the values of $\beta(T - T_{\text{ref}})$.

2.4. FUEL DENSITY CALCULATION

The density of the fuel solution for an unvoided reactor at the reference temperature mainly depends on the concentration of uranyl salt dissolved. Following for the most part the method described by Sutondo [51], the procedure for calculation of the fuel density is shown in this part.

The fuel solution can be split into two general components; the salt and the water, each with its own density. As the uranium concentration of the fuel usually is given, the amount of salt (in gL^{-1}) present can be calculated by

$$c_{\text{salt}} = c_U \frac{M_{\text{salt}}}{M_U} \tag{2.24}$$

where M denotes the molar mass. The molar mass of uranium is a function of the enrichment, i.e., the percentage of the lighter isotopes ^{234}U and ^{235}U. For an enrichment p, the weight fractions in uranium are given by

$$\begin{aligned} f_{(^{234}U)} &= 8.4400 \cdot 10^{-3} p - 7.0084 \cdot 10^{-4} \\ f_{(^{235}U)} &= p \\ f_{(^{238}U)} &= 1 - f_{(^{235}U)} - f_{(^{234}U)} \end{aligned} \tag{2.25}$$

so the molar masses of this enriched uranium and of the salt are equal to:

$$\begin{aligned} M_U &= f_{(^{234}U)} M_{(^{234}U)} + f_{(^{235}U)} M_{(^{235}U)} + f_{(^{238}U)} M_{(^{238}U)} \\ M_{\text{salt}} &= M_U + 6M_O + M_S \end{aligned} \tag{2.26}$$

With the molar mass and the density of the salt known, the volume fraction of the salt can easily be obtained using

$$v_{\text{salt}} = \frac{c_{\text{salt}}}{\rho_{\text{salt}}} = \frac{c_U}{\rho_{\text{salt}}} \frac{M_{\text{salt}}}{M_U} \cdot \frac{1}{V} \tag{2.27}$$

where v is the volume fraction and V the total volume considered, in this case 1 dm^3, which implies that the volume fraction of water is given by

$$v_{H_2O} = 1 - v_{\text{salt}} \tag{2.28}$$

This means the concentration of water can be written as

$$c_{H_2O} = v_{H_2O} \frac{V}{\rho_{H_2O}} \tag{2.29}$$

with ρ evaluated at the reference temperature. The density of the fuel for a certain concentration of uranium can then be calculated using

$$\rho_{\text{fuel}} = v_{\text{salt}} \cdot \rho_{\text{salt}} + v_{H_2O} \cdot \rho_{H_2O} \tag{2.30}$$

With the knowledge of the volumes occupied by the solute and solvent, the number densities can be calculated in the following way:

$$\begin{aligned} N_{(^{234}U)} &= \frac{c_{\text{salt}}}{M_{\text{salt}}} f_{(^{234}U)} N_A \\ N_{(^{235}U)} &= \frac{c_{\text{salt}}}{M_{\text{salt}}} f_{(^{235}U)} N_A \\ N_{(^{238}U)} &= \frac{c_{\text{salt}}}{M_{\text{salt}}} f_{(^{238}U)} N_A \\ N_{(S)} &= \frac{c_{\text{salt}}}{M_{\text{salt}}} N_A \\ N_{(H)} &= 2 \frac{c_{H_2O}}{M_{H_2O}} N_A \\ N_{(O)} &= 6 \frac{c_{\text{salt}}}{M_{\text{salt}}} N_A + \frac{c_{H_2O}}{M_{H_2O}} N_A \end{aligned}$$

with $N_{(x)}$ in dm^{-3}.

2.5. GEOMETRY

The basis of the isotope production facility is a cylindrical reactor vessel, placed inside a larger vessel filled with water. An aqueous solution of uranyl salt is used as fuel and is pumped through the reactor vessel continuously. Huisman [29] describes four designs of the reactor vessel and comes up with a best choice of those four. This choice is taken as a starting point in this research.

The reactor vessel is a vertical cylinder of radius 20 cm with a height of 60 cm, of which the lower 40 cm is occupied by fuel solution and the upper 20 cm by air. The volume that is occupied by fuel can be subdivided into five parts: four inflow annuli and one outflow pipe. Each annulus has a width Δr of 4 cm, with the lower 10 cm of the inflow annuli only 2 cm wide. The outflow pipe is situated in the center of the core so that the inflow volume is 96% of the total fuel volume, and the outflow volume only 4%. Stainless steel is used as construction material for the reactor.

The fuel is pumped through the reactor with a mass flow rate set at 0.40 kg s^{-1}. With a fuel density of approximately 1300 kg m^{-3} and the total area of the inflow annuli 0.121 m^2, this means that the average speed in the inflow annuli is of the order of several mm s^{-1}. The outflow area is 24 times as small, while the mass flow rate is equal: the average outflow speed is of the order of several cm s^{-1}.

All fuel flowing out will be processed and subsequently re-inserted in the reactor. Two important parts of the processing step are the extraction of fission products and the cooling of the fuel. External cooling is needed, because the heat flow from the reactor to the surroundings is insufficient to transfer all fission heat to the environment. The quicker the reprocessing can be done, the less fuel solution is needed.

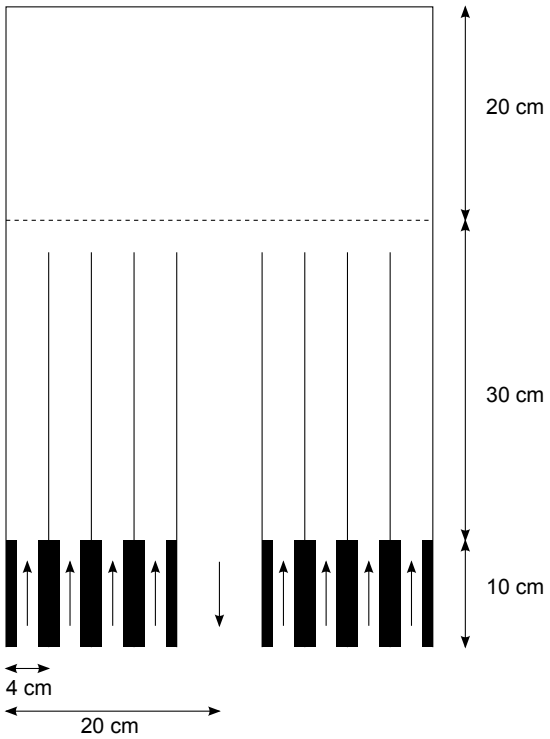

Figure 2.4: The geometry of the reactor vessel through which the fuel solution is pumped. The arrows indicate the direction of the flow; the dashed line shows the fuel level. Between the inlets coaxial vertical walls are placed, to guide the fuel.

2.6. TEMPERATURE DISTRIBUTION AND COOLING

An important safety characteristic of the reactor is the temperature distribution. Local boiling, caused by a high local temperature, can cause unwanted effects like slushing.

The water outside the reactor vessel is contained in a stainless steel tank (hereafter referred to as water vessel) and heats up due to the conduction of heat from the fuel through the wall of the inner vessel (referred to as reactor vessel). Induced by buoyancy effects, this water starts to circulate, hot parts moving upwards and cool parts downwards. By conduction of heat, the water vessel wall is heated, and when this wall has a temperature higher than the ambient temperature, the heat is transferred to the surrounding air.

To determine the amount of heat flow from the cylindrical wall to the surrounding air, knowledge about the heat transfer coefficient is essential. Useful information on this subject can be found in the book *Fundamentals of Momentum, Heat, and Mass Transfer* [52]. A detailed explanation of Nusselt numbers for different geometries is given, from which the ones applicable to the aforementioned configuration can be calculated.

An equation found by Churchill and Chu through investigation of experimental data can be used to calculate the Nusselt number for a vertical plate, but also for a vertical cylinder, provided the dimensions of the cylinder dimensions obey the following condition

$$\frac{D}{L} \geq \frac{35}{\mathrm{Gr}^{\frac{1}{4}}} \tag{2.31}$$

where D and L are the characteristic diameter and length (in this case the height), and Gr the Grashof number. The Churchill-Chu relation provides the Nusselt number as a function of both the Rayleigh and the Prandtl number

$$\mathrm{Nu} = \left(0.825 + \frac{0.387\mathrm{Ra}^{\frac{1}{6}}}{\left(1 + \left(\frac{0.492}{\mathrm{Pr}}\right)^{\frac{9}{16}}\right)^{\frac{8}{27}}} \right)^2 \tag{2.32}$$

Aside from heat transfer from the vertical water vessel wall, the heat transfer from the circular top (horizontal) of the water vessel has to be considered. The bottom is considered to be insulated implicating no heat flux occurs here. The relation for the Nusselt number for a horizontal plate is easier than that for a vertical plate, but is different for different ranges of the Rayleigh number

$$\mathrm{Nu} = 0.54\mathrm{Ra}^{\frac{1}{4}} \quad \text{if} \quad 10^5 < \mathrm{Ra} < 2 \cdot 10^7 \tag{2.33a}$$

$$\mathrm{Nu} = 0.14\mathrm{Ra}^{\frac{1}{3}} \quad \text{if} \quad 2 \cdot 10^7 < \mathrm{Ra} < 3 \cdot 10^{10} \tag{2.33b}$$

With the knowledge obtained about the Nusselt numbers and the geometrical properties, the relation between the total heat flow and the temperature difference (with T_∞ the temperature far away from the cylindrical water vessel) can be specified

$$q = \left(\mathrm{Nu}_{\mathrm{top}} \frac{\lambda A_{\mathrm{top}}}{D} + \mathrm{Nu}_{\mathrm{side}} \frac{\lambda A_{\mathrm{side}}}{L} \right) (T - T_\infty) \tag{2.34}$$

As can be seen, the total heat flow is a function of the water vessel wall temperature T. In figure 2.5, the total heat flow from the water vessel is shown as a function of the temperature of the

wall of the water vessel, assuming a constant temperature of the surrounding air. With all other parameters known, equation (2.34) can be solved using an iterative process, evaluating the material properties at a temperature referred to as the *film temperature*, which is the average of the water vessel wall temperature and the ambient temperature $\frac{T+T_\infty}{2}$.

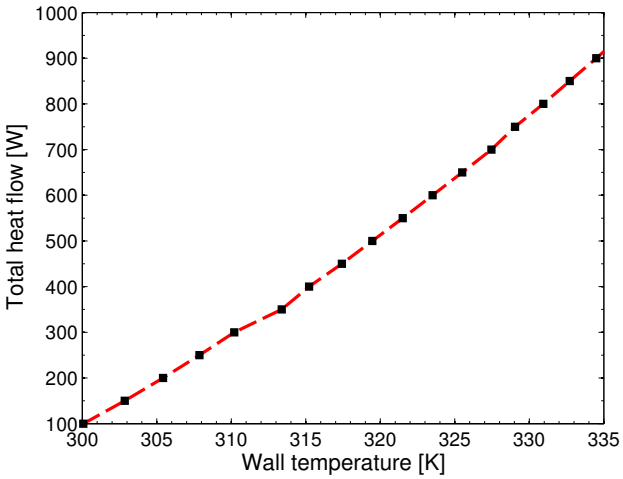

Figure 2.5: The higher the temperature at the wall of the water container is, the larger the amount of heat flow from the reactor to the surroundings. This makes sense, because the temperature difference is the driving force for heat transfer. A small kink can be seen between 310 and 315 K. For higher temperatures the Rayleigh number is larger than $2{\cdot}10^7$, causing a change in the relation between the Nusselt and Rayleigh number (see (2.33)). The air temperature far away from the reactor is set at 298K.

3

COMPUTATIONAL CODES

3.1. SCALE XSDRNPM

The multiplication factors for different fuel solutions as described in chapter 2.1 are calculated using the program SCALE. This program performs calculations regarding reactor physics and criticality and is developed by Oak Ridge National Laboratory (ORNL). SCALE XSDRNPM is a one-dimensional code for neutron transport, and is used to calculate the multiplication factor k_{eff} for a specified geometry. The atomic composition of the material is entered by defining the nuclides present together with their number densities. For the calculations in chapter 2.1, the program uses the ENDF/B-V cross section database, and solves the Boltzmann equation (3.1) for 238 energy groups. Using a S_{16} calculation with 30 inner and 20 outer iterations (for swift calculation and enough accuracy), the k_{eff} and flux are calculated.

$$\vec{\Omega} \cdot \nabla \Psi \left(\vec{r}, E, \vec{\Omega}\right) + \Sigma_t \left(\vec{r}, E\right) \Psi \left(\vec{r}, E, \vec{\Omega}\right) = S \left(\vec{r}, E, \vec{\Omega}\right) \tag{3.1}$$

This time-independent version of the Boltzmann equation (the k_{eff}, which arises in the fission source term, will not change in time for a fixed geometry and composition) consists of four terms: the leakage/flow term $\vec{\Omega} \cdot \nabla \Psi$, the interaction term $\Sigma_t \Psi$ and two source terms (denoted by S). The fission source term can be written as

$$\frac{1}{k} \frac{1}{4\pi} \chi \left(\vec{r}, E\right) \int_0^{4\pi} \mathrm{d}\vec{\Omega}' \int_0^{\infty} \nu \left(\vec{r}, E'\right) \Sigma_f \left(\vec{r}, E'\right) \Psi \left(\vec{r}, E', \vec{\Omega}'\right) \mathrm{d}E'$$

with ν the average number of neutrons produced per fission (approximately 2.45), Σ_f the macroscopic fission cross section, χ the fraction of the produced neutrons per unit energy and k the effective multiplication factor.

The scatter source term

$$\int_0^{4\pi} \mathrm{d}\Omega' \int_0^{\infty} \Sigma_s \left(\vec{r}, E' \rightarrow E, \vec{\Omega}' \rightarrow \vec{\Omega}\right) \Psi \left(\vec{r}, E', \vec{\Omega}'\right)$$

contains the macroscopic scattering cross section, specified for scattering from a certain energy and direction $\left(E', \vec{\Omega}'\right)$ to $\left(E, \vec{\Omega}\right)$.

3.2. HEAT

One of the characteristic aspects of the designs of the AHRs discussed in chapter 2.5 is that the fuel is continuously flowing through the reactor. However, the flow of fuel is not the only process

influencing the flow pattern. To get an accurate image of what is actually happening inside the reactor regarding flow, the Navier-Stokes equation (3.2) has to be solved and in addition, solutions for the concentration distribution (3.3) and temperature distribution (3.4) have to be calculated.

$$\rho\frac{\partial\vec{v}}{\partial t}+\rho\left(\vec{v}\cdot\nabla\right)\vec{v}=\mu\nabla\cdot\left[\left(\nabla\vec{v}+\nabla\vec{v}^{T}\right)-\frac{2}{3}\nabla\cdot\vec{v}I\right]-\nabla p+\vec{f} \tag{3.2}$$

$$\frac{\partial c_i}{\partial t}+\vec{v}\cdot\nabla c_i=\nabla\cdot(\mathscr{D}\nabla c_i)+\gamma_i S-\frac{c_i}{\tau_i} \tag{3.3}$$

$$\rho C_p\left(\frac{\partial T}{\partial t}+\vec{v}\cdot\nabla T\right)=\nabla\cdot(\lambda\nabla T)+p \tag{3.4}$$

Table 3.1 shows the physical meaning of the symbols used in equations (3.2), (3.3) and (3.4)

Table 3.1: Physical meaning of symbols used in the aforementioned equations.

Symbol	**Meaning**	**Unit**
γ_i	Relative production yield of particle i	-
λ	Thermal conductivity	$\mathrm{Wm^{-1}K^{-1}}$
μ	Dynamic viscosity	$\mathrm{Nsm^{-2}}$
ρ	Density	$\mathrm{kg\,m^{-3}}$
τ_i	Mean lifetime of particle i	s
C_p	Specific heat	$\mathrm{Jkg^{-1}K^{-1}}$
c_i	Concentration of particle i	$\mathrm{m^{-3}}$
$\vec{f}$	Force per unit volume	$\mathrm{Nm^{-3}}$
p eq. (3.2)	Pressure	$\mathrm{Nm^{-2}}$
p eq. (3.4)	Power per unit volume	$\mathrm{Wm^{-3}}$
S	Production rate	$\mathrm{m^{-3}s^{-1}}$
T	Temperature	K
$\vec{v}$	Velocity vector	$\mathrm{ms^{-1}}$
$\mathscr{D}$	Diffusion coefficient	$\mathrm{m^2s^{-1}}$

Although these equations look relatively easy in their continuous forms, they have to be rewritten in a discrete form in order to implement them in a program using a discrete grid. A detailed overview of the steps involved in the discretization process can be found in appendix A.

The program used to calculate the solutions is a computational fluid dynamics (CFD) code called HEAT, written by dr. ir. Lathouwers. It uses a finite volume method to solve the aforementioned discrete equations and compute the fields of the relevant quantities. The cells are defined by a staggered grid as shown in figure 3.1. As can be seen in figure 3.1, the scalar cells (the cells where the scalar quantities such as pressure, temperature and concentration are calculated) and momentum cells (where the horizontal and vertical speeds are calculated) are defined in such a way that the momenta at the boundary of each scalar cell are known. The spherical symmetry of the system infers that no quantity has an angular dependence. This is an approximation; in reality small perturbations will disrupt the spherical symmetry.

The choice for the size of the grid is of importance, as on one hand a small grid will lead to a more detailed solution, while on the other hand a larger number of cells will increase computational effort and therefore time needed to complete the calculations. This trade-off implicates a grid has to be chosen based on one's priorities. For the calculations, a grid of 25.000 - 30.000 cells is used.

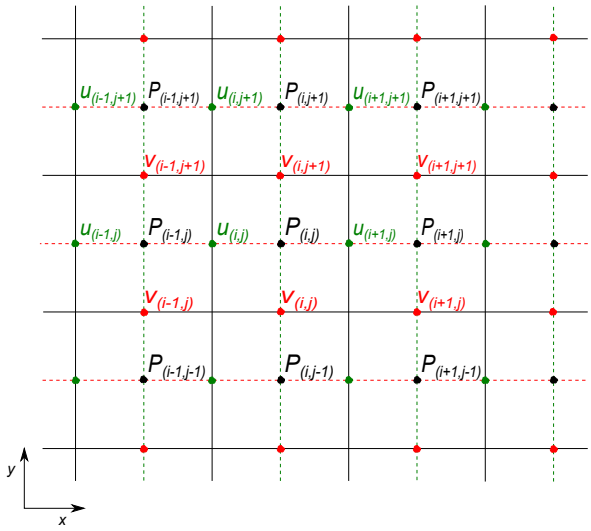

Figure 3.1: A part of the grid surrounding the scalar cell *(i,j)*. The cells bounded by the green dashed lines and horizontal solid black lines are the horizontal (u) momentum cells, the cells confined by the vertical solid borders and the red lines are the vertical (v) momentum cells and the cells denoted by P are the scalar cells.

As already mentioned, some assumptions are made in the calculations. First, although HEAT has been designed to deal with turbulent flows, turbulent effects are neglected during calculations as the speeds in the reactor are relatively low, so that the flow is in the laminar regime. Second, the buoyancy effects on the vertical momentum are approximated using the Boussinesq theorem (see section 2.3) to describe density differences

$$\rho = \left(1 - \beta_0 \Delta T\right) \rho_0 \tag{3.5}$$

This approximation is valid if $\beta \Delta T << 1$. The temperature differences and the thermal expansion factor in the reactor are of the order 10^1 and 10^{-4} (see figure 2.3) respectively, so this criterium is fulfilled. A third approximation is that all formed gas bubbles move at the same speed as the fuel, and therefore ca not escape from the fuel into the air above. The justification for this assumption stems from the notion that the bubbles have a very small size and low speed relative to the fuel, explained in section 2.2. Finally, the fuel level is set at a fixed height ignoring ripples, which is a valid approximation when the speeds are sufficiently low so that no slushing will occur.

For linking the pressure and velocity, a pressure-correction method called SIMPLE (Semi-Implicit Method for Pressure-Linked Equations) is used. A detailed explanation of this algorithm can be found in the book '*An introduction to computational fluid dynamics*' [53]; globally it is an iterative solving mechanism which updates pressure and speed turn by turn, until convergence is reached.

During the calculations on the steady state behavior of the reactor, another (outer) loop is created which, for a given power, updates all characteristics (momenta and pressure in the SIMPLE routine and temperature) until a predefined level of temperature convergence is reached. Both loops are shown schematically in figure 3.2.

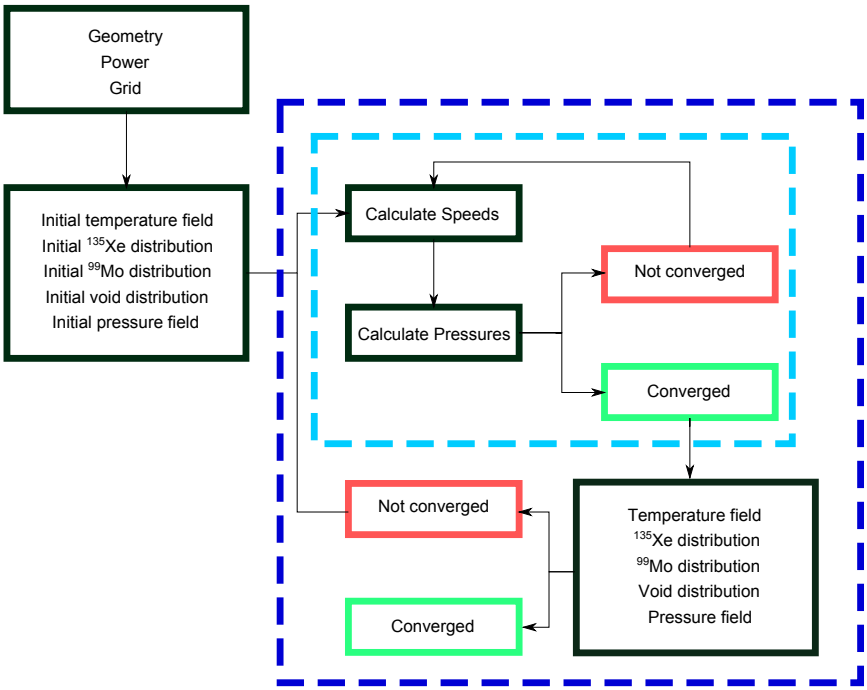

Figure 3.2: A schematic overview of the flowchart of HEAT. The geometry, power and grid are used to produce an initial guess for the fields that are going to be calculated. In a calculation of the steady state these are put into a loop which recalculates the fields until a convergence criterium is fulfilled. Inside this loop, another loop (the SIMPLE routine) is placed, which updates the momenta and pressure iteratively.

3.3. SERPENT

As HEAT calculates only the flow and temperature profile for a given power distribution, another code is needed to calculate the power distribution for a given temperature distribution. The neutronics part of the process is calculated by a code called Serpent, which is a continuous-energy Monte Carlo reactor physics code [54]. Development started in 2004 at the VTT Technical Research Centre of Finland under supervision of Jaakko Leppänen, and although the code is still being improved, it is already useful for finding a detailed power distribution. Based on the irradiation history and a list of depleted materials together with a decay and a fission yield library, also the fuel burnup can be calculated. For an increase in computational speed, the possibility of parallel processing is included, which is particularly useful because the Serpent calculations contribute a large part to the total calculation time.

In the evaluation, neutrons are simulated one by one travelling through the geometry defined by the input file. These neutrons interact with the materials, using the ENDF/B-VII database for evaluating cross sections. On the basis of these interactions, a power distribution is created, which contains information about the fission events and therefore the production of isotopes. Of course the simulation of more neutrons leads to a higher statistical accuracy, but again there is the important trade-off between accuracy and calculation time.

3.4. COUPLING BETWEEN SERPENT AND HEAT

In order to calculate a steady state solution, HEAT and Serpent are coupled, because the neutronics (calculated with Serpent) are dependent on results from the fluid dynamics (calculated with HEAT) and vice versa. The coupling code transfers the calculated power distribution from Serpent to HEAT, and details on place-dependent fuel composition and temperature the other way around.

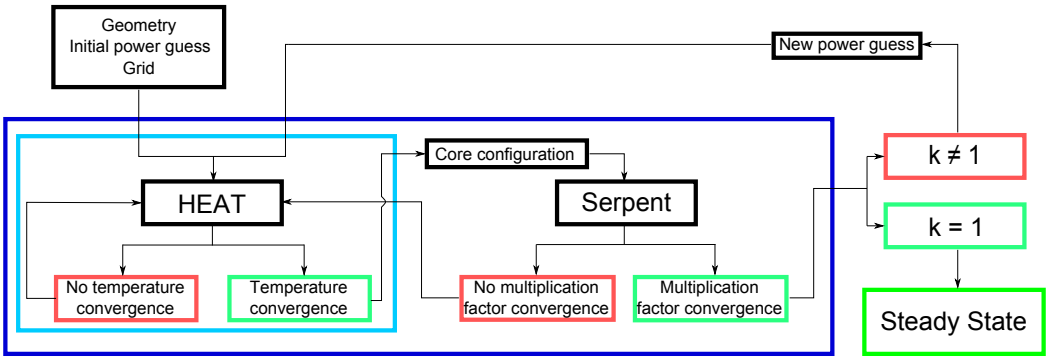

Figure 3.3: A schematic review of the flowchart for calculation of the steady state power. The first loop is the HEAT loop as shown in figure 3.2. Subsequently, Serpent calculates the multiplication factor using the fields calculated in HEAT, in the scheme included as 'core configuration'. If the outer loop has converged and the multiplication factor is not equal to 1, a new power guess is made and the next outer loop iteration starts.

As the number of cells used in Serpent (800) is significantly smaller than the amount of cells in HEAT (several thousands) due to calculation time issues, each Serpent cell corresponds to multiple (parts of) HEAT cells. When data is transferred from HEAT to Serpent, the values (particle concentrations, temperature) stored in the Serpent cells are the averages of the values in the corresponding HEAT cells. If data is transferred in the opposite way, the values calculated by Serpent (power density, isotope production) in a single Serpent cell are stored in multiple HEAT cells.

In figure 3.3, the schematic program structure for finding the steady state power is shown. Every calculation of the steady state power starts with a specification of the geometry accompanied by an initial power density guess. In a number of iterations, HEAT calculates the flow profile, temperature distributions and fuel compositions; the loop is stopped when the temperature difference between two subsequent iterations is smaller than a predefined value. If the temperature has converged, the fuel specifications of each HEAT cell are moulded into the correct input form for Serpent. If the multiplication factor calculated by Serpent is similar to the one calculated in a previous iteration (within a predefined radius of convergence), the power is changed (if $k_{\text{eff}} > (1+\epsilon)$ or $k_{\text{eff}} < (1-\epsilon)$, with ϵ defining the accuracy), or the loop is ended (if $(1-\epsilon) \leq k_{\text{eff}} \leq (1+\epsilon)$) and the steady state power is found.

3.5. POINT KINETICS

The transient behavior of the reactor is very important for the safety evaluation. As long as the reactor operates at the steady state power and no events disrupting any parameter occur, the time-dependent evolution is rather predictable and slow. In case of an event, either wanted (caused by operating personnel) or unwanted (system malfunction), various parameters are prone to change. Therefore, an assessment of various events and their consequences has to be made in order to identify and subsequently eliminate or reduce certain risks.

The technique described before could be used, doing a Monte Carlo calculation for every time step, but as each individual Monte Carlo calculation takes several hours to complete, this technique is not favorable for time-dependent calculations, in which several tens or hundreds of time steps are needed. Therefore another method, *point kinetics*, is used to gain insight into the time evolution of the system properties.

The point reactor kinetics method makes use of a time-independent, spatial flux shape ψ, which scales with an amplitude factor that is variable in time *n(t)*. This assumption infers that point kinetics can be used as approximation as long as the flux shape change induced by perturbation of a certain parameter is not significant. An example of a case in which the spatial flux shape changes significantly is for example the instantaneous removal of all fuel from the reactor core.

The point kinetics model uses seven different equations (of which 6 are quasi-identical)

$$\frac{\mathrm{d}n}{\mathrm{d}t} = \left(\frac{\rho(t)-\beta}{\Lambda}\right) n(t) + \Sigma_i \lambda_i C_i(t) \tag{3.6a}$$

$$\begin{aligned} \frac{\mathrm{d}C_1}{\mathrm{d}t} &= \frac{\beta_1}{\Lambda} n(t) - \lambda_1 C_1(t) \\ \vdots &= \vdots \\ \frac{\mathrm{d}C_6}{\mathrm{d}t} &= \frac{\beta_6}{\Lambda} n(t) - \lambda_6 C_6(t) \end{aligned} \tag{3.6b}$$

where n is the previously mentioned amplitude factor, t the time, ρ the reactivity, β the delayed neutron fraction (β_i is the delayed neutron fraction from the precursor group i), Λ the neutron generation time, λ_i the precursor decay constant and C_i the precursor concentration, both for the specific group specified by i.

Implementing these equations, a prediction of the time evolution can be made, provided that the reactivity changes in time are known. An overview of reactivity effects resulting from a variety of events is given in chapter 5.

4

STEADY STATE CALCULATIONS

4.1. INITIAL DESIGN

As a starting point for the development of the AHR, the exact same geometry as described by Mark Huisman (*'Bulkheads'*) [29] is taken. The most significant difference in design is the fuel, which is changed from a uranyl nitrate solution to a uranyl sulfate solution, with a uranium concentration of 251 gL^{-1}, flowing into the reactor at a rate of 0.4 kgs^{-1}. Some additional changes were made in the code system, to better reflect actual physics; a method to calculate the void fraction due to the production of radiolytic gas has been incorporated in HEAT. Furthermore, a scheme to describe expansion of the fuel was added. This scheme corrects the local fuel composition for both temperature and void effects. The temperature expansion coefficient of water at 323 K was used in the calculations. Fuel flows in at a temperature of 303 K, and the temperature at the reactor vessel wall is also fixed at 303 K.

Some characteristics of this reactor operating in steady state are visualized in figures 4.1 and 4.2. The thermal power of this reactor in a steady state situation is approximately 18.5 kW, with a higher power density at the center of the reactor than at the outer regions. The power density (figure 4.1a) at the center of each inflow annulus is higher than that at the sides of the annulus. This is a result of the higher temperature and void fraction near the structural material, as can be seen in figures 4.1b and 4.2a. Because the fuel speed decreases near the structural material (see figure 4.2b), the fuel will heat up more and the void fraction will increase. This will lead to a lower concentration of uranium and therefore a lower power density. The temperature of the fuel stays well below the boiling point, the maximum temperature of 321.3 K is found in the outflow pipe at the center.

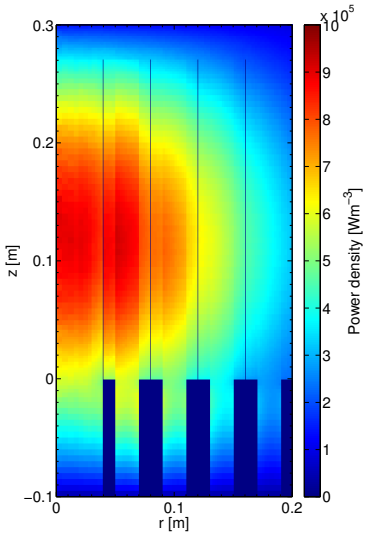

(a) The power density has roughly a spherical shape. In the middle of each inflow annulus the power is somewhat higher than at the edges, which is most evident in the most central inflow annulus

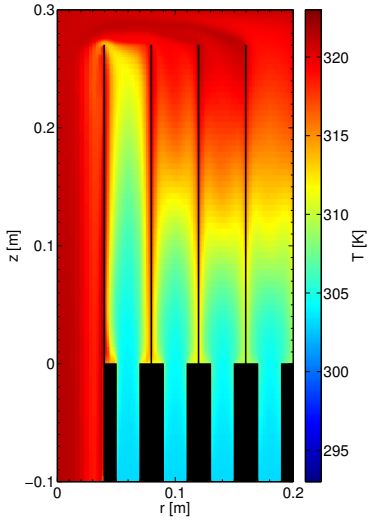

(b) The temperature profile in the reactor. Temperature differences in the inflow annuli arise for various reasons: the difference in power density, difference in heat transfer to surrounding volume, and difference in flow speed.

Figure 4.1

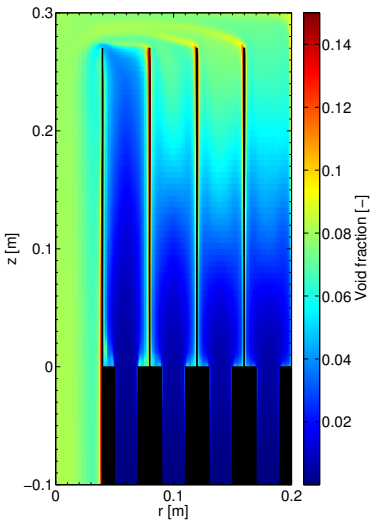

(a) The void fraction near the guiding walls tends to be higher than at other places because of the low speed near these walls.

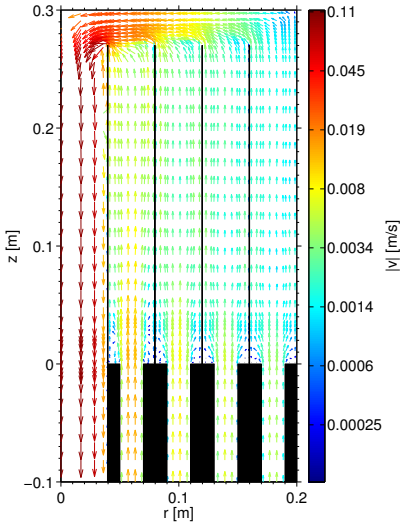

(b) Looking closely at the flow pattern it can be seen that the flow speed is lower at the edges of the annulus.

Figure 4.2

4.2. ADJUSTING INFLOW

Because of the cylindrical core design, the inflow area of each annulus is dependent on the distance from the center of the reactor vessel. In the initial design the mass inflow rates for all annuli were all set at 25% of the total mass inflow rate, which led to higher fuel speeds in the center of the reactor. Although the power density is higher in this part of the reactor, the fuel is less irradiated because of

the high flow rate. The inflow ratios were changed to investigate the effect on the temperature, total power and void fraction, while keeping the total mass inflow rate at 0.4 kgs^{-1}.

If the ratio between mass inflow rates is taken as the ratio of the areas of the inlet annuli perpendicular to the flow (3:5:7:9), the fuel in the centre inflow annulus will heat up more, as the power density is higher at the core of the reactor. To correct for this effect, the ratio (7:9:11:13) is chosen.

At a slightly lower power level (18.2 kW compared to 18.5 kW), the average temperature decreases with 0.7 degrees whereas the maximum temperature increases by 1.6 degrees. The average void fraction decreases with approximately 8% to 0.034.

The result of a higher temperature in the center and a lower temperature at the edge of the reactor vessel means less energy can be transferred to the environment. This will limit the total power at which the reactor operates in steady state.

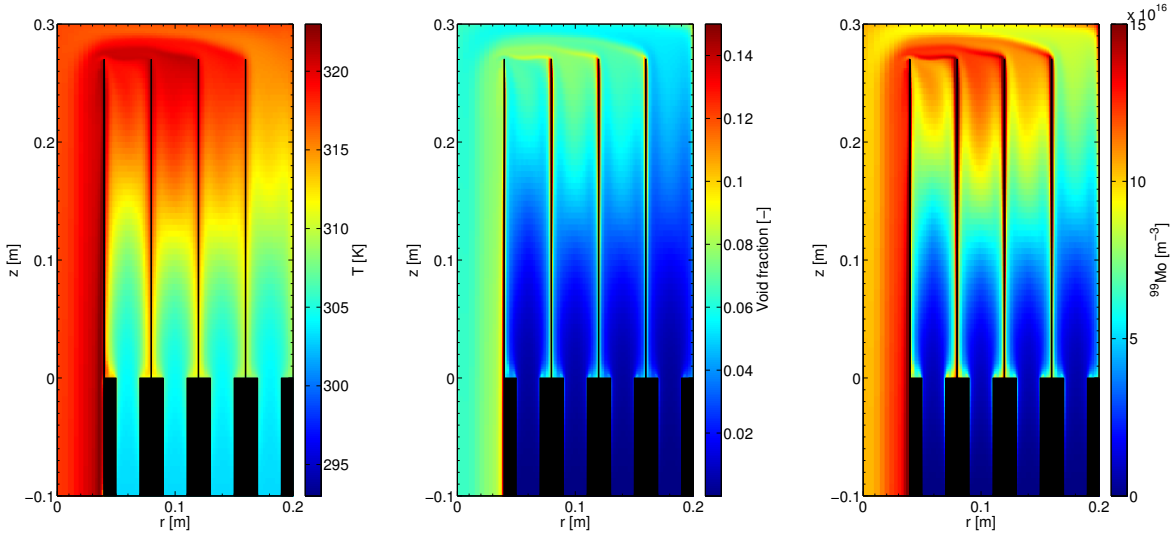

(a) Temperature (b) Void fraction (c) Concentration of ^{99}Mo

Figure 4.3: The inflow ratios have been changed from 1:1:1:1 to 7:9:11:13. As a result the temperature in the most central inflow annulus is increased. Also the distributions of void and ^{99}Mo have changed in a similar way: an increase in the center annuli, a decrease in the outer ones.

4.3. 12 INLETS

In the initial design the flow speed in the center of the annuli is higher than at the sides, which leads to an increased temperature and void fraction near the edges of the annuli. Furthermore, the abrupt widening at the inflow creates vortices in the bottom corners of the annuli (see figure 4.4a), which also cause a higher local void fraction and temperature. A local high void fraction should be avoided, because it can lead to the formation of larger bubbles which can, for example, cause slushing.

Both the previously mentioned effects can be prevented by splitting up each inlet into multiple inlets. By placing two inlets at the side and one at the center of each annulus, the flow speed near the structural material is increased and the vortices have decreased in size, see figure 4.4b. In figure 4.5 the vertical speed is shown as a function of the radius. The speed at the edge of each annulus is still zero as it should be (because of the no-slip boundary condition), but the gradient is much steeper.

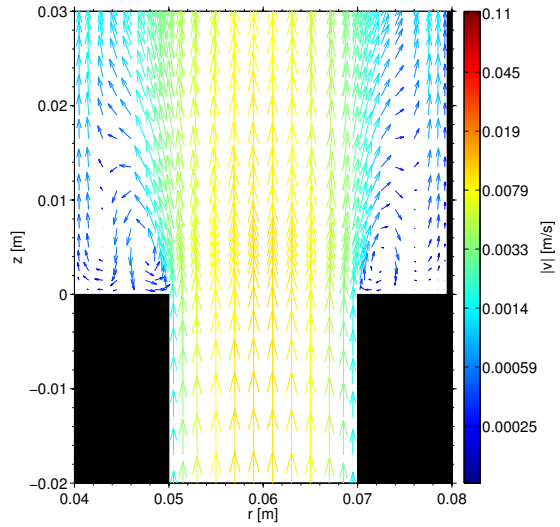

(a) In the initial design 2 vortices appear near the entrance, both approximately 1 centimeter in diameter.

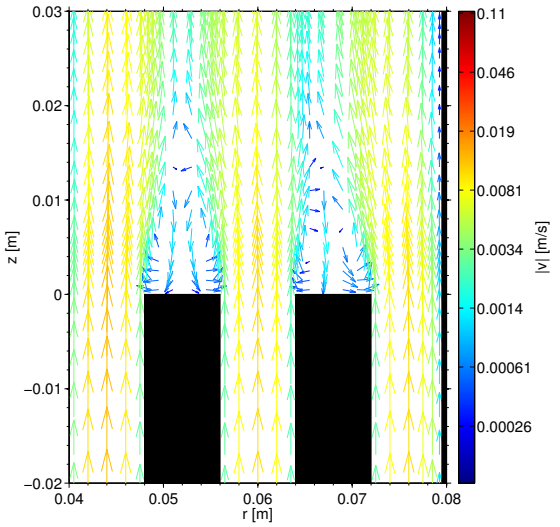

(b) In the design with 12 inlets the vortices are slightly smaller, and the speed near the edges of the annulus is increased

Figure 4.4

The profiles shown in figure 4.6 are found in steady state operation of the reactor. The accumulated fraction of the fuel flowing through the first 3 inlets is slightly less than 0.25. In the other 9 inlets the remainder is evenly distributed, resulting in a slightly higher speed as the center of the reactor vessel is approached. This leads to a reasonably flat temperature distribution, as shown in figure 4.6a. At a total power of 19.7 kW, the average temperature is 311.4 K. The maximum void fraction has decreased with respect to the previous designs, even though the power is higher. ^{99}Mo flows out at a rate of $3.87{\cdot}10^{13}$ atoms per second. If every day a batch of ^{99}Mo is transported from the facility the total production is 359 6-day Ci per week, assuming a 100% extraction yield.

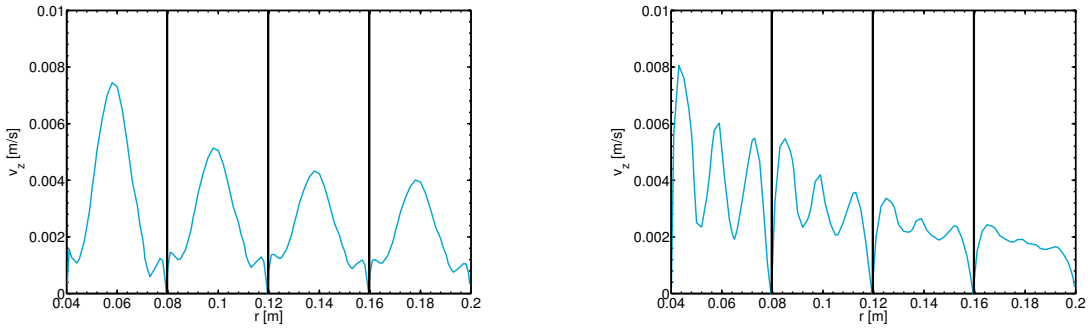

(a) (b)

Figure 4.5: In the left diagram the speed distribution is shown for the initial design, the right diagram shows the vertical speed for the design with 12 inlets. In both cases the speed at the (guiding) walls is zero, but the gradient is much steeper for the design with 12 inlets. The vertical speeds are taken at 2.8 cm above the entry level.

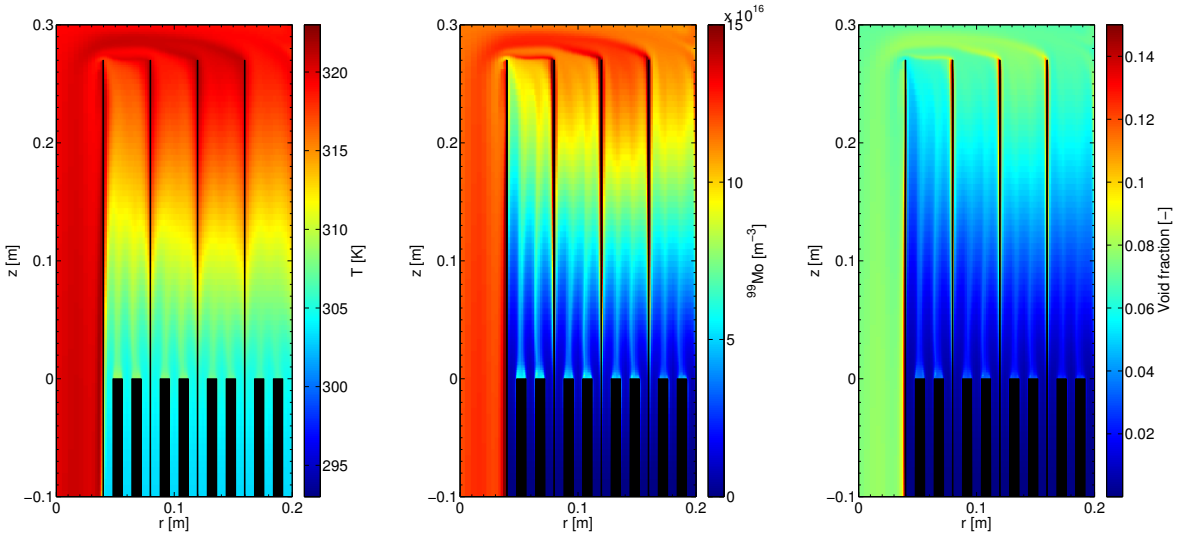

(a) (b) (c)

Figure 4.6: The temperature distribution (left) is more homogeneous thanks to the slight adjustment of inflow ratios and the higher speed at the edges of the annuli, which prevent the fuel at the edge of the annulus from heating up more than the fuel in the center. Also in the concentration ^{99}Mo (center) and distribution of the void (right) the effect is visible: less buildup of fission products and a lower void fraction near the structural material are the result of the increase in the number of inlets.

4.4. IMPROVING THE MODEL

Up to this point the expansion of the fuel due to temperature differences is calculated using a thermal expansion coefficient for pure water, which is not temperature-dependent. As described in chapter 2.3, the actual thermal expansion coefficient for a uranyl sulfate solution differs from the used value by a order of magnitude. To improve the model the temperature-dependent values have been incorporated. Because the new values of the expansion coefficient are smaller than the previous ones, the local fuel densities have increased.

As a result, the steady state reactor power increases to 50.5 kW, which also leads to an increase in temperature. While the average temperature rises 12 degrees to 323.2 K, the maximum temperature rises to 349.1 K. The average void fraction increases to almost 0.1, the maximum void fraction to more than 0.5. At this point, the physical correctness of the model can be doubted, because the assumption is made that bubbles do not coalesce. For local void fractions of 0.5, the chance of coalescence is larger and the bigger bubbles will not move at the same speed as the fuel. Therefore, the reactor power will be lowered.

The increase in steady state power leads to an increase of the outflow rate of ^{99}Mo to $9.96 \cdot 10^{13}$ atoms per second, corresponding to a weekly production of 925 6-day Ci (based on daily transport from the facility).

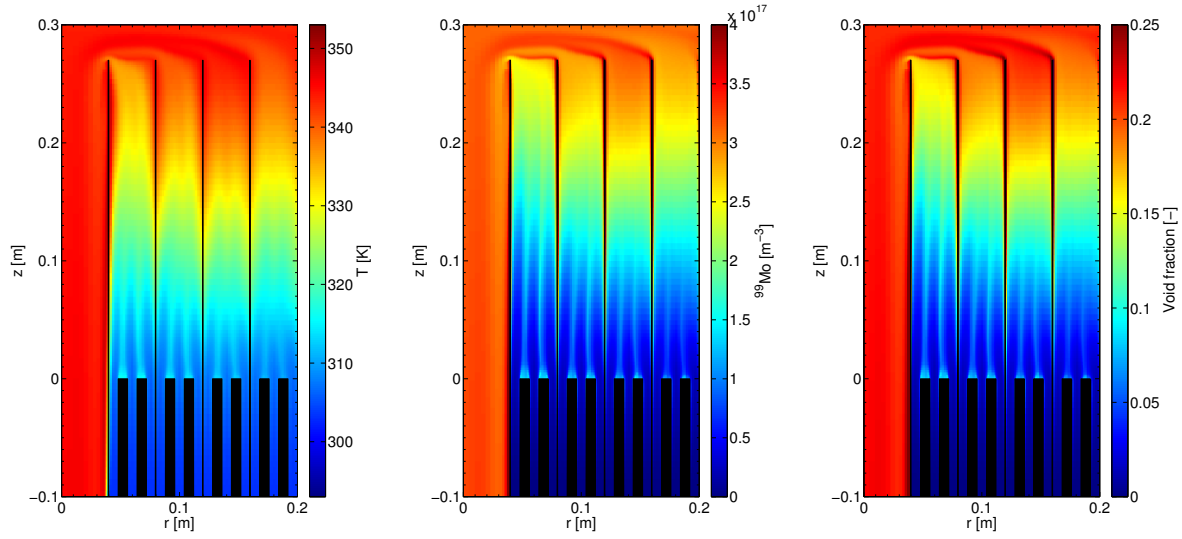

Figure 4.7: Because the new expansion coefficient is much smaller than the one previously used, the total amount of uranium in the core has increased, causing an increase in the total power by a factor of approximately 2.5. This increase leads to higher temperatures (a), but the maximum temperature stays well below the boiling point. Also the concentration of ^{99}Mo (b) and the void fraction (c) increase with a factor of approximately 2.5, leading to high void fractions (over 20%).

4.5. LOWERING THE CONCENTRATION

Because the production rate of ^{99}Mo using a 251 gL^{-1} uranium solution exceeds 200 6-day Ci per week and the power level causes large void fractions, the power will be lowered. An easy way to do this is to lower the uranium concentration. Using a solution with 225 gL^{-1} uranium in the form of a uranyl sulfate solution rather than the original solution leads to a steady state power of 13.6 kW. The maximum void fraction has decreased to 0.18, the average temperature to 308.4 K and the maximum temperature to 316.5 K.

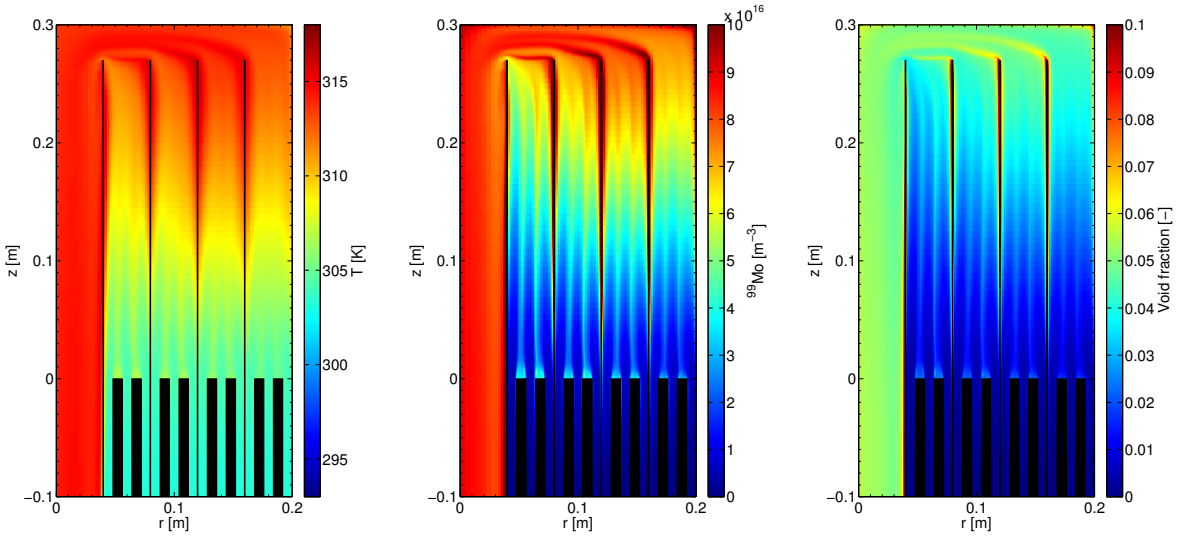

Figure 4.8: By lowering the concentration of uranium, the power of the reactor decreases drastically. As a result, the fuel heats up significantly less, leading to a maximum temperature of only 316.5 K. Also the molybdenum concentration and the void fraction decrease.

4.6. IMPROVING THE CODE

Until now, all calculations have been performed with a fixed temperature at the boundary of the fuel region, which of course does not reflect the actual situation. In a few steps the code has been extended to include temperature gradients, pressure differences and buoyancy-driven flows in the water vessel. As a first step, the temperature at the inside of the water vessel wall is set to a fixed value. This enables temperature differences (figure 4.9b) in both air and water regions, leading to buoyancy-driven flows. However, the temperature at the boundary of the water vessel is not the boundary value. In chapter 2.6, a correlation between the heat flow and both the water vessel wall temperature and the surrounding air temperature is shown. Adding an iterative loop, this condition can be used to accurately determine the temperature distribution in the entire reactor, shown in figure 4.9c. The buoyancy-driven flows and the flow pattern of the fuel are shown in figure 4.11.

Because the temperature at the outer boundary of the system is increased with respect to previous calculations, the heat transfer has deteriorated. As a result, the power is slightly lowered (13.2 kW), leading to a maximum fuel temperature of 316.1 K; well below the boiling temperature. The average ^{99}Mo concentration at the outflow is $9.44 \cdot 10^{16}$ m^{-3}, which equals a production of 266 6-day Ci per week, assuming a 100% extraction yield and daily transport from the facility.

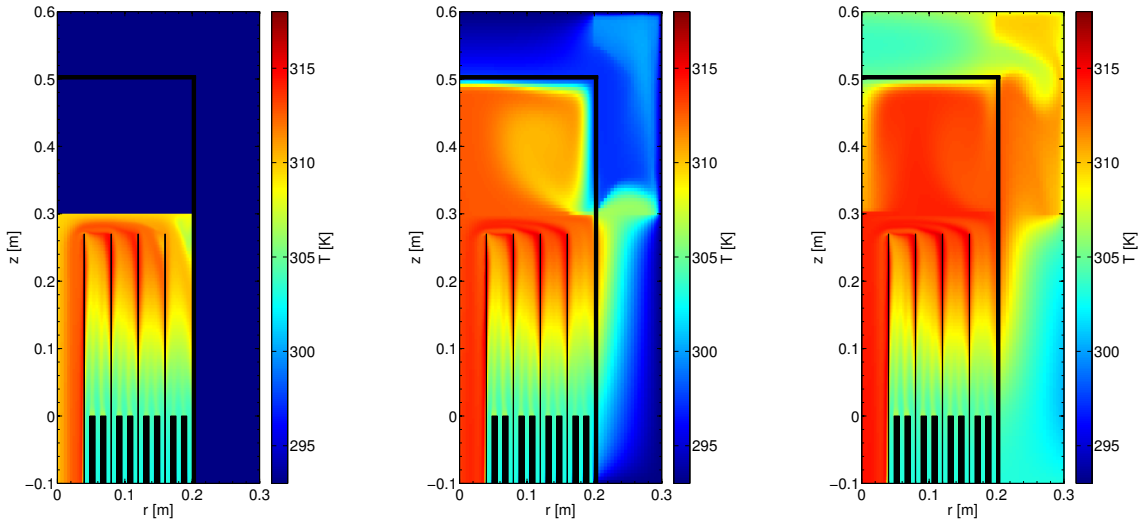

Figure 4.9: The temperature of the water in the water vessel has been fixed at 293 K. Because the water temperature does not rise, the temperature gradient will be overestimated, which results in a larger heat transfer than in reality (a). In another case, the temperature of the water vessel wall has been fixed at 293 K. The air above the fuel can only conduct heat, so the heat transfer is underestimated (b). Finally, both the water and air region can flow as a result of density differences, leading to a more realistic heat transfer. The heat transfer from the wall to the environment is a function of the wall temperature and the ambient temperature, which is set at 293 K (c).

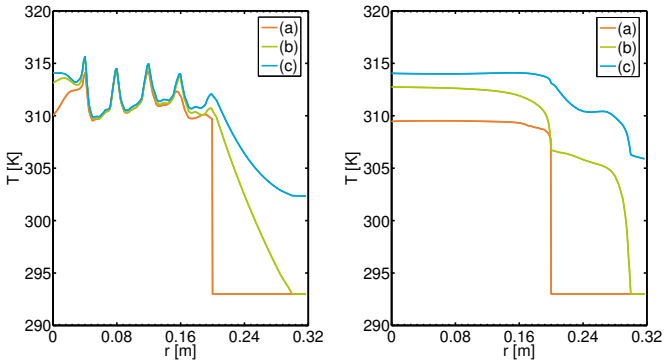

Figure 4.10: The radial temperature distribution in the left figure is taken at $z = 0.2$ m, in the right figure at z=0.3m. Cases (a), (b) and (c) correspond to figures 4.9a, 4.9b and 4.9c respectively. In case (a) the most heat can be transferred, which can be seen from the temperature difference at the side of the reactor ($r = 0.2$ m) and at the top, where the temperature difference is largest in case (a).

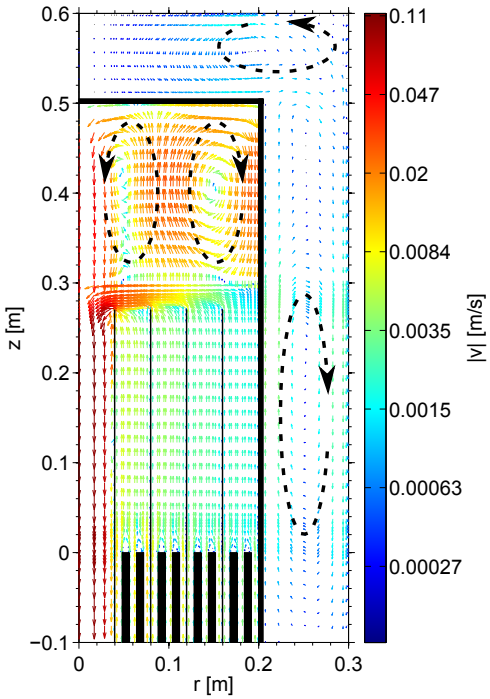

Figure 4.11: The flow pattern of the air, water and fuel in one figure. The flow of the water and air is caused by buoyancy effects; the dashed ellipses indicate the circulation of the fluids.

5

REACTIVITY ANALYSIS

For investigating the time-dependent behavior of the reactor, a database of reactivity effects is assembled. Seven parameters are looked into: uranium concentration, ^{135}Xe concentration, void fraction, fuel temperature, fuel level (an increase in the height of the fuel in the reactor core), water level (a decrease of the level of the water in the water vessel) and a fuel leak (a leak of fuel from the reactor inflow pipe to the water in the water vessel). The time-dependent reactivity value used in transient calculations will be a sum of these individual reactivity effects.

Serpent is used to calculate the effective multiplication factor for every perturbation of the steady state. All parameters are perturbed multiple times individually, so that a database of multiplication factors corresponding to perturbed situations is available. Subsequently, the reactivity $\rho = \frac{k-1}{k}$ is calculated and a function is fitted to be able to interpolate the data, which is necessary for the point kinetics calculations.

In some transient calculations, the reactivity value used in the calculations is a sum of the individual reactivity effects, which is only accurate if no correlation between effects exists. To see if our data fulfills this requirement, Serpent is used once again to calculate the reactivity in a situation where multiple characteristics are changed simultaneously.

5.1. URANIUM CONCENTRATION

If the uranium concentration in the fuel increases, the macroscopic absorbtion cross section (especially fission) of the fuel increases and the non-leakage probability of a neutron increases, which means the multiplication factor increases. The relation between the uranium concentration and the reactivity is shown in figure 5.1. A second order correlation is used to fit the datapoints, which has uncertainties of approximately 8 pcm.

The reactivity as function of the uranium concentration is represented by

$$\rho_U = -4.3417 \cdot 10^{-6} c_U^2 + 2.9077 \cdot 10^{-3} c_U - 4.3443 \cdot 10^{-1} \tag{5.1}$$

which corresponds to a reactivity effect of 95.4 pcm $(\mathrm{gL}^{-1})^{-1}$ at a uranium concentration of 225 gL^{-1}. Huisman has found a reactivity of 66.0 pcm $(\mathrm{gL}^{-1})^{-1}$ for his uranyl nitrate fueled design at a uranium concentration of 248 gL^{-1}. A similar value (75.4 pcm $(\mathrm{gL}^{-1})^{-1}$) is found for the current design with the uranium concentration set at 248 gL^{-1}.

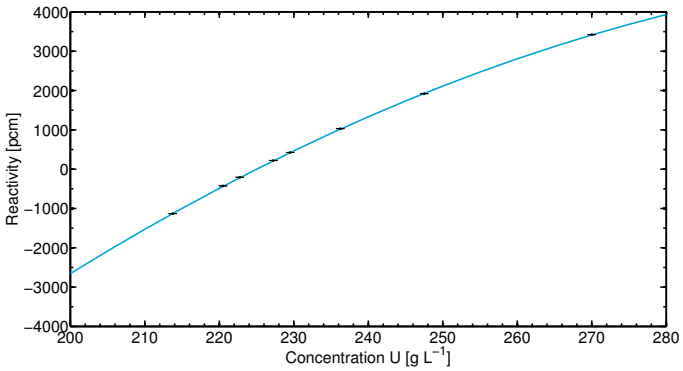

Figure 5.1: The second order fit corresponds well to the data. All data points have error bars, but because the uncertainty is small with respect to the reactivity changes, these are not visible.

5.2. XENON CONCENTRATION

^{135}Xe is a known for its large neutron absorbtion cross section, so the evolution of the xenon concentration plays a role in the transient behavior of the reactor. To analyse the effect of the xenon concentration on the reactivity, the average concentration of xenon is increased and the reactivities are plotted. For a hundredfold increase of the xenon concentration the reactivity is -17 pcm, which is of the same order of magnitude as the value found by Huisman [29].

The small effect on the reactivity can be explained by looking into the ratio of the number of neutrons absorbed in the fuel material to the total number of neutrons absorbed (called the thermal utilization factor, $f = \frac{\Sigma_a^F}{\Sigma_a}$, with Σ_a the macroscopic absorbtion cross section and superscript F denoting 'fuel'). If the macroscopic absorbtion cross section of ^{135}Xe is only a small fraction of the total macroscopic absorbtion cross section, a hundred-fold increase in the concentration will cause a small decrease of the thermal utilization factor and therefore a small decrease of the multiplication factor. A second order fit to the data is shown in figure 5.2.

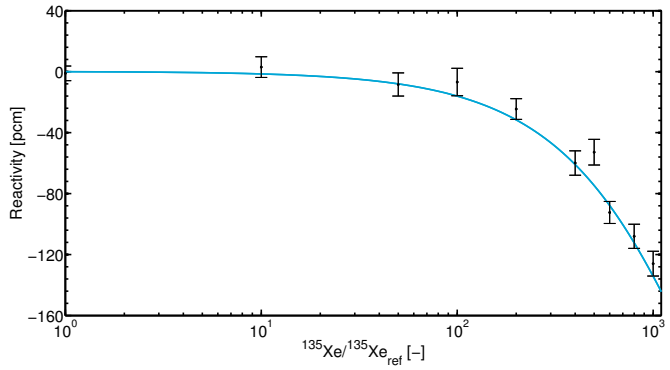

Figure 5.2: The reactivity effect of the ^{135}Xe concentration divided by the concentration during steady state operation. A second order fit is made, and a logarithmic scale is used to show the reactivity at higher concentrations.

5.3. VOID FRACTION

In steady state, the reactor operates with a void fraction of 0.0269. The larger this void fraction becomes, the less volume is actually occupied by fuel. Therefore, a larger void fraction results in a lower multiplication factor because a larger fraction of neutrons will leak from the reactor. Since the void fraction is proportional to the reactor power, an increase in power will lead to an increase of the void fraction, which will lower the reactivity (see figure 5.3). This negative feedback has a limiting effect on the reactor power.

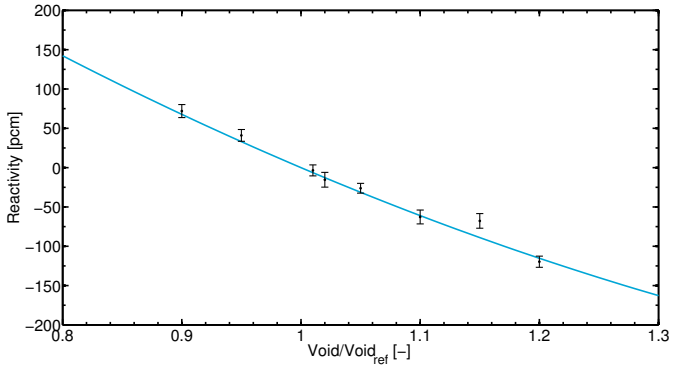

Figure 5.3: For the reactivity effect of the void concentration, data for small perturbations is fitted. Whereas for the xenon concentration it was reasonable to look at a hundred-fold increase, it is not for the void fraction. For large void fractions, the model will not represent reality as the model assumes all void is present in the form of small bubbles.

5.4. TEMPERATURE

The temperature effect on the reactivity is a combined effect of Doppler broadening and the expansion of the fuel (for an increase in temperature). Using the Boussinesq approximation as presented in chapter 2.3, an estimate of the expansion of the fuel is made, while the Doppler broadening is realised by using cross sections at a different temperature. If a second order fit is made (see figure 5.4) and the derivative is taken at a temperature of 310 K, a reactivity coefficient of -10 pcm K^{-1} is found, which is of the same order of magnitude as the value found by Cooling et al. for their AHR, -19.2 pcm K^{-1} [46]. The reactivity effect is 3 times larger than the value provided by Huisman (-3.8 pcm K^{-1}), who neglected expansion effects [29].

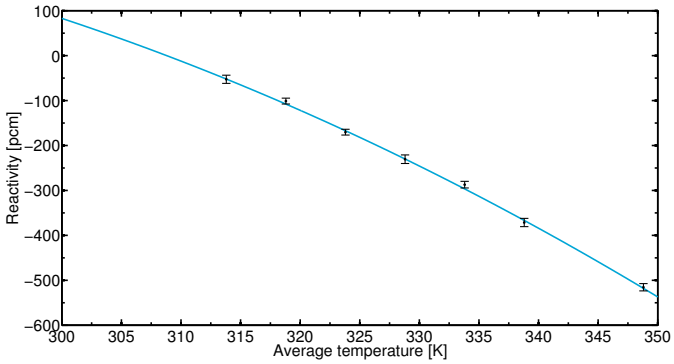

Figure 5.4: The negative temperature coefficient of reactivity is an important feedback mechanism of the AHR, and is shown above. Average temperatures up to 350 K are used for the fit, because the maximum temperature should stay below the boiling point.

5.5. REFLECTOR WATER LEVEL

If the water level in the water vessel drops as a result of a leak, the reactor loses (part of) the reflector, leading to an increased fraction of neutrons leaking from the reactor which will reduce the multiplication factor. Looking at the data, two regimes can be distinguished; therefore the fit of the data is split into two parts, see figure 5.5. Loss of the upper 30 centimeter of water will mainly affect the leakage from the top of the reactor, whereas loss of the lower 40 centimeter will influence mainly leakage through the side wall of the reactor vessel. The latter has an area that is 4 times as big as the top of the reactor. A decrease of the water level by one centimeter yields a decrease in reactivity of approximately 146 pcm when the water level is under 30 cm; for the upper part the effect is one order of magnitude smaller: approximately 15 pcm cm^{-1}.

As mentioned in section 3.5, the point kinetics model assumes that the flux changes only in amplitude. To check whether the change of the flux resulting from a decrease in water level fulfills this requirement, a plot (see figure 5.6) of the flux profile as function of the radius is made for a water level of 60 cm and 0 cm. The flux level is simular in both situations because the total flux is normalized to the same value for both calculations. However, from the plot it becomes clear that the flux profile changes in the transition from a reflected reactor to a bare reactor. As expected, the relative flux at the edge of the reactor is much smaller for a bare reactor than for a reflected reactor.

Although the requirement that the flux only changes in amplitude is not met, the point kinetics model will be used to calculate the transient behavior in case of a decrease of the reflector water level.

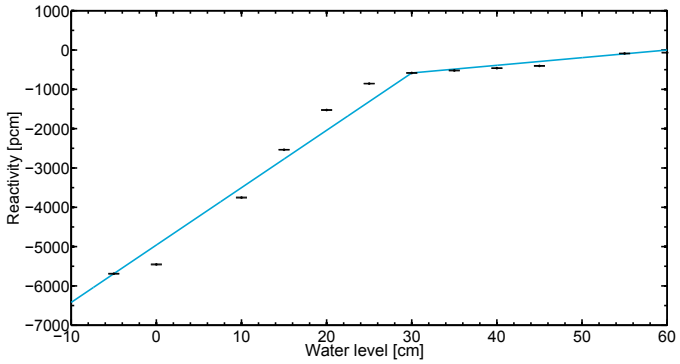

Figure 5.5: The fit of the data is split up into parts: the water part next to the fuel region shows a stronger reactivity coefficient. Where the two fits meet is a kink, which is a non-physical phenomenon, a consequence of evaluating the data as two different sets.

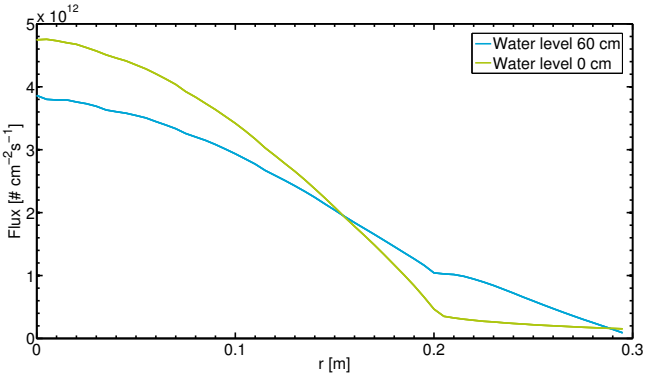

Figure 5.6: The plot above shows the scalar neutron flux profile as a function of the radius, evaluated at z = 10 cm. When the water is at the normal level (60 cm), the relative flux near the boundary is higher than when the water level has decreased to 0 cm, because the number of reflected neutrons is higher.

5.6. FUEL LEVEL

An increase in the fuel level results in a larger amount of uranium in the reactor core, presuming the average uranium concentration does not change. If the volume is increased, the non-leakage probability of a neutron is increased, causing a positive reactivity effect. Figure 5.7 shows a second order fit of the data points, which is used to calculate time-dependent reactivity values.

The larger fuel volume leads to a flux profile that is a little more spread out, as shown for three fuel levels in figure 5.8. Again the flux is normalized to the same value in the three calculations, leading to a similar amplitude.

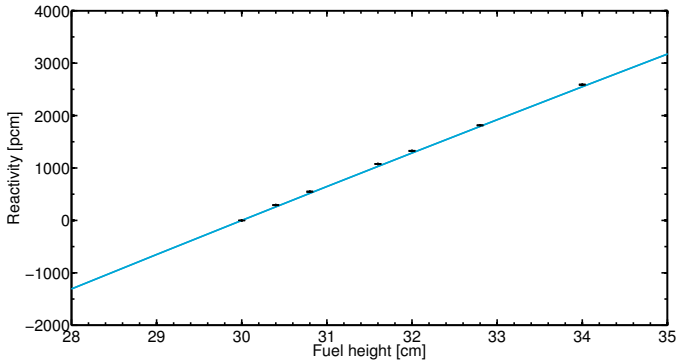

Figure 5.7: The fuel level has a large influence on the reactivity. This makes sense, because a 4 cm rise of the fuel level means the fuel volume is increased by 10%, which means the amount of uranium in the core is also increased by roughly 10%.

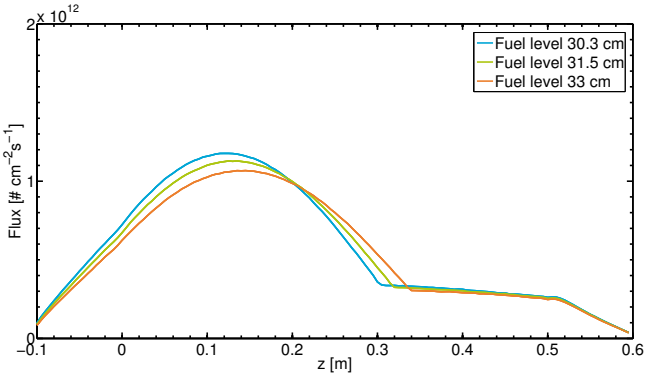

Figure 5.8: A higher fuel level leads to a changed flux profile; the flux is stretched somewhat in the vertical direction (shown on the horizontal axis). Because the flux is normalized to the same value for the three cases, a stretched flux leads to a lower maximum value.

5.7. FUEL CONCENTRATION IN PART OF THE WATER

In this section, a leak at the most central inflow pipe of the reactor vessel is assumed, causing a small concentration of uranium in the surrounding water. This will lead to an increase in power, because also fissions in the surrounding water will occur. To limit the amount of fuel solution in the water and the spreading of this fuel, the water can be kept in various compartments to prevent diffusion and convection of leaked fuel. Another option is to keep the pressure in the water outside the reactor core higher than the pressure of the solution in the reactor, in which case a leak in the reactor vessel will cause water to flow into the core, rather than fuel flowing out. In figure 5.9 the reactivity is shown for fuel leaking out of the most central reactor inflow pipe into the water directly around it (enclosed by the two most central inflow pipes). Because of the circular symmetry of the code, a leak will always be assumed circular.

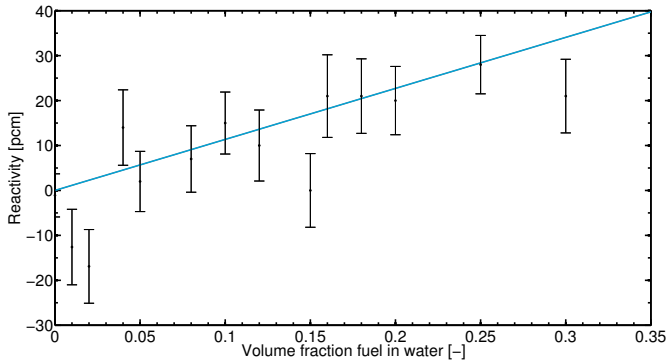

Figure 5.9: Fuel is assumed to only flow into the volume enclosed by the two inner inflow pipes. Although many data points are taken, the trend is not really clear. A linear fit is used as approximation for the data points, with an additional restriction for the fit to pass through (0,0).

5.8. LINEARITY OF FEEDBACK EFFECTS

A last step is the investigation of the mutual dependence of the reactivity coefficients. If there is no correlation, the total reactivity can be written as

$$\rho = \rho_0 + \Sigma_i \rho_i \tag{5.2}$$

with ρ_0 the initial reactivity, and ρ_i the reactivity changes resulting from the various possible events. To investigate the linearity of the reactivity effects, multiple events are simulated at once. Serpent is used to calculate the reactivity, which is then compared to the sum of the reactivities of the separate events. If no correlation between the effects exists, these values will be similar.

Looking at the values calculated by Serpent and the expectation based on addition of reactivities using (5.2) (available in appendix B for reference), it can be noted that there is no correlation between effects for all events considered except for one case. An increase in fuel level and a decrease in water level re-enforce each other, leading to a larger increase in reactivity than is expected from addition of the effects. Therefore, no events in which both the fuel level and the water level change have been considered in calculating the transient behavior.

Although the fit from section 5.7 does not seem to represent the data very well, the fit is used in calculation of the combined effects. It is worth noticing that calculation of the reactivity by Serpent in case of simultaneous perturbation of multiple parameters including the concentration of uranium in the surrounding water yields results which are consistent with the expected value calculated using (5.2).

6

TRANSIENT CALCULATIONS

Starting from the steady state situation as described in chapter 4.6, the transient behavior of the reactor is assessed for some events which are deemed probable. These include changes in the inflow conditions (uranium concentration, temperature of the fuel, flow rate), changes in ambient temperature and changes in the fuel and water level. The reactivity coefficients from chapter 5 are converted to a reactivity value, which is a function of time. With this value, the point kinetics equations (3.6a) and (3.6b) are solved. The neutron generation time in steady state operation $\Lambda = 6.1662 \cdot 10^{-5}$ s, the total delayed neutron fraction $\beta = 7.5891 \cdot 10^{-3}$. Other parameters that have to be put in to the equations are listed in table 6.2. These values are available from the Serpent calculation of the steady state situation.

Table 6.1: The group constants as used in the transient calculations, calculated by Serpent.

Group	β	λ [s^{-1}]	$t_{\frac{1}{2}}$ [s]
1	$2.447 \cdot 10^{-4}$	$1.249 \cdot 10^{-2}$	55.49
2	$1.269 \cdot 10^{-3}$	$3.182 \cdot 10^{-2}$	21.79
3	$1.225 \cdot 10^{-3}$	$1.094 \cdot 10^{-1}$	6.335
4	$3.471 \cdot 10^{-3}$	$3.172 \cdot 10^{-1}$	2.186
5	$1.021 \cdot 10^{-3}$	1.354	0.5121
6	$3.582 \cdot 10^{-4}$	8.649	0.0801

6.1. DELAYED NEUTRON FRACTION

These values for β, however, are calculated without considering that precursors flow out of the core. Assuming an average fuel residence time of 30 seconds, it is likely that part of the precursors (especially those with longer half-life) will decay outside the reactor vessel. Because neutrons released in decay of these precursors are not likely to induce a fission in the reactor vessel, the group constants of groups one to three are changed. The groups with a short half-life time are not affected by this assumption, as almost all precursors will decay before they flow out of the reactor.

Following the assumption that a precursor either decays in the core or flows out after 30 seconds, it can be calculated that the chance at decay inside the reactor for a precursor from group 1 is 41.8%, while for precursors in group 2 and 3 the chances are 74.8% and 99.1% respectively. The adapted group constants β_a are calculated by multiplying the group constant calculated by Serpent by the chance at decay inside the reactor vessel. The difference between the original β and the adapted

value β_a is 6.3%.

Table 6.2: The adapted group constants, calculated using $\beta_{a,i} = P_i(\text{decay}) \cdot \beta_i$ with $P_i(\text{decay})$ the chance that a precursor from group i decays inside the reactor vessel.

Group	β_a	λ [s^{-1}]	$t_{\frac{1}{2}}$ [s]
1	$1.023 \cdot 10^{-4}$	$1.249 \cdot 10^{-2}$	55.49
2	$9.492 \cdot 10^{-4}$	$3.182 \cdot 10^{-2}$	21.79
3	$1.210 \cdot 10^{-3}$	$1.094 \cdot 10^{-1}$	6.335

Two time evolutions starting from the steady state (starting with ρ = -1 pcm) have been calculated, one with the original value for β and one with the adapted value. As can be seen in the left graph in figure 6.1, the change in the delayed neutron fraction leads to difference in reactivity. The smaller fraction of delayed neutrons results in a more prompt reactor behavior, as can be seen by the shift of the curve to the left. The power, shown in the right diagram of figure 6.1, is not much different for the two values of β; the maximum difference between the two cases is only 0.05%. Based on these arguments, the original values of β are used in the transient calculations.

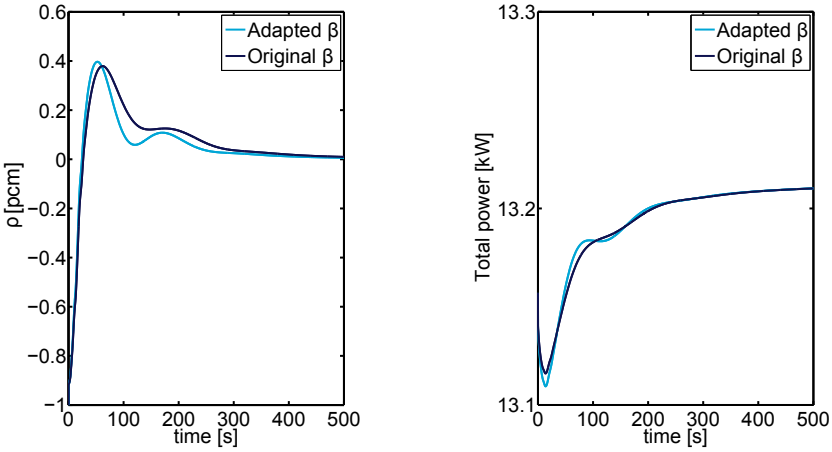

Figure 6.1: The reactivity in pcm as a function of time for the original and the adapted delayed neutron fraction. As the delayed neutron fraction decreases, the reactor reacts more promptly to changes, which is the cause of the steeper curve in case of an adapted value of β. The power variations are induced by the reactivity changes; for the smaller value of β the power changes are slightly larger, but the difference between the two situations is negligible.

6.2. URANIUM CONCENTRATION

In the reprocessing step, the fuel has to be prepared for a new cycle through the reactor. Assuming all fission products and radiolytic gases are extracted, only the uranyl sulfate and water remain. These have to be cooled, and the uranium concentration has to be set to 225 gL^{-1}. An error in the uranium concentration could lead to problems, due to the large reactivity coefficient of the uranium concentration, as discussed in chapter 5.1. An increase of the inlet concentration to 227 gL^{-1} is simulated, keeping all other parameters constant.

In approximately 300 seconds, the average uranium concentration in the reactor rises to its equilibrium level of 227 gL^{-1}. Because of the higher uranium concentration, the reactivity rises to 25 pcm, resulting in an increase in power. This leads to an increase in temperature, concentration

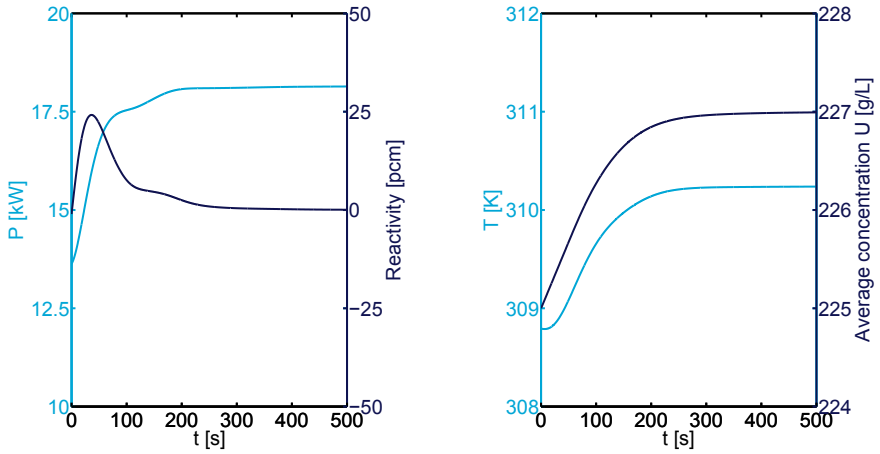

Figure 6.2: An increase in the uranium concentration will lead to an increase in reactivity. This leads to an increase in the power, which results in an increase of the temperature. Eventually (at $t \approx 300$ s) the reactivity effects of the changed temperature, ^{135}Xe concentration and void fraction will cancel out the increase in reactivity from the increased uranium concentration.The new steady state power is 18.2 kW

of ^{135}Xe and the average void fraction. All these events decrease the reactivity, which eventually becomes zero. The reactor now operates at a new steady state power of 18.2 kW, with an average temperature of 310.2 K

6.3. INFLOW RATE

Another parameter that could be set to a wrong value is the flow rate. In the reference situation, the inflow rate is set at 0.4 kgs^{-1}. If the inflow rate is lowered to 0.3 kgs^{-1}, the outflow rate will also decrease to 0.3 kgs^{-1}. This decrease in flow means that the fuel will spend more time in the reactor. Initially the power is at the steady state value, 13.2 kW. Because of the longer residence time the average fuel temperature, void fraction and ^{135}Xe concentration will rise. This will lead to a decrease of the reactivity, which in turn leads to a decrease in power. As the power decreases more and more, the fuel temperature, void fraction and ^{135}Xe concentration will drop again, resulting in a rise of the reactivity. After approximately 250 seconds the power settles at the new equilibrium level of 10.1 kW.

The inflow rate can also be set to a higher value than the 0.4 kgs^{-1}. An increased inflow rate will yield opposite effects from a decreased inflow rate. The fuel will flow faster, meaning it has less time to heat up. Also there is less buildup of fission products and radiolytic gas, leading to a positive reactivity. This positive reactivity results in an increase of the power, causing the temperature, ^{135}Xe concentration and void fraction to return to their equilibrium values. Figure 6.3 shows the development of both the total reactor power and temperature.

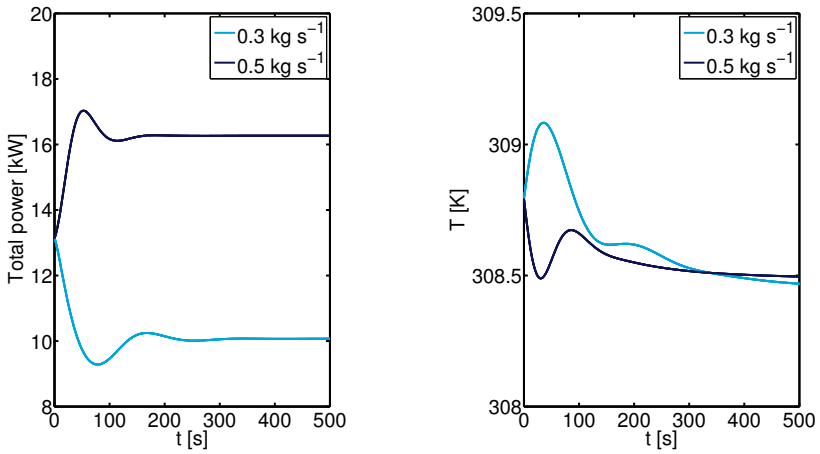

Figure 6.3: These graphs illustrate the power and temperature changes resulting from a changed inflow rate. If the inflow rate is increased (black), the power will initially rise, while the average temperature drops. For a decreased inflow rate (blue), the effects are reversed; the power initially increases and the temperature decreases. After approximately 300 seconds, the power has settled at a new steady state level.

6.4. NO INFLOW

The fuel is pumped through the reactor core, and stops flowing when the pump stops. In that case, there is neither inflow nor outflow, so the fuel will spend a longer time in the reactor core. The cooling by the water is not sufficient to transport all extra heat to the surroundings, so the fuel temperature will increase. Also, the void fraction and ^{135}Xe concentration will increase because no fresh fuel is pumped into the core. These three effects lead to a reduction of the reactivity, which is large enough to stop the reactor ($P = 0$). When the power is almost at zero, the temperature starts to decrease gradually because heat is transferred to the environment. The void fraction stays at the same level, because the code does not support void escaping from the fuel. In reality, however, the void bubbles will rise to the surface of the fuel. Due to decay of ^{135}I, the ^{135}Xe concentration will initially increase. After approximately 2.5 hours the average temperature of the fuel is decreased to the same level as before the inflow stopped (see figure 6.4).

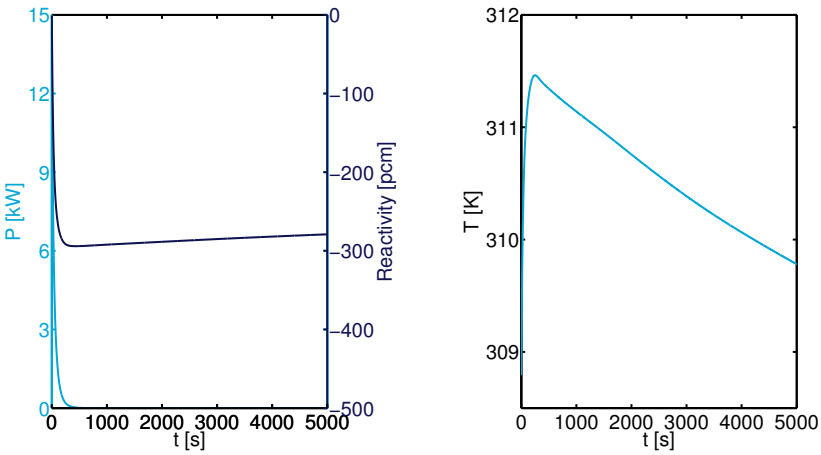

Figure 6.4: If the fuel flow is stopped, a large negative reactivity is introduced as a result of the increase of the void fraction, ^{135}Xe concentration and temperature. After approximately 200 seconds, the temperature will decrease due to heat transfer through the reactor vessel wall, the void and xenon however stay in the fuel and cause the reactor to shut down.

6.5. NO COOLING

Because the heat transfer from the reactor to the surroundings is insufficient to dissipate all fission heat, the fuel is cooled externally after it has left the core. In case of a failure of the cooling system, the fuel will be reinserted in the reactor at a higher temperature. Even when the heat exchange system fails the fuel temperature will decrease somewhat before it is reinserted, but to be conservative for calculating the transient the inflow temperature is set equal to the outflow temperature.

The average temperature will increase because of the high inflow temperature, causing a negative reactivity. This causes the power to decrease, which limits the temperature rise. Furthermore, the decreasing power induces a decrease in ^{135}Xe concentration and void fraction, which has a positive effect on the reactivity, limiting the drop of the power. The average temperature, shown in figure 6.5, rises to approximately 356.3 K while the maximum temperature of the fuel stays at 359.9 K which is well below the boiling point (the boiling point of an aqueous solution is always higher than the boiling point of pure water [55]). Considering the fact that this calculation is conservative, it can be stated that safe operation is ensured in the event of loss of external cooling.

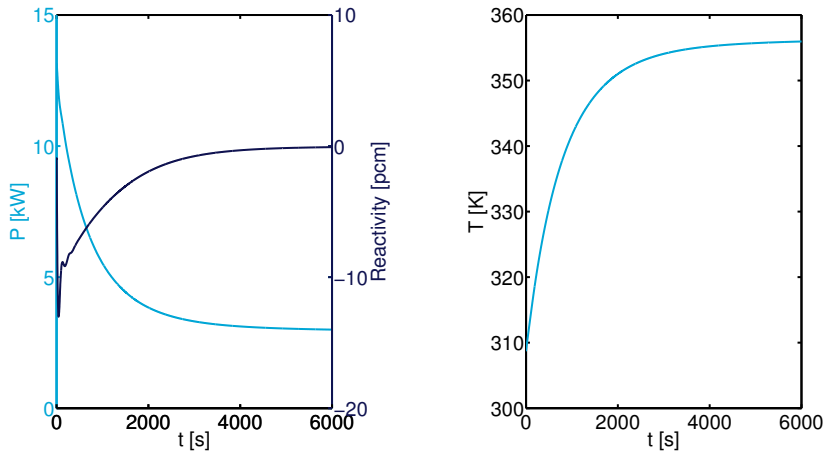

Figure 6.5: The increasing fuel temperature creates a negative reactivity, which causes the power to decrease. As a result the production of void and ^{135}Xe diminishes, leading to an increase in reactivity. Eventually, the effects cancel each other out at a power of 2.94 kW. The average temperature at this power level is lower than 360 K.

6.6. INCREASE IN AMBIENT TEMPERATURE

Until now, all described transients scenarios result from flaws in either the fuel processing or the inflow conditions. However, changes in external parameters can also affect the reactor. The ambient temperature is important for the heat transfer from the reactor vessel to the surroundings. The higher the ambient temperature, the less efficient the cooling of the reactor vessel. To investigate the impact of a deteriorated heat transfer from the reactor, the ambient temperature is increased from 293 K to 313 K.

As it turns out, the 20 K increase in ambient temperature does not have a large influence on the reactor characteristics. The amount of heat that is transferred from the fuel to the surroundings will decrease slightly, but the influence on the average temperature is negligible. Initially, the power will fluctuate a little, because the initial reactivity is slightly less than 0.

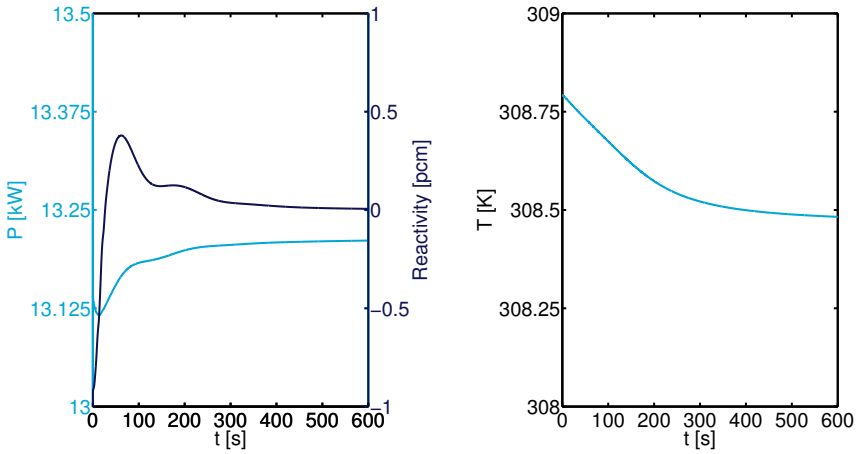

Figure 6.6: Initially, the reactivity is negative, which leads to a small decrease in power. This induces an increase in reactivity resulting from void, temperature and ^{135}Xe feedback. The reactivity then slightly overshoots, which causes the power to increase and eventually settle at 13.2 kW.

6.7. INCREASE IN FUEL LEVEL

Another possible event is a change of the fuel level in the reactor. In this section, continuous fuel flow is assumed. The maximum fuel level can be limited by placing an extra outlet at 30.5 cm, just above the wanted fuel level (30 cm). Assuming such a pipe is placed, the fuel level is raised to 30.5 cm instantaneously. This leads to an enormous increase in reactivity, shown in figure 6.7, because of the large fuel level coefficient of the reactivity (650 pcm cm^{-1}). This increase in reactivity is followed by a power excursion to 52 kW, leading to an increase in temperature, void fraction and ^{135}Xe concentration. As soon as these three rise, the reactivity decreases until it eventually becomes zero. The new steady state power is 22.5 kW, and the average temperature has risen to 312.3 K.

As described, a small change in the fuel level already leads to a power excursion with a peak power of four times the initial steady state power. One can imagine that a rise of the fuel level with several centimeters can have large consequences, which is why extra attention should be paid to the design of a safety system that prevents the fuel level to rise too far. In such a case, the negative reactivity effect caused by the rising temperature, void fraction and ^{135}Xe concentration is not enough to compensate for the increase in reactivity caused by the increase in fuel volume. In figure 6.8, the power excursion caused by an instantaneous increase of the fuel level with 2.5 cm is shown. Due to the large increase in reactivity, the reactor is supercritical on prompt neutrons alone. As a result, the power rises very quickly, which causes the fuel temperature to rise as well. For high power levels the results may be unreliable, because physical effects such as boiling are not incorporated in the code.

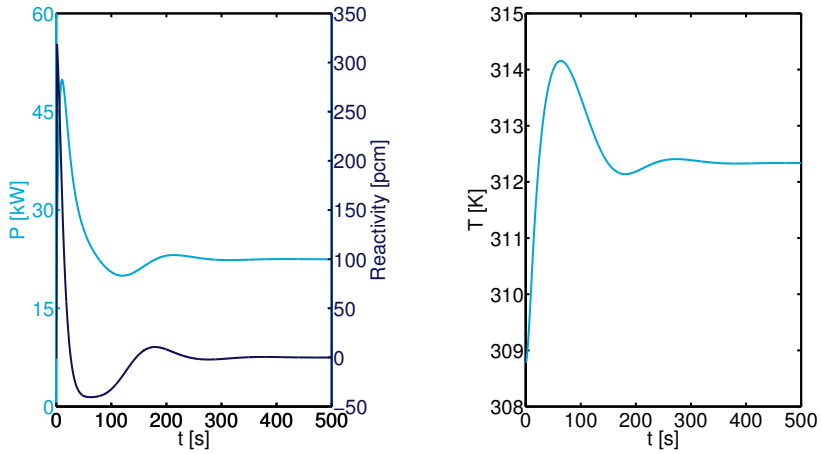

Figure 6.7: The rise of the fuel level leads to a large positive reactivity, resulting in a power excursion to 49.9 kW. This power excursion leads to an increase in the three parameters that provide negative feedback: temperature, void fraction and ^{135}Xe concentration. As soon as the power rises, these three increase, counteracting the large positive reactivity. After the excursion, the power stabilizes at 22.5 kW.

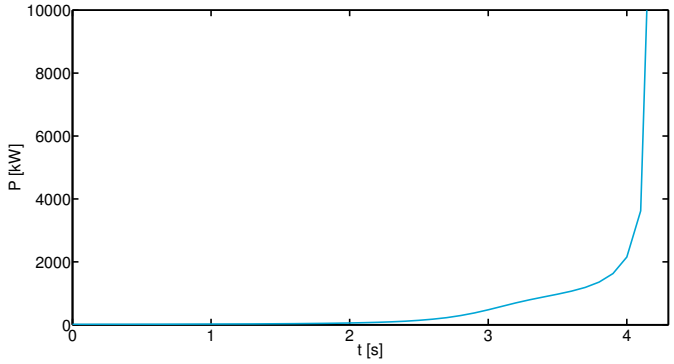

Figure 6.8: If the fuel level suddenly rises with 2.5 cm an enormous amount of reactivity is added, leading to a large power excursion.

6.8. BLOCKAGE OF OUTFLOW PIPE

Another possible event is a blocked outflow pipe, which can lead to a slightly higher fuel level. The situation examined is a combination of the situations described in sections 6.4 and 6.7; the fuel level rises and no fuel flows out of the reactor (unlike in the previous section, where continuous fuel flow was assumed). Three different calculations are carried out, in which the fuel level increases by 0.1, 0.2 and 0.3 cm respectively. In these calculations the fuel level rises gradually until the final height is reached. This leads to the increases in reactivity which can be seen in figure 6.9, which causes an increase in the total reactor power, shown in figure 6.10. As soon as the final fuel level is reached, the reactivity starts to decrease as a result of the negative feedback effects of temperature, void fraction and ^{135}Xe concentration. Because the fuel cannot flow out of the reactor, the created void bubbles and ^{135}Xe stay in the reactor, causing a large negative reactivity, even when the power decreases to low levels. Just as in section 6.4, the void bubbles do not escape the fuel solution, whereas in reality they will rise to the surface of the fuel solution.

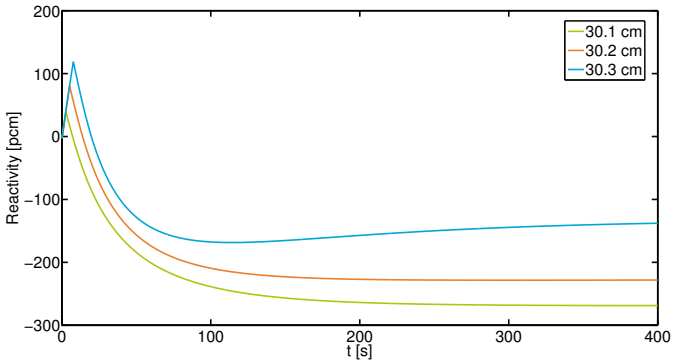

Figure 6.9: The initial reactivity rise is an effect of the gradual increase of the fuel level. Once the fuel level stops rising the negative reactivity feedback effects lead to a decrease in the reactivity, which eventually becomes negative.

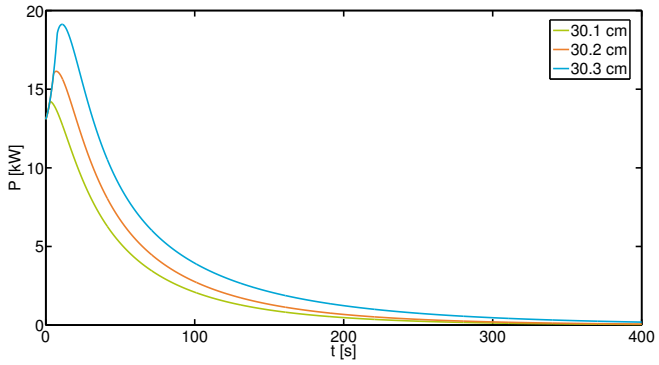

Figure 6.10: For the 0.3 cm rise in fuel level, the maximum power level is 19.8 kW, 11 seconds after the fuel level starts to rise. Obviously, a larger increase in fuel level results in a higher maximum power. The horizontal shift of the peaks is a result of the gradually increasing fuel level. The negative feedback effects eventually cause a negative reactivity, causing the power to decrease to almost zero.

6.9. WATER LEAK FROM THE WATER VESSEL

The next transient simulated is the outflow of water from the water vessel, for example because of a leak. Assumed is that the water flows out at the bottom of the vessel with a rate of 0.1 Ls^{-1}. This means that the water level will drop slowly at first, until it has reached 50.5 cm (the top of the reactor vessel). After that the drop in height will be quicker, because the area of the water is much smaller.

The negative reactivity introduced by the decrease in water level leads to a reduction in power. It is partly compensated for by the positive reactivity from the decrease in temperature, void fraction and ^{135}Xe concentration resulting from the decreased power. However, as the water level keeps decreasing, the negative reactivity effect keeps growing. Therefore, the power keeps decreasing as well. When the water level reaches the 30 centimeter mark, the negative reactivity grows very fast, as shown in figure 5.5. This leads to an even quicker decrease of the reactor power, which will eventually become zero (see figure 6.11). At zero power, the average ^{135}Xe concentration and void fraction will decrease to zero, because no new fission products and radiolytic gas are produced. Also, the average temperature will decrease to slightly below the inlet temperature.

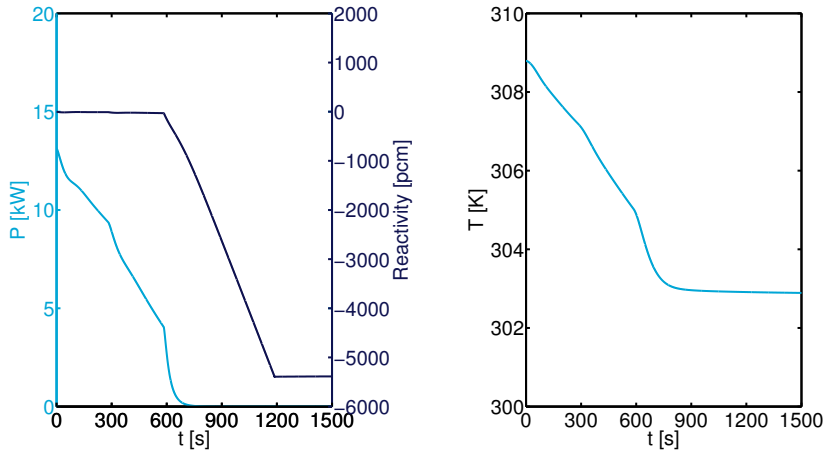

Figure 6.11: During the first 10 minutes, the power gradually decreases due to the negative reactivity. After approximately 600 seconds the water level decreases to below the 30 cm. From this point on, the reactivity effect is enhanced (see figure 5.7) which explains the kink in the upper graph. The power decreases to zero quickly after that; the temperature decreases to 302.9 K.

6.10. FUEL LEAK FROM THE REACTOR VESSEL

In the previous situation, water was leaking from the water vessel, but a leak in the reactor core vessel could also occur, causing fuel to flow into and mix with the surrounding water. The effect of a small amount of fuel leaking into the surrounding water near the most central inflow pipe of the reactor is simulated. As explained in section 5.7, the fuel is contained in the small volume of water between the two most central inflow pipes. The volume fraction of fuel solution in this part of the surrounding water is increased to 50% in 500 seconds, which causes a reactivity peak of 2.5 pcm after 50 seconds. After that, the power has risen to a level at which the negative reactivity effects compensate for the largest part the increase in reactivity caused by the leak. Because the volume fraction of the fuel solution in the surrounding water keeps increasing until $t = 500$ s, the reactivity stays just a bit above zero (around 1.5 pcm), which causes the power to increase gradually. After 500 seconds, the volume fraction of fuel stops increasing while the temperature still rises, which causes the negative reactivity. After this, the power stabilizes and the new steady state power is 14.3 kW, which can be seen in figure 6.12.

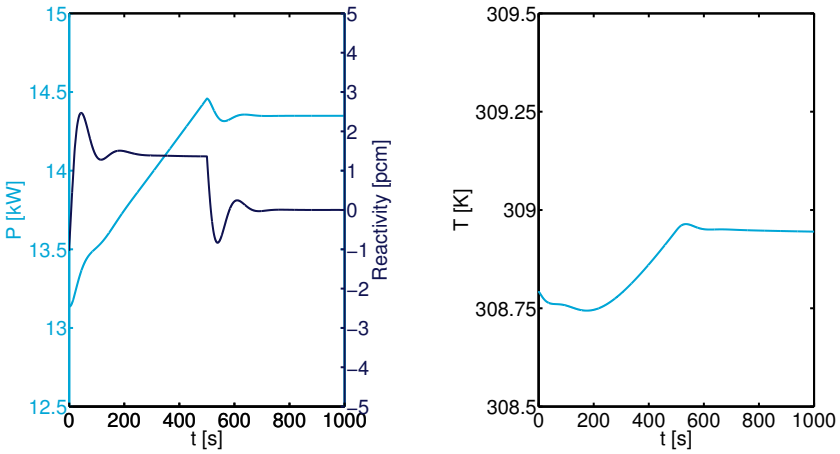

Figure 6.12: The increase of fuel solution in the surrounding water leads to an increased reactivity, which in turn leads to an increase in power. This increase in power causes negative reactivity feedback, causing the feedback coefficient to be just above zero. At $t = 500$ s, the increase in reactivity due to the fuel leak stops, while the negative reactivity feedback still increases. This causes a temporary negative reactivity, after which the power settles at 14.3 kW

6.11. SUMMARY

Looking at the results discussed in this chapter, the potential risk of the simulated events can be assessed. Most of the situations investigated only lead to slight changes in power (change in inflow rate, change in uranium concentration, fuel leak from the reactor) or a shutdown of the reactor (water leak from the water vessel, stop of fuel flow). Safe operation is also ensured if the external cooling of the fuel fails or the ambient temperature increases, as the maximum temperature of the fuel stays below the boiling point.

The largest potential risk encountered is an increase in fuel level large enough to cause prompt criticality. Therefore, measures should be taken to prevent the fuel level from rising above a threshold, for example by placing outflow pipes just above the fuel level.

7

CONCLUSION AND OUTLOOK

7.1. CONCLUSIONS

The need for an alternative method to produce medical isotopes grows, as the current production reactors are aging and become less reliable. Combined with the increasing worldwide demand and the transport challenges, this can lead to (local) shortages of medical isotopes, directly affecting medical care.

One of the alternatives to produce medical isotopes on a small scale is a small aqueous homogeneous reactor (AHR). Throughout the years, many AHRs with different fuels and geometries have been built and operated safely. Additional advantages of an AHR include the possibility to do both the production and extraction at one site, and the noticeable decrease in waste production. Even though this thesis focuses on the production of ^{99}Mo, as this is the most used medical isotope, a modification to the extraction component can be made to extract other elements.

The fuel for an AHR is an aqueous solution of a uranyl salt, in this project chosen to be uranyl sulfate, containing 20% enriched uranium, which is in line with the Non-Proliferation Treaty. Uranyl sulfate is chosen because of the extensive knowledge about its use in AHRs, the >90% extraction yield of ^{99}Mo and the behavior of the fuel in the core regarding pH stability and radiolytic gas production.

An existing computational model has been used to investigate the operation of an AHR, consisting of four coaxial inflow annuli and a central outflow pipe, through which a uranyl sulfate solution is continuously pumped. The model is a combination of a CFD code to calculate the fuel flow in the core based on a specific power distribution, and a Monte Carlo reactor physics code for calculation of the power profile. Improvements to both the geometry and the code have been made, and implementation of these have led to an increasingly realistic description of the system. To check the physical correctness, the results of the model should be validated against real values.

Using the aforementioned model, a description of a steady state operation of the AHR design has been made. Fueled by a uranyl sulfate solution with a uranium concentration of 225 gL^{-1}, it operates at relatively low power and low temperature. In the described steady state, the reactor is theoretically able to produce approximately 2% of the global demand, assuming a daily transport from the reactor facility. The output can be increased by switching to a higher concentration uranyl sulfate solution. However, this also increases the operating temperature and power.

A safety assessment of the design has been made using a point kinetics model. Using the correlations between various reactor and fuel characteristics and their effects on the reactivity of the system, an estimate of the transient behavior has been made to check whether safe operation can be ensured in a variety of unanticipated events. Investigating the transient behavior, the large rise of the fuel level in the core seems to be the most risky event as it induces a large increase in reactor power. By placing an extra outflow pipe just above the desired fuel level, this hazard can be circumvented. Again, the correctness of the transient calculations should be confirmed by validating the model against experiments.

7.2. OUTLOOK

One of the points of interest for future research might be the fuel preparation. Whereas in this thesis only the extraction of ^{99}Mo is considered, one might look into the process of extracting other fission products. It might be that other medical isotopes such as ^{123}I and ^{131}I can be extracted more efficiently from another type of uranyl salt. Also, precaution measures should be taken to ensure that the uranium concentration is kept at the appropriate level.

If more knowledge about the filtering step is obtained, a better description of the contents of the inflowing fuel can be made. For this project, all inflowing fuel is considered uncontaminated, but if the reprocessing is imperfect, the fuel composition will change over time, which might affect the reactor characteristics.

To improve the models even further, a two-phase fluid dynamics code should be adapted to properly describe the behavior of gas bubbles in the fuel solution. High local power densities may lead to larger gas bubbles which rise through the fuel. Whereas with the current codes the fuel composition in steady state is assumed constant in time, these rising bubbles may lead to time dependency.

If this time dependency is taken into account, it would be useful to use another code to calculate the power based on the fuel composition. The calculations using Serpent are very time consuming. It would be ideal to have a neutronics code to work in fully coupled mode with the CFD code. In that way, also the convection of precursors can be taken into account.

Another aspect worth looking into deeper is the geometry of the reactor core. Different geometries could be tested to check their performance. One could think of changing the inlets to a perforated circular plate, for example. Also, pumping the fuel through the reactor from bottom to top or from top to bottom or horizontally might be an option.

What is needed to determine the credibility of the results is a validation of the code. To check the physical correctness, one could simulate an AHR that has actually been built and compare the results with the reality, or set up experiments for validation.

An economical analysis of the concept has to be made, to investigate the feasibility of the proposed production method. This analysis should provide answers to questions about, for example, the optimal production capacity of a reactor in terms of operational costs, and compare the proposed production method to alternative methods.

BIBLIOGRAPHY

[1] W. G. Davey. An evaluation of the number of neutrons per fission for the principal plutonium, uranium, and thorium isotopes. *Nuclear Science and Engineering*, 44:345–371, 1971.

[2] H.D. Selby, M.R. Mac Innes, D.W. Barr, A.L. Keksis, R.A. Meade, C.J. Burns, M.B. Chadwick, and T.C. Wallstrom. Fission product data measured at Los Alamos for fission spectrum and thermal neutrons on ^{239}Pu, ^{235}U, ^{238}U. *Nuclear Data Sheets*, 111:2891–2922, 2010.

[3] J. J. Duderstadt and L. J. Hamilton. *Nuclear Reactor Analysis*. Wiley, 1976.

[4] IAEA. Production and supply of molybdenum-99. *Annex to Nuclear Technology Review*, 2010.

[5] L. H. Kahn. The potential dangers in medical isotope production. *Bulletin of the Atomic Scientists*, 2008.

[6] I. Zolle. *Technetium-99m Pharmaceuticals*. Springer, 2007.

[7] B. Ponsard. Mo-99 supply issues: Status report and lessons learned. *RRFM, Marrakech, Morocco*, 2010.

[8] A. Nagurney and L. S. Nagurney. Medical nuclear supply chain design: A tractable network model and computational approach. *International Journal of Production Economics*, 140:865–874, 2012.

[9] OECD. The supply of medical radioisotopes: An assessment of long-term global demand for technetium-99m. *Nuclear Energy Agency*, 2011.

[10] Kamerstuk Tweede Kamer. Notitie toekomst productie van radiofarmaca. 2009.

[11] OECD. The supply of medical radioisotopes – a path to reliability. *Nuclear Energy Agency*, 2011.

[12] B. Wolterbeek, J. L. Kloosterman, D. Lathouwers, M. Rohde, A. Winkelman, L. Frima, and F. Wols. What is wise in the production of ^{99}Mo? A comparison of eight possible production routes. *J. Radioanal. Nucl. Chemistry*, 2014.

[13] D. Updegraff and S. A. Hoedl. Nuclear medicine without nuclear reactors or uranium enrichment. 2013.

[14] Treaty on the non-proliferation of nuclear weapons. *United Nations*, 1968.

[15] International Atomic Energy Agency. Homogeneous aqueous solution nuclear reactors for the production of Mo-99 and other short lived radioisotopes. September 2008.

[16] M. E. Bunker. Early reactors, from Fermi's water boiler to novel power prototypes. *Los Alamos Science*, 7:124–131, 1983.

[17] J. A. Lane. *Aqueous Homogeneous Reactors*. Addison-Wesley, 1958.

[18] L. B. Borst. Design comparison of reactors for research. *Annual Review of Nuclear Science*, 5:179–196, 1955.

[19] J. R. Ireland. Design principals for aqueous homogeneous reactors. *LANL report*, LA-UR 11-06788, 2011.

[20] M. W. Rosenthal. An account of Oak Ridge National Laboratory's thirteen nuclear reactors. *ORNL Report*, ORNL/TM-2009/181, 2009.

[21] S. V. Myasnikov, A. K. Pavlov, N. V. Petrunin, and V. A. Pavshook. Conversion of the ARGUS solution reactor to LEU fuel: Results of feasibility studies and schedule. *RERTR 2012 - 34th international meeting on reduced enrichment for research and test reactors*, 2012.

[22] B. Tournier, F. Barbry, and B. Verrey. SILENE, a tool for neutron dosimetry. *Radiation Protection Dosimetry*, 70:345–348, 1997.

[23] H. Glandais and P. Fouillaud. Test potential of the CEA Valduc critical laboratory. *Workshop on future criticality safety research needs*, Pocatello, Idaho, USA, September 2009.

[24] X. Song and W. Niu. Optimization of 200kW medical isotope production reactor design. *Sichuan Nuclear Society*, Nuclear Power Institute of China, 2000.

[25] Deng Qimin Li Maoliang, Cheng Zuoyong. The progress report of aqueous homogeneous reactor for medical isotope production in China. *Nuclear Power Institute of China*.

[26] S. Tegas Sutondo and S. Slamet. Safety design limits of main components of the proposed SAMOP system. *Proceedings of the 3rd Asian Physics Symposium*, Bandung, Indonesia, 2009.

[27] R. H. Kimpland. SHEBA prompt burst dynamics. *Los Alamos National Laboratory*, LA-UR-97-4736, 1997.

[28] C. C. Capiello, K. B. Butterfield, R. G. Sanchez, J. A. Bounds, R. H. Kimpland, R. P. Damjanovich, and P. J. Jaegers. Solution High-Energy Burst Assembly (SHEBA) results from subprompt critical experiments with uranyl fluoride fuel. *Los Alamos National Laboratory*, LA-23373-MS, 1997.

[29] M. V. Huisman. Medical isotope production reactor. Master's thesis, TU Delft, 2013.

[30] T. Setiadipura and E. Saragi. Neutronic aspect of subcritical assembly for mo-99 production (SAMOP) reactor. In *International Conference on Advances in Nuclear Science and Engineering*, 2007.

[31] A. J. Youker, S. D. Chemerisov, M. Kalensky, P. Tkac, D. L. Bowers, and G. F. Vandegrift. A solution-based approach for Mo-99 production: considerations for nitrate versus sulfate media. *Science and technology of nuclear installations*, 2013.

[32] IAEA. Non-HEU production technologies for molybdenum-99 and technetium-99m. *IAEA Nuclear Energy Series*, 2013.

[33] N. N. Ponomarev-Stepnoy, V. A. Pavshook, G. F. Bebikh, V. Y. Khvostionov, P. S. Trukhlyaev, and I. K. Shvetsov. Method and apparatus for the production and extraction of molybdenum-99, October 1999.

[34] http://www.ncnr.nist.gov/resources/n-lengths/.

[35] N. N. Ponomarev-Stepnoy, V. A. Pavshook, G. F. Bebikh, V. Y. Khvostionov, P. S. Trukhlyaev, I. K. Shvetsov, and Y. L. Vandysh. Maleic anhydride polymer modified with benzoin oxime, October 1999.

[36] D. C. Stepinski, A. V. Gelis, P. Gentner, A. J. Bakel, and G. F. Vandegrift. Evaluation of Radsorb, Isosorb (Thermoxid) and PZC as potential sorbents for separation of 99-Mo from a homogeneous-reactor fuel solution. *Argonne National Laboratory*, Chemical Engineering Division, 2007.

[37] N.D. Betenekov, E.I. Denisov, T.A. Nedobukh, and L.M. Sharygin. Inorganic sorbent for molybdenum-99 extraction from irradiated uranium solutions and its method of use, January 2002. US Patent 6,337,055.

[38] L. Ling, P. Chung, A. Youker, D. C. Stepinski, G. F. Vandegrift, and N. L. Wang. Capture chromatography for Mo-99 recovery from uranyl sulfate solutions: Minimum-column-volume design method. *Journal of Chromatography A*, 1309:1–14, 2013.

[39] R. H. Kimpland. *A multi-region computer model for predicting nuclear excursions in aqueous homogeneous solution assemblies*. PhD thesis, University of Arizona, 1993.

[40] F. J. Souto, R. H. Kimpland, and A. S. Heger. Analysis of the effects of radiolytic-gas bubbles on the operation of solution reactors for the production of medical isotopes. *Nuclear Sc*, 150:322–335, 2005.

[41] P. Spiegler, C. F. Bumpus, and A. Norman. Production of void and pressure by fission track nucleation of radiolytic gas bubbles during power bursts in a solution reactor. Technical report, Atomics International, 1962.

[42] F. J. Souto and A. S. Heger. A model to estimate volume change due to radiolytic gas bubbles and thermal expansion in solution reactors. Technical report, Los Alamos National Laboratory, 2001.

[43] F. J. Souto and R. H. Kimpland. Reactivity analysis of solution reactors for medical-radioisotope production. *Nuclear Instruments & Methods in Physics Research, Section B*, 213:369–372, 2004.

[44] H. M. Forehand. *Effect of Radiolytic gas on nuclear excursions in aqueous solutions*. PhD thesis, University of Arizona, 1981.

[45] L. A. Glasgow. *Transport Phenomena, an introduction to advanced topics*. Wiley, 2010.

[46] C. M. Cooling, M. M. R. Williams, E. T. Nygaard, and M. D. Eaton. The application of polynomial chaos method to a point kinetics model of MIPR: an aqueous homogeneous reactor. *Nuclear Engineering and Design*, 262:126–152, 2013.

[47] L. P. B. M. Janssen and M. M. C. G. Warmoeskerken. *Transport Phenomena Data Companion*. VSSD, 1987.

[48] D. C. Giancoli. *Physics for Scientists & Engineers*. Pearson Education International, 1984.

[49] E. Orban, M. K. Barnett, J. S. Boyle, J. R. Heiks, and L. V. Jones. Physical properties of aqueous uranyl sulfate solutions from 20 to 90 degrees. *Journal of Physical Chemistry*, 60:413–415, 1956.

[50] P. S. Epstein and M. S. Plesset. On the stability of gas bubbles in liquid-gas solutions. *The Journal Of Chemical Physics*, 18:1505–1509, 1950.

[51] T. Sutondo. Analytical method of atomic density determination of the uranyl nitrate solution system.

[52] J. R. Welty, C. E. Wicks, R. E. Wilson, and G. L. Rorrer. *Fundamentals of Momentum, Heat, and Mass Transfer*. John Wiley & Sons, 2008.

[53] H.K. Versteeg and W. Malalasekera. *An introduction to computational fluid mechanics*. Longman Scientific & Technical, 1995.

[54] J. Leppänen. Serpent - a continuous-energy monte carlo reactor physics burnup calculation code, 2013.

[55] P. Atkins and J. de Paula. *Physical Chemistry*. W.H. Freeman and company, 2006.

[56] R.B. Bird, W.E. Stewart, and E.N. Lightfoot. *Transport Phenomena*. John Wiley & Sons, 1960.

LIST OF ABBREVIATIONS

AHR	Aqueous Homogeneous Reactor
BR-2	Belgian Reactor - 2 (Mol, Belgium)
CFD	Computational Fluid Dynamics
CRAC	Conséquences Radiologiques d'un Accident de Criticité
HEU	Highly Enriched Uranium
HFR	Hoge Flux Reactor (High Flux Reactor)
HOR	Hoger Onderwijs Reactor
HRE	Homogeneous Reactor Experiment
HRT	Homogeneous Reactor Test
HYPO	High Power
LEU	Low Enriched Uranium
LOPO	Low Power
MIPR	Medical Isotopes Production Reactor
NPIC	Nuclear Power Institute of China
NRU	National Research Universal
OECD	Organisation for Economic Co-operation and Development
ORNL	Oak Ridge National Laboratory
PZC	Polyzirconium compound
SAFARI-1	South African Fundamental Atomic Research Installation-1
SAMOP	Subcritical Assembly for Molybdenum Production
SHEBA	Solution High-Energy Burst Assembly
SILENE	Source d'Irradiation à Libre Evolution Neutronique
SIMPLE	Semi-Implicit Method for Pressure-Linked Equations
SUPO	Super Power

LIST OF SYMBOLS

Symbol	Property	Unit
α	Void fraction	-
α_T	Temperature feedback coefficient	-
β	Thermal expansion coefficient	-
β	Delayed neutron fraction	-
γ	Production yield	-
ϵ	Accuracy	-
ϕ_m	Mass flow	kgs^{-1}
ϕ''_q	Heat flux	$Js^{-1}m^{-2}$
ϕ_q	Heat flow	Js^{-1}
Λ	Neutron generation time	s
λ	Thermal conductivity	$Jm^{-1}s^{-1}K^{-1}$
λ	Decay constant	s^{-1}
μ	Dynamic viscosity	Pa·s
ν	Average number of neutrons produced per fission	-
ρ	Density	kgm^{-3}
ρ	Reactivity	pcm
Σ	Macroscopic cross section	m^{-1}
σ	Surface tension	Nm^{-1}
τ	Mean lifetime	s
χ	Fraction of produced neutrons per unit energy	-
Ψ	Angular neutron flux	$m^{-2}s^{-1}$
Ω	Volume	m^3
A	Area	m^2
C_p	Specific heat	$Jkg^{-1}K^{-1}$
C	Precursor concentration	-
c	Concentration	gm^{-3}
D	Diameter	m
$\mathscr{D}$	Diffusion coefficient	m^2s^{-1}
E	Energy	J
F	Force	N
f	Weight fraction	-
$\vec{f}$	Force per unit volume	Nm^{-3}
$G(x)$	Radiolytic yield for type x	J^{-1}
g	Gravitational acceleration	ms^{-2}
h	Height	m
K_z	Equilibrium constant	-
k	Multiplication factor	-
L	Length	m
M	Molar mass	$gmol^{-1}$

Symbol	Property	Unit
m	Mass	kg
N_A	Avogadros number	mol^{-1}
N	Number density	dm^{-3}
n	Amplitude factor	-
P	Power	Js^{-1}
p	Pressure	Nm^{-2}
p	Power per unit volume	$\mathrm{Js}^{-1}\mathrm{m}^{-3}$
p	Enrichment	-
q	Charge conversion factor	$\mathrm{J\,eV}^{-1}$
R_g	Gas constant	$\mathrm{Jmol}^{-1}\mathrm{K}^{-1}$
r	Radius	m
S	Production rate	$\mathrm{m}^{-3}\mathrm{s}^{-1}$
S	Neutron source	$\mathrm{m}^{-3}\mathrm{s}^{-1}$
T	Temperature	K
t	Time	s
u	Horizontal speed	ms^{-1}
V	Volume	m^3
v	Speed	ms^{-1}
v	Volume fraction	-
z	Height	m
Gr	Grashof number	-
Nu	Nusselt number	-
Pr	Prandtl number	-
Ra	Rayleigh number	-
Re	Reynolds number	-

A

DISCRETIZATIONS

A.1. DISCRETIZATION OF THE NAVIER-STOKES EQUATIONS

The Navier-Stokes equation can be written as in (A.1), however, it should be rewritten to a form usable in the computational codes as described in chapter 3.2. Therefore, the equation is written in discretized form, providing equations for each cell in the grid. The main target is to arrive at an equation of the form $A\mathbf{x} = \mathbf{s}$, with A the component matrix, $\mathbf{s}$ the source vector and $\mathbf{x}$ the solution vector in which we are the most interested. Showing how to assemble the component matrix and the source vector is the main goal of this appendix.

$$\rho \frac{\partial \vec{v}}{\partial t} + \rho \left(\vec{v} \cdot \nabla\right) \vec{v} = \nabla \cdot \vec{T} - \nabla p + \vec{f} \tag{A.1}$$

From the continuity equation the divergence of the flow speed $\vec{v}$ can be determined using the notion that ρ is taken as a constant both in time and in space (fluctuations in ρ are dealt with by introducing the Boussinesq approximation, as discussed in chapter 2.3)

$$\frac{\partial}{\partial t}\rho + \nabla \cdot \rho \vec{v} = 0 \tag{A.2a}$$

With the notion that ρ is constant

$$\rho \left(\nabla \cdot \vec{v}\right) = 0 \tag{A.2b}$$

$$\nabla \cdot \vec{v} = 0 \tag{A.2c}$$

This conclusion can be used to simplify the tensor $\vec{T}$:

$$\vec{T} = \mu \left[\left(\nabla \vec{v} + \nabla \vec{v}^T\right) - \frac{2}{3} \nabla \cdot \vec{v} I \right] = \mu \left(\nabla \vec{v} + \nabla \vec{v}^T\right) \tag{A.3}$$

If the equation is considered for a certain volume, i.e., a cell taken from our grid, (A.1) has to be integrated over that volume Ω. This yields advantages, because some of the terms can be written as boundary (surface) integrals rather than volume integrals.

$$\int_\Omega \rho \frac{\partial \vec{v}}{\partial t} \mathrm{d}\Omega + \int_\Omega \rho \left(\vec{v} \cdot \nabla\right) \vec{v} \mathrm{d}\Omega = \int_\Omega \nabla \cdot \vec{T} \mathrm{d}\Omega - \int_\Omega \nabla p \mathrm{d}\Omega + \int_\Omega \vec{f} \mathrm{d}\Omega \tag{A.4a}$$

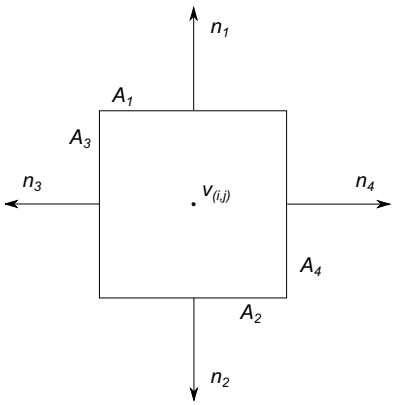

Figure A.1: definition of the areas A_i and unit vectors n_i

Or, rewriting to boundary terms where possible

$$\rho \int_\Omega \frac{\partial \vec{v}}{\partial t} \mathrm{d}\Omega + \rho \int_{\partial\Omega} \vec{v}\,(\vec{v}\cdot\hat{n})\,\mathrm{d}A = \int_{\partial\Omega} \left(\vec{T}\cdot\hat{n}\right)\mathrm{d}A - \int_{\partial\Omega} \left(p\cdot\hat{n}\right)\mathrm{d}A + \int_\Omega \vec{f}\,\mathrm{d}\Omega \tag{A.4b}$$

Due to the indepence of the angle provided, by the radial symmetry, only four boundaries have to be taken into account when calculating the surface integrals. For a v-momentum cell (note that this is not the vector $\vec{v}$ but the component of $\vec{v}$ denoting the vertical speed), the boundaries are shown in figure A.1. For a u-momentum cell, a similar cell is used. The relative location of u and v momentum cells is shown in figure A.2. In the remainder of this section, every term in equation (A.4b) will be considered separately, to reassemble the equation for a single cell afterwards.

The first term of the equation describes the time-dependent behavior of the flow.

$$\rho \int_\Omega \frac{\partial}{\partial t} \begin{pmatrix} u \\ 0 \\ v \end{pmatrix} \mathrm{d}\Omega = \rho\Omega \frac{1}{dt} \begin{pmatrix} u^{(t)} - u^{(t-1)} \\ 0 \\ v^{(t)} - v^{(t-1)} \end{pmatrix} \tag{A.5}$$

Here, u and v represent the horizontal and vertical speed of the flow in the cell, with superscripts to denote the time (current time (t), or one timestep back (t-1)), at which they are taken.

The second term on the left side is the convection term

$$\rho \int_{\partial\Omega} \vec{v}\,(\vec{v}\cdot\hat{n})\,\mathrm{d}A = \rho\cdot(A_1 v_1 - A_2 v_2 - A_3 u_3 + A_4 u_4) \begin{pmatrix} u \\ 0 \\ v \end{pmatrix} \tag{A.6}$$

where the u_i and v_i define the values of the horizontal and vertical speeds at the boundary planes. For building the matrix, the direction of the flows have to be investigated, to see to which component of the matrix (the component related to cell *(i,j)* or one of the neighbour cells) this flow contributes.

Now let us deal with the term $\int_{\partial\Omega} \left(\vec{T}\cdot\hat{n}\right)\mathrm{d}A$, which is the diffusive term. First the full second-order tensor $\vec{T}$ is included (from the book '*Transport Phenomena*' [56]):

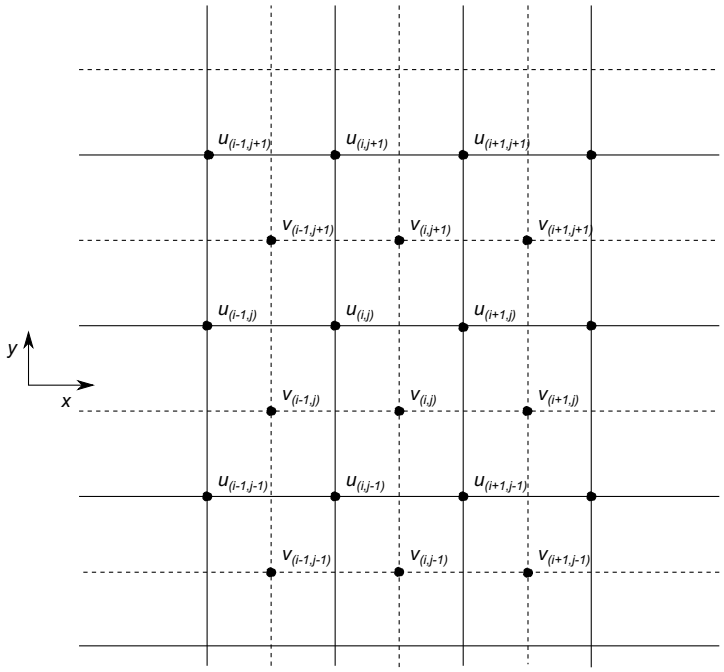

Figure A.2: u-cells are depicted by the dashed lines, v-cells by the solid lines

$$\vec{T} = \mu \begin{pmatrix} 2\frac{\partial v_r}{\partial r} & r\frac{\partial}{\partial r}\frac{v_\theta}{r} & \frac{\partial v_r}{\partial z} + \frac{\partial v_z}{\partial r} \\ r\frac{\partial}{\partial r}\frac{v_\theta}{r} & 2\frac{1}{r}\frac{\partial v\theta}{\partial \theta} + 2\frac{v_r}{r} & \frac{1}{r}\frac{\partial v_z}{\partial \theta} + \frac{\partial v_\theta}{\partial v_z} \\ \frac{\partial v_r}{\partial r} + \frac{\partial v_z}{\partial r} & \frac{1}{r}\frac{\partial v_z}{\partial \theta} + \frac{\partial v_\theta}{\partial v_z} & 2\frac{\partial v_z}{\partial z} \end{pmatrix} \tag{A.7a}$$

$$= \mu \begin{pmatrix} 2\frac{\partial v_r}{\partial r} & 0 & \frac{\partial v_r}{\partial z} + \frac{\partial v_z}{\partial r} \\ 0 & 2\frac{v_r}{r} & 0 \\ \frac{\partial v_r}{\partial r} + \frac{\partial v_z}{\partial r} & 0 & 2\frac{\partial v_z}{\partial z} \end{pmatrix} \tag{A.7b}$$

All θ-dependent terms are taken out of the equation in the conversion from (A.7a) to (A.7b) because of the spherical geometry. For the four different cell boundaries as depicted in figure A.1, the unit normal vectors are given by $\hat{n}_1 = \begin{pmatrix} 0 \\ 0 \\ 1 \end{pmatrix}$, $\hat{n}_2 = \begin{pmatrix} 0 \\ 0 \\ -1 \end{pmatrix}$, $\hat{n}_3 = \begin{pmatrix} -1 \\ 0 \\ 0 \end{pmatrix}$ and $\hat{n}_4 = \begin{pmatrix} 1 \\ 0 \\ 0 \end{pmatrix}$, so we have arrived at

$$\int_{\partial\Omega} \left(\vec{T} \cdot \hat{n}\right) \mathrm{d}A = A_1 \begin{pmatrix} \frac{\partial u}{\partial y} + \frac{\partial v}{\partial x} \\ 0 \\ 2\frac{\partial v}{\partial y} \end{pmatrix} - A_2 \begin{pmatrix} \frac{\partial u}{\partial y} + \frac{\partial v}{\partial x} \\ 0 \\ 2\frac{\partial v}{\partial y} \end{pmatrix} - A_3 \begin{pmatrix} 2\frac{\partial u}{\partial x} \\ 0 \\ \frac{\partial u}{\partial y} + \frac{\partial v}{\partial x} \end{pmatrix} + A_4 \begin{pmatrix} 2\frac{\partial u}{\partial x} \\ 0 \\ \frac{\partial u}{\partial y} + \frac{\partial v}{\partial x} \end{pmatrix} \tag{A.8}$$

The derivatives in the equation are the derivatives at the specific boundary, so that $\frac{\partial v}{\partial y}$ at boundary one boils down to $\frac{v_{(i,j+1)} - v_{(i,j)}}{\mathrm{d}y}$ with $\mathrm{d}y$ the difference in location between the center of the cells.

The only remaining terms are the pressure and force terms:

$$\int_{\partial\Omega} \left(p \cdot \hat{n}\right) \mathrm{d}A = \begin{pmatrix} 0 \\ 0 \\ A_1 p_1 \end{pmatrix} + \begin{pmatrix} 0 \\ 0 \\ -A_2 p_2 \end{pmatrix} + \begin{pmatrix} -A_3 p_3 \\ 0 \\ 0 \end{pmatrix} + \begin{pmatrix} A_4 p_4 \\ 0 \\ 0 \end{pmatrix} \tag{A.9}$$

For the term $\int_\Omega \vec{f}\,\mathrm{d}\Omega$, the main interest is in the *difference* between the densities (and therefore between the forces $\vec{f}$, expressed in Nm^{-3}), emerging from the Boussinesq approximation 2.3:

$$\int_\Omega \vec{f}\,\mathrm{d}\Omega = \begin{pmatrix} 0 \\ 0 \\ f_z \end{pmatrix} = \Omega\left(\Delta\rho\right) g \begin{pmatrix} 0 \\ 0 \\ 1 \end{pmatrix} = -\Omega(\beta\Delta T + \alpha) g \begin{pmatrix} 0 \\ 0 \\ 1 \end{pmatrix} \tag{A.10}$$

So, putting it all together, the discretized Navier-Stokes equation is written as

$$\begin{aligned} &\rho\Omega\frac{1}{dt}\begin{pmatrix} u^{(t)} - u^{(t-1)} \\ 0 \\ v^{(t)} - v^{(t-1)} \end{pmatrix} + \rho\cdot(A_1 v_1 - A_2 v_2 - A_3 u_3 + A_4 u_4)\begin{pmatrix} u \\ 0 \\ v \end{pmatrix} \\ =&A_1\begin{pmatrix} \frac{\partial u}{\partial y} + \frac{\partial v}{\partial x} \\ 0 \\ 2\frac{\partial v}{\partial y} \end{pmatrix} - A_2\begin{pmatrix} \frac{\partial u}{\partial y} + \frac{\partial v}{\partial x} \\ 0 \\ 2\frac{\partial v}{\partial y} \end{pmatrix} - A_3\begin{pmatrix} 2\frac{\partial u}{\partial x} \\ 0 \\ \frac{\partial u}{\partial y} + \frac{\partial v}{\partial x} \end{pmatrix} + A_4\begin{pmatrix} 2\frac{\partial u}{\partial x} \\ 0 \\ \frac{\partial u}{\partial y} + \frac{\partial v}{\partial x} \end{pmatrix} \\ -&\begin{pmatrix} A_4 p_4 - A_3 p_3 \\ 0 \\ A_1 p_1 - A_2 p_2 \end{pmatrix} - \begin{pmatrix} 0 \\ 0 \\ \Omega(\beta\Delta T + \alpha) g \end{pmatrix} \end{aligned} \tag{A.11}$$

or, written down in a more straightforward fashion:

For the u matrix and source vector

$$\begin{aligned} &\rho\left(\Omega\frac{u^{(t)} - u^{(t-1)}}{dt} + (A_1 v_1 - A_2 v_2 - A_3 v_3 + A_4 v_4)\right) u \\ =&(A_1 - A_2)\left(\frac{\partial u}{\partial y} + \frac{\partial v}{\partial x}\right) + 2\,(A_4 - A_3)\frac{\partial u}{\partial x} + A_3 p_3 - A_4 p_4 \end{aligned} \tag{A.12a}$$

For the v matrix and source vector

$$\begin{aligned} &\rho\left(\Omega\frac{v^{(t)} - v^{(t-1)}}{dt} + (A_1 v_1 - A_2 v_2 - A_3 v_3 + A_4 v_4)\right) v \\ =&2\,(A_1 - A_2)\frac{\partial v}{\partial y} + (A_4 - A_3)\left(\frac{\partial u}{\partial y} + \frac{\partial v}{\partial x}\right) + A_2 p_2 - A_1 p_1 - \Omega\left(\beta\Delta T + \alpha\right) g \end{aligned} \tag{A.12b}$$

A.2. Discretization of the concentration equation

The concentration c (in particles L^{-1}) of various isotopes, such as ^{99}Mo and ^{135}Xe, in the fluid is given by

$$\frac{\partial c_i}{\partial t} + \vec{v}\cdot\nabla c_i = \nabla\cdot(\mathscr{D}\nabla c_i) + \gamma_i S - \frac{c_i}{\tau_i} \tag{A.13}$$

where τ is the decay constant, γ the fission yield, $\mathscr{D}$ the diffusion coefficient, S the density of production and the subscripts i denote the component of interest. Once again, the equation can be rewritten to integral form, substituting the volume integrals to surface integrals where possible (equations (A.22a) and (A.22b)). The values for the concentration are determined for the scalar cells, which are situated with respect to both u- and v-momentum cells in such a way that the horizontal and vertical speeds are known at the boundaries of the scalar cell, see figure A.3.

$$\int_\Omega \frac{\partial c_i}{\partial t}\mathrm{d}\Omega + \int_\Omega \vec{v}\cdot\nabla c_i \mathrm{d}\Omega = \int_\Omega \nabla\cdot(\mathscr{D}\nabla c_i)\,\mathrm{d}\Omega + \int_\Omega \gamma_i S \mathrm{d}\Omega - \int_\Omega \frac{1}{\tau_i} c_i \mathrm{d}\Omega \tag{A.14a}$$

$$\int_\Omega \frac{\partial c_i}{\partial t}\mathrm{d}\Omega + \int_{\partial\Omega} c_i\,(\vec{v}\cdot\hat{n})\,\mathrm{d}A = \int_{\partial\Omega} \mathscr{D}\,(\nabla c_i)\cdot\hat{n}\,\mathrm{d}A + \int_\Omega \gamma_i S \mathrm{d}\Omega - \int_\Omega \frac{1}{\tau_i} c_i \mathrm{d}\Omega \tag{A.14b}$$

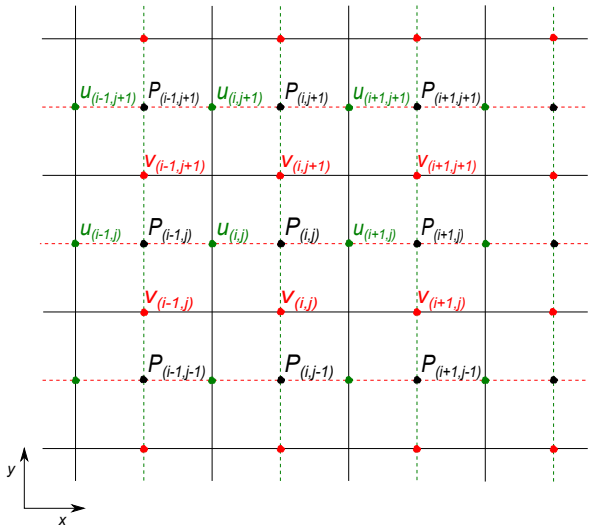

Figure A.3: A part of the grid surrounding the scalar cell *(i,j)*. The cells bounded by the green dashed lines and horizontal solid black lines are the horizontal (u) momentum cells, the cells confined by the vertical solid borders and the red lines are the vertical momentum cells, the cells denoted bij $P_{(i,j)}$ are the scalar cells.

Considering each term separately and combining them all in (A.20):

$$\int_{\Omega} \frac{\partial c_i}{\partial t} \mathrm{d}\Omega = \Omega \frac{c_i^{(t)} - c_i^{(t-1)}}{dt} \tag{A.15}$$

$$\begin{aligned} \int_{\partial\Omega} c_i \left(\vec{v} \cdot \hat{n}\right) \mathrm{d}A &= \begin{pmatrix} 0 \\ 0 \\ c_i A_1 v_1 \end{pmatrix} + \begin{pmatrix} 0 \\ 0 \\ -c_i A_2 v_2 \end{pmatrix} + \begin{pmatrix} -c_i A_3 u_3 \\ 0 \\ 0 \end{pmatrix} + \begin{pmatrix} c_i A_4 u_4 \\ 0 \\ 0 \end{pmatrix} \\ &= \begin{pmatrix} -c_i A_3 u_3 + c_i A_4 u_4 \\ 0 \\ c_i A_1 v_1 - c_i A_2 v_2 \end{pmatrix} \end{aligned} \tag{A.16}$$

$$\int_{\partial\Omega} \mathscr{D} \left(\nabla c_i\right) \cdot \hat{n} \mathrm{d}A = \mathscr{D} \left[A_1 \begin{pmatrix} 0 \\ 0 \\ \frac{\partial c_i}{\partial y} \end{pmatrix} - A_2 \begin{pmatrix} 0 \\ 0 \\ \frac{\partial c_i}{\partial y} \end{pmatrix} - A_3 \begin{pmatrix} \frac{\partial c_i}{\partial x} \\ 0 \\ 0 \end{pmatrix} + A_4 \begin{pmatrix} \frac{\partial c_i}{\partial x} \\ 0 \\ 0 \end{pmatrix} \right] \tag{A.17}$$

$$\int_{\Omega} \gamma_i S \mathrm{d}\Omega = \Omega \gamma_i S \tag{A.18}$$

$$\int_{\Omega} \frac{1}{\tau_i} c_i \mathrm{d}\Omega = \frac{\Omega}{\tau_i} c_i^{(t-1)} \tag{A.19}$$

$$\begin{aligned} \Omega \frac{c_i^{(t)} - c_i^{(t-1)}}{dt} + \begin{pmatrix} -c_i A_3 u_3 + c_i A_4 u_4 \\ 0 \\ c_i A_1 v_1 - c_i A_2 v_2 \end{pmatrix} &= \mathscr{D} \begin{pmatrix} -A_3 \frac{\partial c_i}{\partial x} + A_4 \frac{\partial c_i}{\partial x} \\ 0 \\ A_1 \frac{\partial c_i}{\partial y} - A_2 \frac{\partial c_i}{\partial y} \end{pmatrix} \\ &+ \Omega \gamma_i S + \frac{\Omega}{\tau_i} c_i^{(t-1)} \end{aligned} \tag{A.20}$$

A.3. DISCRETIZATION OF THE ENERGY BALANCE

The energy distribution in the fluid is given by equation (A.21), and is expressed in Js^{-1}.

$$\rho C_p \left(\frac{\partial T}{\partial t} + \vec{v} \cdot \nabla T \right) = \nabla \cdot (\lambda \nabla T) + p \tag{A.21}$$

where C_p is the specific heat, λ the thermal conductivity, ρ the density, p the power per unit volume and T the temperature. The left and right side can both be integrated over the volume Ω. Using mathematical theorems, some terms can be rewritten and expressed as boundary integrals. The exact derivation of the discretized form will be skipped, as it is in parallel with A.2

$$\int_\Omega \rho C_p \frac{\partial T}{\partial t} \mathrm{d}\Omega \quad + \quad \int_\Omega \rho C_p \vec{v} \cdot \nabla T \mathrm{d}\Omega = \int_\Omega \nabla \cdot (\lambda \nabla T) \, \mathrm{d}\Omega \quad + \int_\Omega p \mathrm{d}\Omega \tag{A.22a}$$

$$\rho C_p \int_\Omega \frac{\partial T}{\partial t} \mathrm{d}\Omega \quad + \quad \rho C_p \int_{\partial\Omega} T \, (\vec{v} \cdot \hat{n}) \, \mathrm{d}A = \int_{\partial\Omega} \lambda \, (\nabla T) \cdot \hat{n} \mathrm{d}A \quad + \int_\Omega p \mathrm{d}\Omega \tag{A.22b}$$

$$\rho C_p \Omega \frac{T^{(t)} - T^{(t-1)}}{dt} \quad + \quad \rho C_p \begin{pmatrix} -TA_3 u_3 + TA_4 u_4 \\ 0 \\ TA_1 v_1 - TA_2 v_2 \end{pmatrix} = \lambda \begin{pmatrix} -A_3 \frac{\partial T}{\partial x} + A_4 \frac{\partial T}{\partial x} \\ 0 \\ A_1 \frac{\partial T}{\partial y} - A_2 \frac{\partial T}{\partial y} \end{pmatrix} \quad + p\Omega \tag{A.22c}$$

B

TABLES

Table B.1: Investigation of the correlation between different events. In each row, a different combination of events is shown; each parameter is changed (√) with respect to the reference value, or unchanged (×). Between brackets, the change of the parameter is indicated. For every combination of events shown, the reactivity and uncertainty as calculated by Serpent are shown, as well as the value that is expected if the reactivity effects of the seperate events are added. For events that are uncorrelated, the calculated reactivity will be equal to the expectation. Table continues on the next page.

Xe (×100)	Void (×1.1)	U (×1.02)	T (+10 K)	Water Height (to 30 cm)	Leak (+10%)	Fuel Height (×1.05)	Reactivity	Uncertainty	Expectation (Linear)
√	√	√	√	√	×	×	-0.00352	0.00009	-0.00327
√	√	√	√	×	√	×	0.00239	0.00008	0.00263
√	√	√	√	×	×	×	0.00247	0.00009	0.00256
√	×	√	√	√	×	×	-0.00290	0.00008	-0.00271
√	×	√	√	×	√	×	0.00306	0.00009	0.00312
√	×	√	√	×	×	√	0.01619	0.00009	0.01633
√	×	√	√	×	×	×	0.00296	0.00008	0.00313
√	×	√	×	√	√	×	-0.00169	0.00008	-0.00157
√	×	√	×	√	×	√	0.02611	0.00006	0.01156
√	×	√	×	×	√	√	0.01717	0.00006	0.01747
√	×	√	×	×	×	√	0.01728	0.00008	0.01739
√	×	√	×	×	×	×	0.00422	0.00007	0.00419
√	×	×	√	√	√	×	-0.00709	0.00009	-0.00691
√	×	×	√	√	×	√	0.02077	0.00006	0.00622
√	×	×	√	√	×	×	-0.00706	0.00009	-0.00698
√	×	×	√	×	√	√	0.01196	0.00008	0.01212
√	×	×	√	×	×	√	0.01201	0.00007	0.01205
√	×	×	√	×	×	×	-0.00117	0.00008	-0.00115
√	×	×	×	√	√	√	0.02195	0.00007	0.00735
√	×	×	×	√	√	×	-0.00583	0.00009	-0.00585
√	×	×	×	√	×	√	0.02197	0.00008	0.00728
√	×	×	×	√	×	×	-0.00587	0.00011	-0.00592
√	×	×	×	×	√	√	0.01314	0.00007	0.01319

Xe (×100)	Void (×1.1)	U (×1.02)	T (+10 K)	Water Height (to 30 cm)	Leak (+10%)	Fuel Height (×1.05)	Reactivity	Uncertainty	Expectation (Linear)
√	×	×	×	×	√	×	0.00002	0.00007	-0.00002
√	×	×	×	×	×	√	0.01312	0.00007	0.01312
×	√	√	√	√	×	√	0.02455	0.00009	0.01001
×	×	√	√	√	√	×	0.00269	0.00008	-0.00255
×	×	√	√	√	×	√	0.02515	0.00008	0.01058
×	×	√	√	√	×	×	-0.00272	0.00008	-0.00262
×	×	√	√	×	√	√	0.01647	0.00008	0.01649
×	×	√	√	×	×	√	0.01627	0.00009	0.01642
×	×	√	√	×	×	×	0.00316	0.00007	0.00321
×	×	√	×	√	√	√	0.02623	0.00006	0.01172
×	×	√	×	√	√	×	-0.00166	0.00008	-0.00148
×	×	√	×	√	×	√	0.02628	0.00005	0.01164
×	×	√	×	√	×	×	-0.00166	0.00008	-0.00156
×	×	√	×	×	√	√	0.01731	0.00008	0.01755
×	×	√	×	×	√	×	0.00426	0.00009	0.00435
×	×	√	×	×	×	√	0.01736	0.00009	0.01748
×	×	×	√	√	√	√	0.02091	0.00006	0.00638
×	×	×	√	√	√	×	-0.00690	0.00007	-0.00683
×	×	×	√	√	×	√	0.02095	0.00007	0.00630
×	×	×	√	√	×	×	-0.00705	0.00010	-0.00690
×	×	×	√	×	√	√	0.01217	0.00008	0.01221
×	×	×	√	×	√	×	-0.00085	0.00009	0.00099
×	×	×	√	×	×	√	0.01237	0.00006	0.01214
×	×	×	×	√	√	√	0.0222	0.00008	0.00744
×	×	×	×	√	√	×	-0.00592	0.00009	-0.00576
×	×	×	×	√	×	√	0.02205	0.00008	0.00737
×	×	×	×	×	√	√	0.01321	0.00007	0.01327

ACKNOWLEDGEMENTS

Conducting this research, in a research group that I enjoyed being a part of, I've gone through various states of mind; failing to fix some bugs almost caused premature baldness, solving the problems and getting results, however, outweighed these more stressful times. Now, while dotting the i's and crossing the t's, I can say I'm content with the final product of this project, this thesis.

For that, I have to credit my supervisors, Jan Leen Kloosterman and Martin Rohde, who guided me by posing the right questions, helped me out using their expertise and gave detailed feedback on my writing and reporting.

Furthermore, I want to thank both Danny Lathouwers and Zoltan Perko for their explanation of neutron transport codes and advice on a practical level. Moreover, I want to acknowledge Mark Huisman for the codes he has written for his project, which helped me a lot during my research. I am also grateful to those members of the research group I haven't mentioned explicitly, for providing a great working atmosphere.

Finally, I would like to thank Timothy Kol for the time and effort he has put into proofreading my thesis.